UNIVERSITY OF COPENHAGEN
FACULTY OF SCIENCE

PhD thesis

Per Andersen

Candles that light up the Dark

This thesis has been submitted to the PhD School of The Faculty of Science, University of Copenhagen

Advisor: Jens Hjorth

Submitted: February 28, 2018

Denne afhandling er dedikeret til min mormor

Acknowledgements

This thesis and the research that lay as the foundation would not have been possible without the help and support of a great number of people. I would like to thank the people of the Dark Cosmology Centre at the University of Copenhagen for helping to create a friendly working environment, this goes especially for my fellow Ph.D. students and the postdocs. I would also like to thank the people of the astronomy group at the University of Queensland for welcoming and incorporating me into their group during my stay there. In particular I would like to thank Tamara Davis who has supported me throughout my scientific career and taught me so much. I also would like to thank my supervisor Jens Hjorth for guiding me and for being patient and honest throughout my Ph.D. studies. Finally I would like to give a special thanks to Anne Siegfried for encouraging me and for being loving and supportive.

Abstract

In this thesis I explore four major topics of supernova cosmology. The underlying theme throughout is to improve supernovae as standard candles and thereby improve our understanding of dark energy, dark matter, and cosmology.

For the last few decades the property that type Ia supernovae can be used as standard candles has played a crucial part in constraining the cosmological parameters of the standard cosmological model. Despite having played this crucial role in modern cosmology the progenitor system for type Ia supernovae has so far not been fully understood. In order to understand all systematic effects related to observing type Ia supernovae we need the ability to reliably identify which progenitor system resulted in the type Ia supernovae that we are observing. One way to constrain these progenitor models is through the predicted delay times, the time between star formation and explosion of the type Ia supernovae. On that background we investigate two different ways of measuring the type Ia supernova rates and delay times and how these two methods can be reconciled in a new model. The findings are that the new model is in good agreement with current observations and preferred over the current consensus model. However to constrain type Ia supernova rates in highly star forming regions additional observations are needed in this regime.

Type Ia supernovae can be used to probe the local cosmological bulk flow. Some studies find that this bulk flow is in excess of what is predicted by the standard cosmological model. We show that by taking into account survey geometry and sampling effects when computing the linear theory prediction of this bulk flow these large observed flows can be explained. The finding is that survey geometry and in particular sampling effects can shift the linear theory prediction towards larger bulk flows. This defuses the apparent tension between the measured bulk flow and theory.

Peculiar velocities of type Ia supernova can systematically effect the observed redshifts of Ia supernovae which in turn can cause derived cosmological parameters to also shift systematically. With focus on the Dark Energy Survey type Ia supernova sample it is determined that the method applied to correct for the effects of peculiar velocities in other current studies is sufficient for the Dark Energy Survey sample. This correction must be associated with an uncertainty that is then propagated with other sources of systematic uncertainties in the total uncertainty budget.

After the success of the type Ia supernova as a standard candle at lower redshifts, many candidates for a similarly useful standard candle at higher redshifts have been proposed. The potential utility of these proposed high redshift standard candles is investigated, in particular if they aid in discerning between standard cosmology and a defined subset of modified dark energy models. The finding is that higher redshift standard candles will not contribute to this effort more than lower redshift counterparts as the modified dark energy models under current observational constraints can not deviate significantly from standard cosmology at these higher redshifts. This conversely implies that any deviation from standard cosmology at higher redshifts will pose a problem not just to standard cosmology, but also to the tested subset of modified dark energy models.

Table of Contents

Motivation and Thesis Structure

This thesis has a focus on type Ia supernovae and their use in modern cosmology. The underlying motivation is to constrain cosmological models and ultimately learn more about the nature of dark energy and dark matter.

Although type Ia supernovae play a crucial part in modern cosmology the exact progenitor system, or systems, have so far not been identified. If we are to accurately determine all systematic effects involved in type Ia supernova observations we need to be able to reliably identify the progenitor system of each Ia supernova. For current type Ia supernova surveys systematic uncertainties are the same size as statistical uncertainties, and in the future this balance will only become more dominated by systematics. To this end in chapter 2 is a discussion of two different methods that type Ia supernova rates and delay times are measured followed by a discussion of how these two methods can be reconciled.

It is crucial that whenever observations are in apparent disagreement with standard cosmology that we put these claims to the test. A number of studies have suggested that the local cosmological bulk flow is in excess of what is predicted by standard cosmology. In chapter 3 we therefore test whether the large observed bulk flows could be caused by sparse sampling and survey geometry effects or whether there truly is disagreement with standard cosmology.

A problem for the current standard cosmology is the apparent discrepancy between the Hubble constant measured by local probes such as type Ia supernovae and that measured from observations of the cosmic microwave background. The current disagreement is roughly $\sim 3\sigma$, which is interesting but by no means strong enough evidence to reject the current standard cosmology. Future type Ia surveys will however tighten the constraints on the cosmological parameters and help shed light on whether there truly is disagreement between nearby and distant probes within the standard cosmology paradigm. The larger number of type Ia supernovae that these surveys will observe translates to the uncertainty budget being dominated more by systematic uncertainties as the statistical uncertainties will become smaller. Among these systematics are the effects of peculiar velocities, which introduce a non-trivial systematic redshift contribution to the observed redshifts of type Ia supernovae and is significant at redshifts of 0.1 or less. On that background chapter 4 discusses the current methods applied when correcting for the systematic redshift effects of peculiar velocities, and how future surveys can improve upon this approach to continue to provide reliable and competitive cosmological constraints.

It has been argued that standard candles at high redshift ($z \gtrsim 2$) will aid in constraining cosmological models and that future telescopes such as the James Webb Space Telescope promises

to enable observations of these proposed high redshift standard candles. Before investing considerable observational resources in observing these high redshift standard candles it is important to determine what questions high redshift standard candles will aid in answering. This has been an open question and on that background chapter 5 discusses the utility of high redshift standard candles in discerning between different models for dark energy.

This thesis is structured with first an introduction to the topics I have worked within during my Ph.D. degree. This introduction is meant to be available to anyone with a general astrophysics background and therefore includes both some historical context but also the current status of each topic. Following this general introduction are the four main scientific products of this thesis, which make up chapter two through five. Finally in chapter six is a summary of this thesis as well as a proposed outline for how further progress can be made within the thesis topics.

Chapter 1

Overview of Type Ia Supernovae and Cosmological Applications

In astronomy transient phenomena, such as supernovae, gamma ray bursts, or the merging of black holes or neutron stars present an opportunity to investigate physics at energy scales that are simply not possible to investigate here on Earth. Supernovae in particular have been observed by astronomers at least as far back as July 4th 1054 where Chinese astronomers observed a supernova where we today can observe the remnant in the Crab Nebula. Danish astronomer Tycho Brahe observed a supernova in 1572 that we now know was a type Ia supernova. The large bolometric luminosities of type Ia supernovae of $\sim 10^{43} \mathrm{erg\,s^{-1}}$ at their maximum means that they constitute a large portion of the supernovae observed since their extreme luminosities allow them to be observed from large distances. At their peak type Ia supernovae shine as bright as roughly 10 billion suns, enabling them to shine as bright as the total sum of stars that make up their host galaxy. Their apparent homogeneity which allows them to be used as standardisable candles, the details of which will be explained later, additionally make them an object of extreme interest in modern cosmology.

The first long-term set of spectra of a type Ia supernova were observed by Minkowski (1939) who used photographic plates to observe SN 1937C. Since then major advancements in both the quality and quantity of type Ia supernova observations have taken place, especially since the advent of the charged-coupled device (CCD). Type Ia supernovae are classified by their lack of hydrogen and helium features in their optical spectra, and are incredibly uniform in their spectra and light curves (Maoz et al., 2014). Averaged type Ia supernova redshifts in various redshift ranges are shown in figure 1.1 and illustrate the uniformity of type Ia spectra. Type Ia supernova reach a maximum in optical within $\sim$15-20 days and then decline by roughly three magnitudes in one month and then steadily one magnitude per month over the following months.

Physical models for type Ia supernova explosions are reviewed in Hillebrandt and Niemeyer (2000), later updated in Hillebrandt et al. (2013). Type Ia supernovae are observed in old stellar populations and show a distinct lack of hydrogen and helium in in the spectra. There is broad consensus that this is a strong indication that the core is a white dwarf which when it reaches

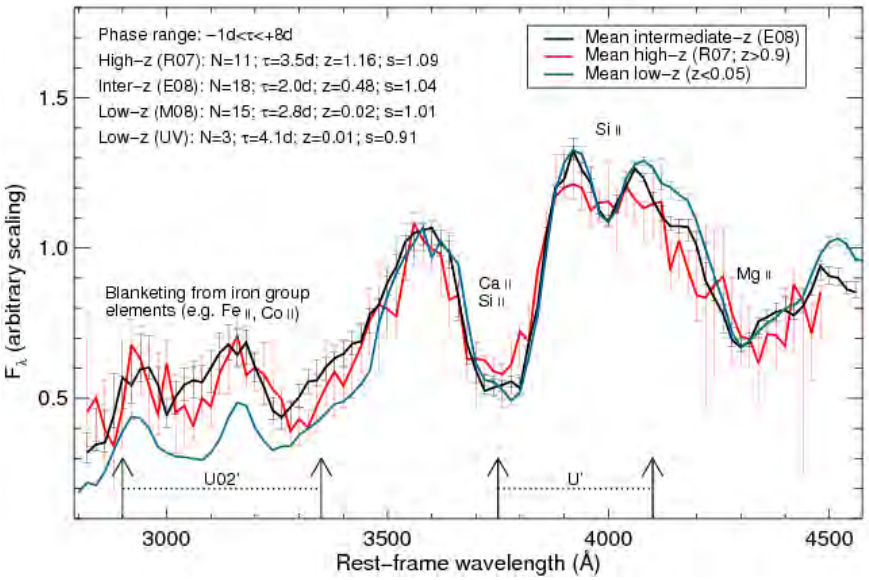

Figure 1.1: Averaged spectra of type Ia supernovae at various redshift ranges. The spectral features of selected elements are highlighted for convenience. Reproduced from Sullivan et al. (2009).

the Chandrasekhar mass of $\sim 1.4 M_{\odot}$ experiences runaway fusion of carbon and oxygen in the core. The physical mechanism that produces the observed luminosity is then nuclear decay of first ^{56}Ni to ^{56}Co and thereafter ^{56}Co to the stable isotope ^{56}Fe, with the exponential timescales of these decays being nine and 114 days respectively. The majority of this luminosity is in the optical spectrum, as an optically thick ejecta reprocesses short wavelength photons into the optical regime. Some variance is however observed in the features of type Ia supernovae and the exact progenitor, or progenitors, of type Ia supernovae are currently unknown.

1.1 Type Ia Supernova Progenitor Models

While there is strong consensus that type Ia supernovae are white dwarfs undergoing thermonuclear explosion, the same consensus does not exist when it comes to the question of how the white dwarf reaches this state. As white dwarfs are inherently stable some interaction between the white dwarf and another object must take place. Recent evidence suggests that there are likely more than one possible avenue that can lead to white dwarfs undergoing rapid thermonuclear explosion. Evidence suggests that type Ia supernovae that are more luminous than the average are predominantly found in highly star forming galaxies, and vice versa with less luminous type Ia supernovae more often found in galaxies with little or no active star formation. See Branch (1998) for a review and Hicken et al. (2009), Kelly et al. (2010), or Sullivan et al. (2010) for a discussion of type Ia supernovae and host galaxy correlations. When the diversity of observations is taken into account, it seems improbable that a single progenitor channel can account for all observed type Ia supernovae. There is however not concrete evidence yet to say with certainty either way. For a progenitor model to hold up to scrutiny it must have a robust explosion mechanic, match observed peak luminosities, light curves, birth rates, and delay times. This is a tall order, and so far no single

progenitor can fulfil all these requirements. That does not mean that we are completely ignorant on type Ia supernova progenitors, or that progress has not been made in the last few decades. In this section we will investigate some of the proposed progenitor models, and consider how they stack up against observations. When going through these progenitors we will group them according to the same prescription as Hillebrandt et al. (2013), e.g. Chandrasekhar mass, sub-Chandrasekhar mass, double degenerate, and others.

1.1.1 Chandrasekhar Mass - Single Degenerate

The Chandrasekhar mass progenitors are commonly referred to as single degenerate and were in the past the most promising type Ia supernova progenitor. The mechanism is that a companion star, which is either a main sequence star or a red giant, is feeding the white dwarf material through Roche-lobe overflow. In order for the transfer of mass to be stable the transfer rate needs to be at least $\sim 10^{-7}\, M_{\odot}\, \mathrm{yr}^{-1}$ (Nomoto et al., 2007) (see also Shen and Bildsten (2007), Wolf et al. (2013), or Starrfield (2014) for a different view). With a stable mass transfer the white dwarf will burn hydrogen, which slowly increases the density in the core of the white dwarf. Once the white dwarf mass reaches the Chandrasekhar limit of $\sim 1.4\, M_{\odot}$ the white dwarf collapses and explodes as a type Ia supernova. The companion star is initially more massive than the white dwarf. It will then lose its hydrogen rich envelope on the asymptotic giant branch, fill its Roche-lobe and form the common envelope that then feeds material to the white dwarf, possibly through forming an accretion disk around the white dwarf. It is believed that it is also possible for the companion star to be a helium rich star, rather than hydrogen rich (Solheim and Yungelson, 2004). This scenario involves the companion star to be of higher mass than in the previous scenario, which in turn causes the delay time from formation to detonation to be shorter. This, combined with this scenario possibly causing observables such as the spectrum of the type Ia supernovae to differ from the previous scenario, leads to some (see e.g. Ruiter et al. (2011)) classifying this as a distinct progenitor scenario.

Supernovae are physically complex and to model them requires a firm understanding of magnetohydrodynamics. Magnetohydrodynamics is conducted using numerical methods, and the complexity of the models is therefore limited by the available computing power. Traditional models have therefore been one dimensional, which although they suffer from severe limitations have taught us a lot about the inner workings of type Ia supernovae, see e.g. Nomoto et al. (1984) for a seminal paper on the topic. Modern simulations however have much more computing power available and can therefore be run in three dimensions. Going from one to three dimensions in the context of simulating type Ia supernovae is a double-edged sword. The advantages are clear; it enables modelling of effects such as turbulence and asymmetric burning and propagation of the explosion. On the other hand a multitude of assumptions are needed in order to run a full simulation in three dimensions. Many distinct parts come together and interact in a manner that is not always obvious. This requires meticulous study of the effects that each assumption has on the outcome of the simulation. Ultimately we wish to compare the results of these simulations with observables. From studying the evolution of type Ia supernova light curves the consensus is that (Hillebrandt

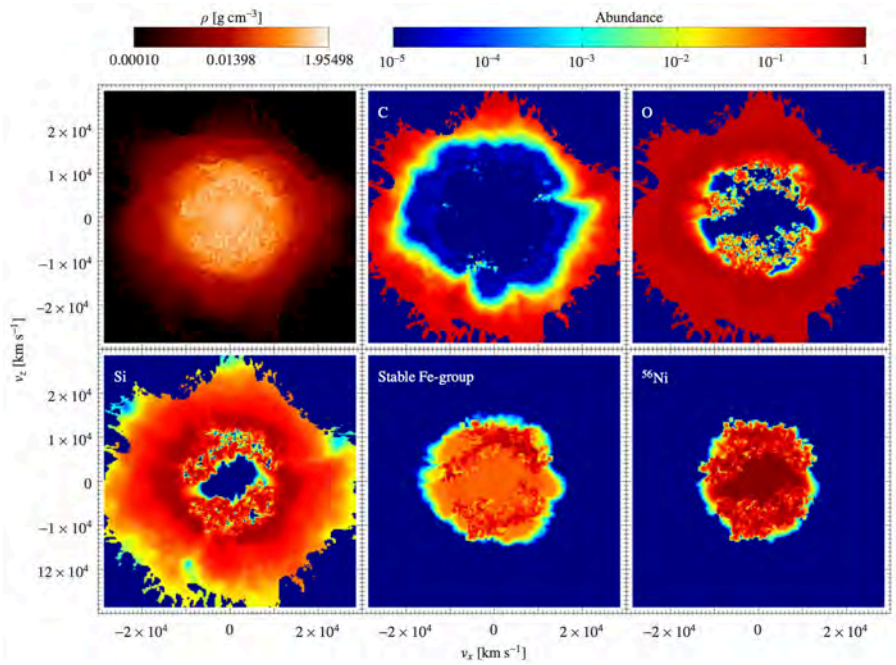

Figure 1.2: Slices through the N100 type Ia supernova simulation of Röpke et al. (2012). Top left figure shows the density and the remaining five figures show the distribution of selected elements 100 seconds after detonation. It is apparent that the inner core consists of stable iron and ^{56}Ni which will subsequently decay and thereby produce the observable optical luminosity. Reproduced from Röpke et al. (2012).

et al., 2013) the observations are in agreement with decay of between 0.3-0.9 $\mathrm{M}_{\odot}$ of ^{56}Ni. This supports models where the detonation happens through deflagration, rather than through prompt detonation. Models based on prompt detonation produces more ^{56}Ni than what is in agreement. Deflagration however preheats and pre-expands the material which in turn results in the burning taking place at lower densities and more material ending up as intermediate mass elements and not ^{56}Ni. See e.g. Seitenzahl et al. (2013) or Röpke et al. (2012) for examples of numerical simulations of a single degenerate progenitor. Figure 1.2 shows slices through the three dimensional simulation of a type Ia supernova from Röpke et al. (2012) 100 seconds after detonation. It is apparent that the produced ^{56}Ni is embedded in an envelope of intermediate mass elements such as carbon and oxygen.

1.1.2 Sub-Chandrasekhar Mass - Double Detonation

A progenitor channel where the explosion happens at sub-Chandrasekhar masses has been suggested (e.g. Shen et al. (2010) or Solheim (2010) for a review). It derives its name from the explosion mechanic in which two subsequent detonations take place. In this scenario the white dwarf accretes helium from a companion star. This layer of helium may then under the right circumstances detonate (Tutukov and Yungelson, 1996), which may then trigger a second detonation that leads to the white dwarf exploding as a type Ia supernova. There are two distinct proposed channels which can lead to a white dwarf stably accreting helium. The first channel is that the primary star unstably fills its Roche-lobe while on the asymptotic giant branch, stripping the common

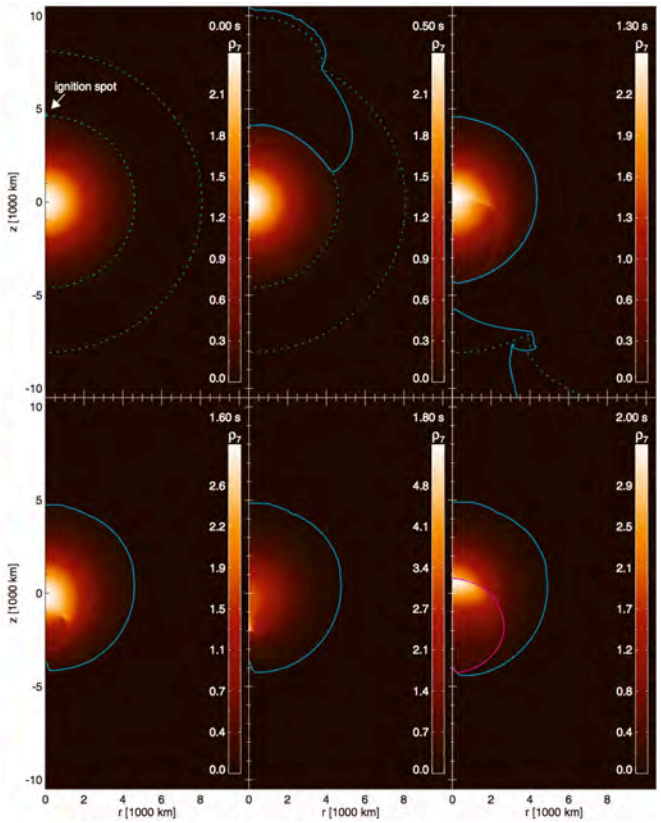

Figure 1.3: A time series evolution of the density of double detonation model two by Fink et al. (2010). The dashed cyan lines mark the border of the helium shell, and the solid cyan/magenta lines are the carbon/oxygen flames. Note that the density scale varies over time. Reproduced from Fink et al. (2010).

envelope and resulting in a white dwarf and main sequence binary. A second common envelope forms when the secondary star unstably fills its Roche-lobe, which results in a binary system consisting of a white dwarf and a stripped core of a giant with an exposed helium burning core that then subsequently feeds helium onto the white dwarf, which eventually causes detonation through the double detonation method described above. The second channel is similar to the first, except that here the initial mass of the secondary star is smaller. After the second common envelope this smaller mass results in a setup similar to the first where a white dwarf is accreting helium from an exposed helium core, however the helium donor star is in this scenario not massive enough to burn helium itself.

The double detonation scenario has been modelled by e.g. Sim et al. (2010) who found that a type Ia supernova with $\sim 0.6\, M_\odot$ of ^{56}Ni can come from a detonation of a white dwarf with a mass of $\sim 1.1\, M_\odot$. They then derived observables from their simulation and found that the B-band light curves produced by their models are in decent agreement with observations. In figure 1.3 a density time series of double detonation model two by Fink et al. (2010) is shown. Fink et al. (2010) finds that the explosion mechanics are robust against effects such as asymmetries in the initial ignition or a low mass of the helium shell.

1.1.3 Double Degenerate

In the double degenerate scenario two white dwarfs with a combined mass in excess of the Chandrasekhar limit merge and explode as a type Ia supernova. A number of scenarios can lead to a binary system with two white dwarfs. One could be that the primary star fills its Roche-lobe and stably transfers mass to the secondary star. This strips the primary star and evolves it into a white dwarf. The secondary star then fills its Roche-lobe and unstably transfers material to the primary star, causing a common envelope to form. After some time and additional mass transfer (this time stable) from the secondary to the primary star, a binary has formed consisting of two white dwarfs in close orbit. The double degenerate progenitor has historically, along with the single degenerate progenitor, been the most prominent progenitor to explain how the bulk of type Ia supernovae form. Some studies have however cast some doubt on this picture. Some (see e.g. Miyaji et al. (1980) or Saio and Nomoto (1985)) find that the accretion between the white dwarf binaries can lead to burning happening in the outer layers of the white dwarf, rather than at the centre, which could turn the white dwarf into an oxygen-neon-magnesium white dwarf rather than a carbon-oxygen white dwarf. More recently Liu et al. (2017) numerically evolved roughly 1800 binary systems varying the initial conditions to produce a grid for producing type Ia supernovae through the double degenerate scenario. By interpolating over their grid they then perform binary population synthesis simulations and find that the double degenerate model may contribute up to 16 percent of all observed type Ia supernovae.

1.1.4 Other Progenitor Models

A multitude of other progenitor channels have been proposed in the literature. One example is the merger of a carbon-oxygen rich white dwarf and an asymptotic giant branch star during a common envelope event (Livio and Riess, 2003). In the reviews of Hillebrandt et al. (2013), Maoz et al. (2014), and Livio and Mazzali (2011) there is a more in depth discussion of the above progenitor models as well as other models. Among them are the collisional variant of the double degenerate progenitor. This is a model intended to explaining the possibility that some type Ia supernovae originate in dense stellar environments such as galactic nuclei or globular clusters. A third low mass star would be in orbit around the inner white dwarf binary. Through the Lidov-Kozai mechanism the orbit of the inner white dwarfs could become highly eccentric. An eccentric orbit would cause the time to merger to shorten as more energy is lost through gravitational waves, which would eventually lead to a merger of the white dwarfs, or in rare conditions a head on collision. Current constraints however suggest that such progenitors will be relatively rare, as only 10-20% of stars are in triple systems, and likely only a small fraction of these will have the necessary ratios of the orbits.

1.1.5 Progenitors and Delay Times

Having looked specifically at the delay times for the single degenerate scenario Bours et al. (2013) find that it is not possible to produce sufficient type Ia supernovae at long delay times, therefore

failing to reproduce the tail end of the observed $\sim\tau^{-1}$ delay time distribution. This is due to this progenitor channel not being able to produce binary systems with orbital periods much above a few hundred days, which in turn causes short in-spiral times. Their conclusion is therefore that while the single degenerate progenitor channel may contribute significantly to the observed type Ia supernovae at short delay times, it is highly unlikely to represent the entirety of observed Ia supernovae. Ruiter et al. (2011) discuses the delay times of the double detonation progenitor channel. The approach applied is to use binary population synthesis code to map out the possible delay times. Ruiter et al. (2011) define two distinct channels of formation, called the prompt channel with delay times $<$500 Myr and the delayed channel with delay times of $\gtrsim$800 Myr and up to the Hubble time. They find that the prompt channel account for 13% of all double detonation type Ia supernovae, while the remaining 87% are produced in the delayed channel. This is in good agreement with the results of Rodney et al. (2014) that likewise define a prompt and delayed channel. When looking at delay times of the double degenerate progenitor channel they largely reproduce the observed $\sim\tau^{-1}$ delay time distribution. For delay times larger than $\sim$1 Gyr Yungelson and Livio (2000) find excellent agreement with observations. For shorter delay times however the delay time is dominated by the production rate of the white dwarfs, which instead scales as $\sim\tau^{-1/2}$ (Pritchet et al., 2008). Some models include a transition away from τ^{-1} at short delay times (see e.g. Rodney et al. (2014)) and the current observations do not have sufficient constraining power to determine whether a τ^{-1}, $\tau^{-1/2}$, or possible a constant τ^{0} is the best fit at short delay times.

With respects to the observed delay times the double degenerate progenitor channel seems to come out slightly ahead. There is however no substantial amount of evidence favouring any one scenario, and each of the progenitor scenarios discussed here have their own unresolved issues. In order for the double degenerate scenario to be the dominant one it needs to include a scenario where triple stellar systems invoke a prompt collision, although it is uncertain that enough double white dwarf systems will exist in triple star systems with an appropriate configuration (Leigh and Geller, 2013) or that the inner binary in the triple configuration will not collide while on the main sequence (Hamers et al., 2013). In the recent review of Livio and Mazzali (2011) the progenitor channels presented here are discussed and the strengths and weaknesses of each reviewed. They find that while the single degenerate scenario is the one that has been investigated the most and also explains many of the current observations it is not without shortcomings. One of these shortcomings is that it does not easily explain the observed delay times, which are of particular interest in this thesis. The fact that the substantial effort over the last decades to determine the progenitor channel has so far not reached a certain conclusion could be interpreted as a suggestion that there may be two or more Ia supernova progenitor channels. Livio and Mazzali (2011) compare the current status to that of gamma ray bursts before it was realised that there are two distinct events, short and long, caused by distinct physical phenomena. They further argue that processes involving thermonuclear explosions are sensitive to initial conditions and small changes can result in a multitude of different outcomes. Additionally the proposed progenitor channels of type Ia supernovae are more similar than the two mechanisms responsible for gamma ray bursts, collapse of the cores of massive stars and neutron star-neutron star collisions. It may therefore yet take some

time before a full understanding of the scenario, or scenarios, that lead to type Ia supernovae are fully understood.

1.2 How to use type Ia supernovae as standard candles

In the early 1990's a large number of extragalatic distance indicators existed. Jacoby et al. (1992) reviewed seven of the most reliable, including globular-cluster luminosity functions, type Ia supernovae, HI line width relations, planetary-nebula luminosity functions, surface brightness fluctuations, and fundamental plane relations for elliptical galaxies. Among these one in particular later rose to prominence in cosmology; the type Ia supernova. In Jacoby et al. (1992) it was however concluded that the uncertainties on distances from type Ia were relatively large, making them a less competitive distance indicator. One supernova in particular was a cause for concern, SN 1991bg, which reached a peak light curve magnitude in the B band that was $\sim$2.5 magnitudes fainter than SN 1957B. Both SN 1991bg and SN 1957B were type Ia supernovae, and importantly they both had the same host galaxy, the elliptical NGC4374. The magnitude difference between the two supernovae was therefore unlikely to be a result of varying host galaxy conditions. The important piece to the puzzle was added in Phillips (1993) where it was noted that while SN 1991bg was much fainter at maximum light than other type Ia supernovae, the light curve also declined unusually fast. In the seminal paper by Phillips (1993) the absolute magnitudes at maximum light for type Ia supernovae is shown to be tightly correlated with the decline rate of the light curve. Specifically Phillips (1993) introduced the parameter Δm_{15}, which is the difference between apparent magnitude at peak brightness and fifteen days after peak, typically in the B-band. The relation found by Phillips (1993) is apparent in figure 1.4 and can be written in the form (Phillips, 1993; Phillips et al., 1999; Kattner et al., 2012)

$$M(B)_{\max} = -21.726 + 2.698\Delta m_{15}(B), \tag{1.1}$$

where $M(B)_{\max}$ is the absolute B-band magnitude and $\Delta m_{15}(B)$ is Δm_{15} as measured in the B-band.

Despite the initial success of the method from Phillips (1993) in standardising the type Ia standard candle it failed in taking into account the variability in the observed light curves caused by variation in the large spectral features of type Ia supernovae. Various approaches attempt to resolve this issue by fitting a stretch parameter (Riess et al., 1995; Perlmutter et al., 1997), using color information (Wang et al., 2003, 2005), or both (Riess et al., 1996; Guy et al., 2005). The current state of the art model to fit type Ia supernova light curves is the SALT2 empirical model by Guy et al. (2007). The model is summarised in the equation

$$m_B = M_B - \alpha X_1 + \beta C + \mu \tag{1.2}$$

where m_B and M_B are the apparent and absolute magnitudes at maximum in the B-band. X_1 is the stretch term and C the colour term, with α and β being globally fit variables that are assumed

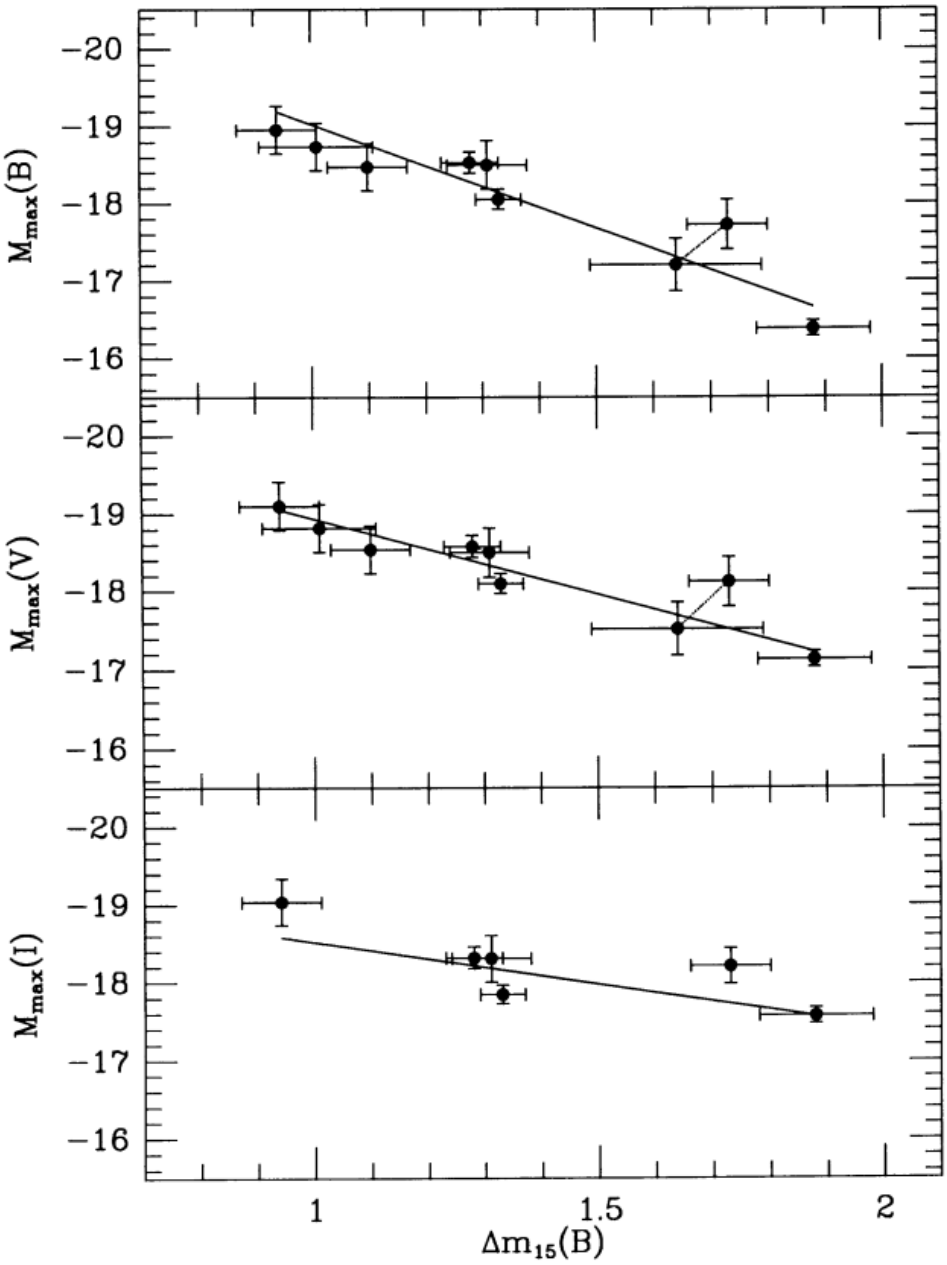

Figure 1.4: The relation between the decline in peak apparent magnitude and 15 days later and absolute magnitude in the B, V, and I bands. This relation facilitates the standardising of type Ia supernovae into a standard candle with only little intrinsic scatter on the derived absolute magnitudes. Reproduced from Phillips (1993).

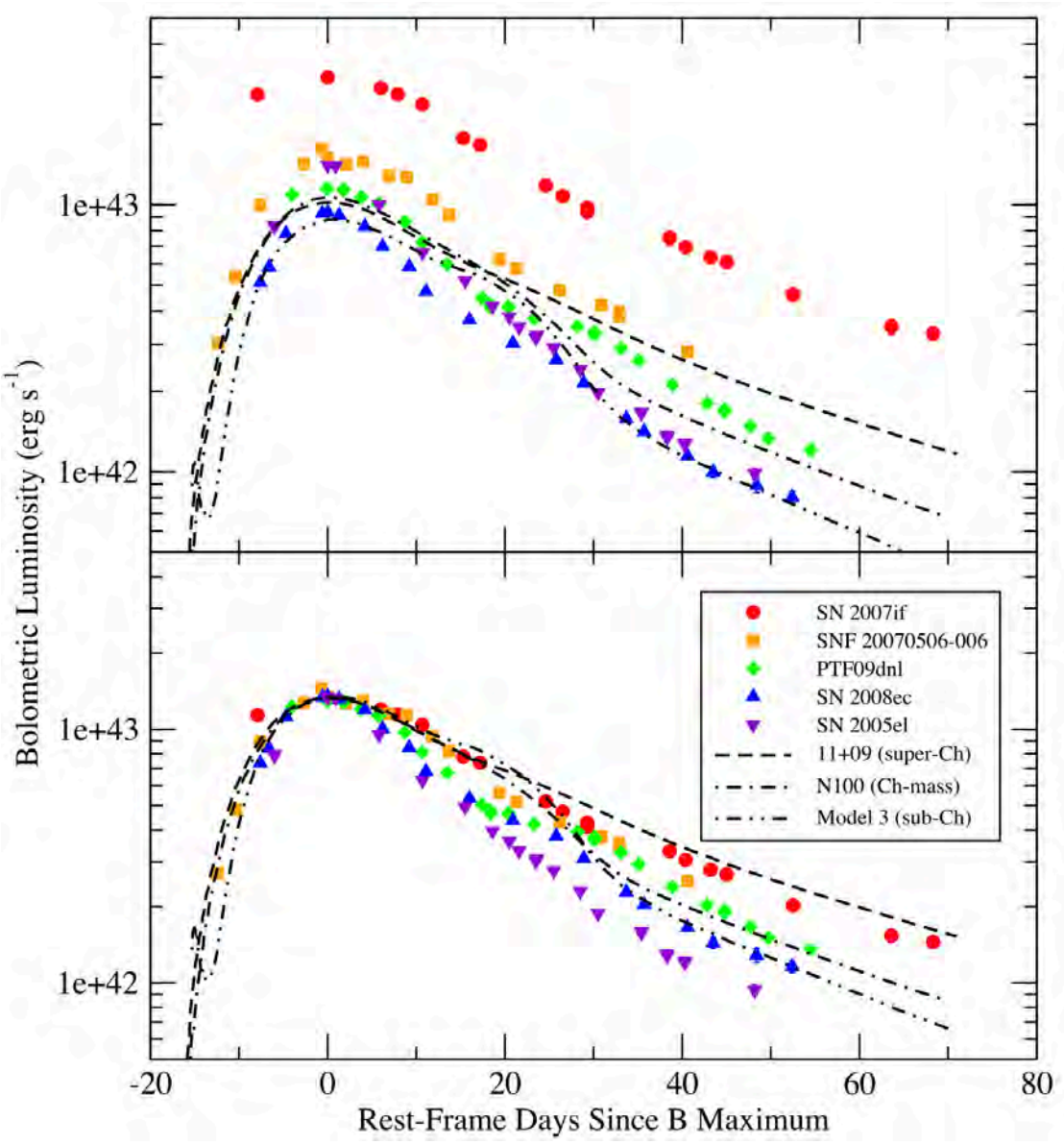

Figure 1.5: Observed bolometric light curves of type Ia supernovae from the SNfactory (coloured symbols) and synthetic light curves for explosion models (black curves). The upper half of the figure shows the original light curves and the bottom light curves normalised to a peak luminosity of $1.2 \cdot 10^{43}$erg s^{-1}. Reproduced from Guy et al. (2007).

to be constant for all type Ia supernovae. Finally μ is the distance modulus of the supernovae, which is dependent on the redshift of the host galaxy and assumed cosmology. In figure 1.5 a representative sample of type Ia supernova light curves are shown alongside synthetic light curves from explosion models.

1.2.1 Calibration of absolute magnitudes

To derive absolute, rather than relative, distances to type Ia supernovae requires calibration of the absolute magnitude, M_B, of the type Ia supernovae in question. This is done through observing type Ia supernovae in galaxies which have absolute distances from some other distance indicator. In theory it does not matter which distance indicator is used, however in practice the standard today is to use the period-luminosity relation of Cepheid variables to derive absolute distances to nearby type Ia supernovae. The period-luminosity relation takes the form

$$m_W = b_W(\log_{10} P - 1) + Z_W \Delta \log_{10}[O/H]_{ij} + M_W + \mu \tag{1.3}$$

where m_W is the 'extinction-free' apparent magnitude, P is the period in days, and $\Delta \log_{10}[O/H]_{ij}$ the metallicity of the Cepheid. The absolute magnitude M_W is the magnitude of a Cepheid at a distance of 10 pc and with a period of 10 days, and μ the distance modulus of the Cepheid host galaxy. b_W and Z_W are fitting parameters that tune the dependency of the magnitude on period and metallicity of the Cepheid. For further details on the definitions see Madore (1982) or Zhang et al. (2017) for a more recent application of Cepheids to calibrate type Ia supernovae absolute magnitudes.

1.3 Modern cosmology

Our understanding of the universe has evolved immensely over the last 100 years. In 1920 a debate at the Smithsonian Museum of Natural History between Harlow Shapley and Heber Curtis centred on the existence of galaxies other than the Milky Way and the size of the observable universe as a whole. The accepted model of the time that Shapley supported was that the Milky Way made up the entire universe and that objects such as the Andromeda galaxy were merely nebulae and part of the Milky Way. Curtis on the other hand argued that Andromeda and other similar objects were galaxies, or "island universes", in their own right. Additional observations eventually proved Curtis's assertion correct. Among these were observations published in Hubble (1929) that showed a linear relation between distance and recession velocity of the form

$$v = H_0 d. \tag{1.4}$$

Equation 1.4 is known as Hubble's law, relating the velocity v and distance d through the Hubble constant H_0 which is typically quoted in units of $\mathrm{km\,s^{-1}\,Mpc^{-1}}$. The observations that lay as the original foundation of Hubble's law are shown in figure 1.6.

While Hubble's law is exceedingly simple it does not accurately describe observed recession

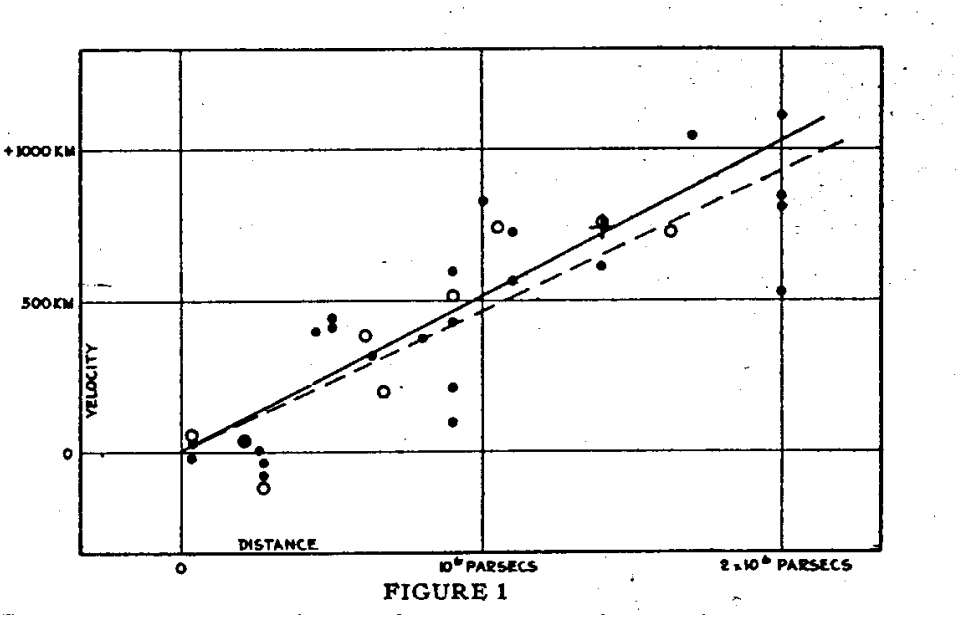

Figure 1.6: Velocities against distances for extra galactic nebulae. The linear relation illustrates that more distant astronomical objects recede from the observer at increasing velocities. Reproduced from Hubble (1929).

velocities at larger distances. The more general Hubble parameter is defined as

$$H(t) = \frac{\dot{a}(t)}{a(t)} \tag{1.5}$$

where $a(t)$ is the scale factor and the dot denotes taking the time derivative. In the following the notation that a subscript of '0' denotes the value at present is adopted. To derive an expression for how the Hubble parameter varies we start with Einstein's field equations. Then assuming an isotropic and homogeneous universe with constant curvature one can derive a metric of the form

$$ds^2 = -c^2dt^2 + a(t)^2\left[dr^2 + R_0^2 S_k(\chi)^2 d\Omega^2\right], \tag{1.6}$$

which is known as the Friedmann-Lemaitre-Robertson-Walker (FLRW) metric. Here c is the speed of light in vacuum, $a(t)$ is the scale factor, $S_k(\chi)$ is

$$S_k(\chi) = \begin{cases} \sin(\chi) & \text{for } \kappa = 1 \\ \chi & \text{for } \kappa = 0 \\ \sinh(\chi) & \text{for } \kappa = -1 \end{cases} \tag{1.7}$$

where R_0 is the curvature radius at present day, χ the dimensionless comoving distance, and κ is either 1, 0, or -1 for a positively curved, flat, or negatively curved universe. The final term $d\Omega$ is given by

$$d\Omega^2 = d\theta^2 + \sin^2\theta d\phi^2, \tag{1.8}$$

containing the spherical coordinates θ and ϕ. For the FLRW metric an equation that governs

the expansion rate of the universe can then be derived. The equation is known as the Friedmann equation and is

$$H(t)^2 = \left(\frac{\dot{a(t)}}{a(t)}\right)^2 = \frac{8\pi G}{3c^2}\varepsilon(t) - \frac{\kappa c^2}{R_0^2 a(t)^2} + \frac{\Lambda}{3}. \tag{1.9}$$

The Friedmann equation in equation 1.9 includes the Λ term which is known as the cosmological constant. The term was introduced by Einstein in Einstein (1917) to keep the universe static, but today plays a very different role that will soon become apparent. $\varepsilon(t)$ is the energy density of the universe, and in equation 1.9 it includes contributions from matter and radiation, but not the cosmological constant which has been separated to show explicitly that it is not a function of time. If we absorb the cosmological constant Λ into the total energy density $\varepsilon(t)$ and assume flatness, e.g. $\kappa = 0$, equation 1.9 becomes

$$H(t)^2 = \frac{8\pi G}{3c^2}\varepsilon(t), \tag{1.10}$$

which in turn implies that there is a critical energy density

$$\varepsilon_c = \frac{3c^2}{8\pi G}H(t)^2, \tag{1.11}$$

where the universe is neither positively or negatively curved, but rather flat.

While equation 1.9 is a very powerful and important equation in cosmology we can not from it alone derive an expression for how the scale factor $a(t)$ evolves as a function of time. Rather, two additional pieces need to be added in order to solve the puzzle. The first is called the fluid equation and is often written as

$$\dot{\varepsilon} + 3\frac{\dot{a}}{a}(\varepsilon + P) = 0, \tag{1.12}$$

where P is the pressure. The second piece is that we need to relate the pressure P to the energy density ε through an equation of state. A simple solution is to assume a relation

$$P = w\varepsilon \tag{1.13}$$

where w is a dimensionless number that is 0 for matter, 1/3 for radiation, and -1 for the cosmological constant. With this the fluid equation can be written as

$$\dot{\varepsilon} + 3\frac{\dot{a}}{a}(1 + w)\varepsilon = 0. \tag{1.14}$$

Solving the separable differential equation and assuming that w is constant for each component reveals the relation

$$\varepsilon(a) = \varepsilon_{w,0}a^{-3(1+w)}, \tag{1.15}$$

where again the notation is that a subscript of 0 indicates value at present day. For matter, radiation, and the cosmological constant the solutions are

$$\varepsilon_m(a) = \varepsilon_{m,0}a^{-3} \tag{1.16}$$

for matter,

$$\varepsilon_r(a) = \varepsilon_{r,0} a^{-4} \tag{1.17}$$

for radiation, and

$$\varepsilon_\Lambda(a) = \varepsilon_{\Lambda,0} \tag{1.18}$$

for the cosmological constant. It is common practice to write the energy densities as a fraction of the critical energy density by defining

$$\Omega(t) = \frac{\varepsilon(t)}{\varepsilon_c(t)} \tag{1.19}$$

where $\Omega(t)$ is then referred to as the dimensionless density parameter.
Dividing equation 1.9 through with H_0 and applying the above definitions allows us to write the Friedmann equation as

$$\frac{H(a)^2}{H_0^2} = \Omega_{r,0} a^{-4} + \Omega_{m,0} a^{-3} + \Omega_{\Lambda,0} + \Omega_{k,0} a^{-2}, \tag{1.20}$$

where for convenience we defined $\Omega_{k,0} = 1 - (\Omega_{r,0} + \Omega_{m,0} + \Omega_{\Lambda,0})$. Equation 1.20 gives us the Hubble parameter, $H(a)$, as a function of scale function given that the cosmological parameters H_0, $\Omega_{r,0}$, $\Omega_{m,0}$, and $\Omega_{\Lambda,0}$ are known. Note here that the Hubble parameter is written as a function of scale factor rather than time. This is standard practise as the scale factor relates to the easily observed redshift (assuming that $a_0 = 1$) through the simple relation

$$a = \frac{1}{1+z}, \tag{1.21}$$

where going from redshift to time is possible, but by no means a trivial operation.

In Ia supernova cosmology the observed quantity is often what is known as the distance modulus, μ. To relate distance modulus to the cosmological parameters from above requires a few steps. First, distance modulus is given as

$$\mu(z) = 5 \log_{10}[D_L(z)] + 25, \tag{1.22}$$

when the luminosity distance, $D_L(z)$, is measured in Mpc. The luminosity distance is in turn given by

$$D_L(z) = (1+z) \frac{c}{H_0 \sqrt{\Omega_{k,0}}} S_k(\chi), \tag{1.23}$$

where $S_k(\chi)$ is defined in equation 1.7 and $\chi(z)$ is

$$\chi(z) = H_0 \sqrt{\Omega_{k,0}} \int_0^z \frac{dz'}{H(z')}, \tag{1.24}$$

when the chosen variable to integrate over is the observed quantity, the redshift z. It should be noted that in general the above integral has no analytic solution. Rather, the integral is solved

numerically for a specific set of cosmological parameters. That equation 1.7 has different cases depending on the curvature of the universe makes numerically solving the integral fairly bothersome. Rather, what is done in practise is to either restrict oneself to deal with only the case where the universe is flat, or work with a Taylor expansion of equation 1.7. Another simplification of equation 1.24 is to define

$$E(z) = \frac{H(z)}{H_0}, \tag{1.25}$$

which in turn allows us to rewrite equation 1.24 to

$$\chi(z) = \sqrt{\Omega_{k,0}} \int_0^z \frac{dz'}{E(z')}, \tag{1.26}$$

which more clearly reveals that $\chi(z)$ is indeed unitless. See King et al. (2013) for a reference where this is done in practise.

In equation 1.9 we chose to include the cosmological constant, Λ, as an explicit term rather than including it in the energy density ε. Rather than serving the original purpose of keeping the universe static, in the modern interpretation Λ serves as a source of accelerated expansion of the universe at late times. This accelerated expansion was observed by Riess et al. (1998) and Perlmutter et al. (1999) who observed type Ia supernovae in the nearby universe at low redshift and up to a redshift of $\sim$1. The Hubble diagram that shows that the cosmology with a non-zero cosmological constant best fit the data of Riess et al. (1998) is shown in figure 1.7.

1.3.1 Modifications to standard cosmology

The cosmology introduced in the above section is referred to as either standard or ΛCDM cosmology. ΛCDM has been successful at explaining observations of not only type Ia supernovae but also the cosmic microwave background, baryon acoustic oscillations and more. Issues still remain, such as a discrepancy between the Hubble constant measurements from local probes, such as Ia supernovae and baryon acoustic oscillations, and high redshift probes like the cosmic microwave background. Therefore alternatives to the standard ΛCDM model have been proposed. They broadly fall into two categories, either modifying ΛCDM through e.g. the equation of state of dark energy or through altering the underlying assumptions by modifying general relativity. In the second category a common modification of general relativity is to the Ricci scalar. The Lagrangian in the Einstein-Hilbert action is

$$S_{EH} = \frac{1}{2\kappa} \int d^4x \sqrt{-g} R, \tag{1.27}$$

where $\kappa = 8\pi G$, g is the determinant of the metric, and R is the Ricci scalar. The modification is then to turn the Ricci scalar into a general function of R,

$$S = \frac{1}{2\kappa} \int d^4x \sqrt{-g} f(R), \tag{1.28}$$

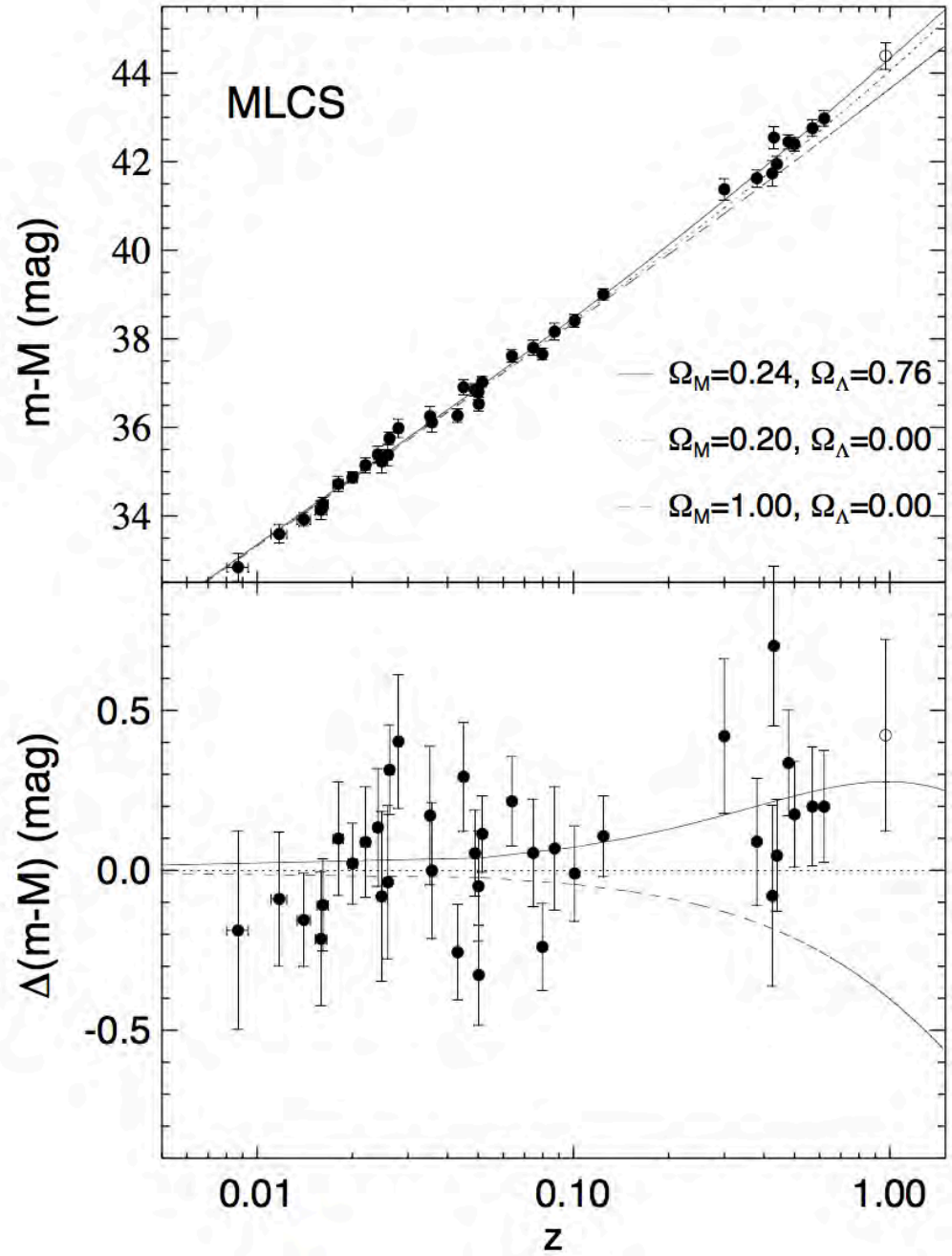

Figure 1.7: The upper panel shows the Hubble diagram for the Riess et al. (1998) sample of type Ia supernovae. Three cosmologies are overplotted, two matter only cosmologies with $\Omega_m = 0.2$ and $\Omega_m = 1$ respectively as well as the best fit flat $\Omega_m = 0.24$, $\Omega_\Lambda = 0.76$ cosmology. The bottom panel shows residuals for all three cosmologies compared with the $\Omega_m = 0.2$ cosmology. Reproduced from Riess et al. (1998).

where $f(R)$ is an arbitrary function of R. This family of models is known as $f(R)$ models (Buchdahl, 1970; Sotiriou and Faraoni, 2010). A motivation for $f(R)$ gravity is that it can lead to the observed accelerated expansion of the universe without having an explicit dark energy term. A few assumptions are typically made to simplify the notation. The first is describing matter as a perfect fluid with stress-energy tensor

$$T^{\mu\nu} = (\rho + P)u^{\mu}u^{\nu} + Pg^{\mu\nu}, \tag{1.29}$$

in tensor notation, where u^{μ} is the four velocity of an observer moving with the fluid and ρ and P are the energy density and pressure of the fluid, respectively. The second assumption is to assume a spatially flat universe, e.g. $\Omega_k = k = 0$. This does of course restrict the model to be applicable only when this assumption is true, however in practise this limitation is not a strong one. This is because observational evidence is in agreement with a flat universe, and any deviation from this flatness will have to be relatively small. Any deviation that exists between the solution where flatness is assumed and where it is not would therefore disappear as $\Omega_k \to 0$. With these assumptions the Hubble parameter in $f(R)$ gravity models can be written as

$$H^2 = \frac{\kappa}{3f'}\left(\rho + \frac{Rf' - f}{2} - 3H\dot{R}f''\right), \tag{1.30}$$

where as shorthand $f = f(R)$ is used and prime denotes derivative with the function parameter. The effective pressure and density are then defined as

$$\rho_{\text{eff}} = \frac{Rf' - f}{2f'} - \frac{3H\dot{R}f''}{f'}, \tag{1.31}$$

and

$$P_{\text{eff}} = \frac{\dot{R}^2 f''' + 2H\dot{R}f'' + \ddot{R}f'' + (f - Rf')/2}{f'}. \tag{1.32}$$

From the definition of the equation of state we can therefore write

$$w_{\text{eff}} = \frac{P_{\text{eff}}}{\rho_{\text{eff}}} = \frac{\dot{R}^2 f''' + 2H\dot{R}f'' + \ddot{R}f'' + (f - Rf')/2}{(Rf' - f)/2 - 3H\dot{R}f''} \tag{1.33}$$

for the effective equation of state of the fluid, where appropriate parameters will then yield $w_{\text{eff}} \approx -1$.

The purpose of $f(R)$ gravity models is to provide a phenomenological modification of general relativity which enables the introduction of higher order terms in the gravity model. From working with $f(R)$ models we can gain understanding for the effects of these modifications, and fitting these models to the available data allows us to focus on models that are in agreement with observations. See e.g. Adams and Blake (2017) for an excellent introduction to $f(R)$ gravity in practise.

Another modification of standard ΛCDM cosmology is to allow the equation of state of dark energy, w_Λ, to depart from being -1. The simplest modification is to allow w_Λ to have another value

than -1, but still remain a constant as a function of time. This cosmology is typically referred to as a wCDM cosmology. A higher order modification is then to introduce an extra parameter that enables w_Λ to vary as a function of redshift. Combined this family of models with varying w_Λ are typically referred to as w_zCDM or w_aCDM cosmologies, depending on whether the redshift or the scale factor is used. These modifications are like $f(R)$ gravity phenomenological in nature. The purpose of these modifications is to test the assumption of whether dark energy truly is constant or whether there is some evolution with redshift. With current data it is not possible to derive tight constraints on the cosmological parameters if more than two additional parameters are added, so therefore for the purpose of learning about the nature of dark energy we shall here restrict ourselves to look at models for w_Λ with a maximum of two free parameters. A multitude of these models exist, here we will list the ones that are referenced the most in current literature but this list is not meant to be exhaustive. A model that is popular is the CPL (Chevallier and Polarski, 2000; Linder, 2003) model which is defined as

$$w(z) = w_0 + w_a \frac{z}{1+z}. \tag{1.34}$$

Other models include the BA (Barboza and Alcaniz, 2012) model,

$$w(z) = w_0 + w_a \frac{z(1+z)}{1+z^2}, \tag{1.35}$$

the Sine model (Lazkoz et al., 2010),

$$w(z) = w_0 + w_a \sin z, \tag{1.36}$$

the logarithmic (Feng et al., 2011) model,

$$w(z) = w_0 + w_a \ln(1+z), \tag{1.37}$$

MZ model 1,

$$w(z) = w_0 + w_a \left(\frac{\ln(2+z)}{1+z} - \ln 2 \right), \tag{1.38}$$

and MZ model 2,

$$w(z) = w_0 + w_a \left(\frac{\sin(1+z)}{1+z} - \sin 1 \right), \tag{1.39}$$

both by Ma and Zhang (2011). The FSLL model 1,

$$w(z) = w_0 + w_a \frac{z}{1+z^2}, \tag{1.40}$$

FSLL model 2,

$$w(z) = w_0 + w_a \frac{z^2}{1+z^2}, \tag{1.41}$$

both by Feng et al. (2012). The linear model (Cooray and Huterer, 1999),

$$w(z) = w_0 + w_a z, \tag{1.42}$$

the JBP model (Jassal et al., 2004),

$$w(z) = w_0 + w_a \frac{z}{(1+z)^2}, \tag{1.43}$$

and the 7CPL model (Pantazis et al., 2016),

$$w(z) = w_0 + w_a \left(\frac{z}{1+z}\right)^7, \tag{1.44}$$

which is the specific case where $n = 7$ of the nCPL (Pantazis et al., 2016) model,

$$w(z) = w_0 + w_a \left(\frac{z}{1+z}\right)^n. \tag{1.45}$$

For a recent review of the status of both modified gravity and w_zCDM cosmologies see Joyce et al. (2016).

1.4 Peculiar Velocities and Bulk Flows in Cosmology

Peculiar velocities of type Ia supernovae are for most supernova cosmologists a nuisance and a source of systematics uncertainty. If sufficient peculiar velocities are measured however, it allows us to probe the local bulk flow. The local bulk flow is determined by fluctuations in the density field, which in turn is determined by the assumed model for gravity and cosmological parameters such as σ_8 and $\Omega_{m,0}$. So by measuring the local bulk flow we can constrain these cosmological parameters. The seminal works on the topic are Peebles (1994) and Coles and Lucchin (2013).

It is useful to first define the necessary mathematical notation to describe fluctuations in the density field before progressing to the velocity field, as the velocity field is directly given by the density field (and some assumed gravitation, which we will not discuss here, but instead assume general relativity to hold true). If we wish to describe the distribution of matter in the universe, we might imagine first subdividing the universe into areas that are evolving independently of one another. As time progresses however, these areas will eventually not be independent of one another. It is therefore advantageous to think of the fluctuations in the density field as a superposition of plane waves which in the limit where the fluctuations are linear evolve independently. This allows us to describe the density field as a superposition of individual components in Fourier space rather than real space. This is often referred to as $\mathbf{k}$-space, as the variable used is $\mathbf{k} = 2\pi/\mathbf{r}$, rather than the real space distance $\mathbf{r}$. Let us now consider a volume V that is bigger than the largest structures that exist in the universe. The density of this volume at point $\mathbf{r}$ is then $\rho(\mathbf{r})$ and the mean density is denoted $\langle\rho\rangle$. We typically want to quantify how the density field deviates from this mean value at a specific point. These fluctuations from the mean are therefore defined as

$$\delta(\mathbf{r}) = \frac{\rho(\mathbf{r}) - \langle\rho\rangle}{\langle\rho\rangle}. \tag{1.46}$$

Again going to the limit where the fluctuations evolve linearly we can then express these fluctuations as a Fourier series

$$\delta(\mathbf{r}) = \sum_{\mathbf{k}} \delta_{\mathbf{k}} \exp\left(i\mathbf{k}\cdot\mathbf{r}\right) \tag{1.47}$$

where the coefficients $\delta_{\mathbf{k}}$ are given by

$$\delta_{\mathbf{k}} = \frac{1}{V}\int_V \delta(\mathbf{r}) \exp\left(-i\mathbf{k}\cdot\mathbf{r}\right)\mathrm{d}\mathbf{r}. \tag{1.48}$$

Let us suppose we calculate the coefficients $\delta_{\mathbf{k}}$ for the volume V. We then proceed to do the same, but for a different volume of equal size to V. For this new volume the Fourier coefficients will differ from those derived for V. If repeated enough times, we can from this thought experiment determine the variance of the Fourier coefficients. These will be related to the variance of the density fluctuations, $\sigma^2 = \langle\delta(\mathbf{r})^2\rangle$, through

$$\sigma^2 = \langle\delta(\mathbf{r})^2\rangle = \sum_{\mathbf{k}} \langle|\delta_{\mathbf{k}}|^2\rangle. \tag{1.49}$$

Note here that by definition the $\langle\delta(\mathbf{r})\rangle^2$ term is zero and omitted from the expression above. If we now assume that the density field is statistically isotropic and homogeneous the direction of $\mathbf{k}$ can be ignored and we can therefore write $k = |\mathbf{k}|$ and modify the above expression to

$$\sigma^2 = \langle\delta(\mathbf{r})^2\rangle = \frac{1}{V}\sum_{\mathbf{k}} \delta_k^2, \tag{1.50}$$

which in the limit where $V \to \infty$ becomes

$$\lim_{V\to\infty} \frac{1}{V}\sum_{\mathbf{k}} \delta_k^2 = \frac{1}{2\pi^2}\int_0^\infty P(k)k^2\mathrm{d}k, \tag{1.51}$$

where $P(k)$ is the matter powerspectrum of the density field. While equation 1.51 is correct and applicable at the largest scales, it is not useful by itself in the context of peculiar velocities which we can only measure at smaller scales. We shall therefore use the same logic to build a statistical description of the density field at some scale R. We let $\langle M\rangle$ be the mean mass found inside a sphere with volume V and radius R. The mass variance over multiple independent spherical volumes of size V is then given by

$$\sigma_M^2 = \frac{\langle(M - \langle M\rangle)^2\rangle}{\langle M\rangle^2}. \tag{1.52}$$

Using the same reasoning as for equation 1.47 we can decompose this into a Fourier series and then let the volume tend towards infinity. This yields an expression for the mass variance of the form

$$\sigma_M^2 = \sum_{\mathbf{k}} \langle|\delta_{\mathbf{k}}|^2\rangle \left(\frac{1}{V}\int_V \exp\left(i\mathbf{k}\cdot\mathbf{r}\right)\right)^2. \tag{1.53}$$

To further simplify this equation we can decompose $\exp(i\mathbf{k}\cdot\mathbf{r})$ in spherical harmonics

$$\exp(i\mathbf{k}\cdot\mathbf{r}) = \sum_{l,m} j_l(kr) i^l (2l+1) P_l^{|m|}(cos\nu \exp(im\varphi), \tag{1.54}$$

where l and m are the degree and order of the spherical Bessel functions j_l and the associated Legendre polynomials $P_l^{|m|}$ respectively. r, ν, and φ are spherical polar coordinates. We can then insert this decomposition into the integral of equation 1.53 which yields

$$\int_V \exp(i\mathbf{k}\cdot\mathbf{r}) = \sum_{l,m} i^l(2l+1) \int_0^{2\pi} \exp(im\varphi)\mathrm{d}\varphi \int_0^{\pi} P_l^{|m|}(\cos\nu)\sin\nu\mathrm{d}\nu \int_0^R j_l(kr) r^2 \mathrm{d}r \tag{1.55}$$

$$= 4\pi \int_0^R j_0(kr) r^2 \mathrm{d}r = \frac{4\pi}{k^3}(\sin(kR) - kR\cos(kR)). \tag{1.56}$$

We here used that the integrals over ν and φ are zero unless $m = l = 0$ and that the 0'th spherical Bessel function is given by

$$j_0(x) = \frac{\sin x}{x}. \tag{1.57}$$

Motivated by the above result we define the window function $W(kR)$ as

$$W(kR) = \frac{3(\sin(kR) - kR\cos(kR))}{(kR)^3}, \tag{1.58}$$

which then allows us to rewrite equation 1.53 as

$$\sigma_M^2 = \frac{1}{V}\sum_{\mathbf{k}} \delta_k^2 W^2(kR), \tag{1.59}$$

which in the limit where $V \to \infty$ is

$$\lim_{V\to\infty} \frac{1}{V}\sum_{\mathbf{k}} \delta_k^2 W^2(kR) = \frac{1}{2\pi^2}\int_0^{\infty} P(k) W^2(kR) k^2 \mathrm{d}k. \tag{1.60}$$

Extending this argument to velocities we find that the velocity variance can be expressed as

$$\sigma_v^2(R) = \frac{H_0^2 f^2}{2\pi^2}\int_0^{\infty} P(k) W^2(kR)\mathrm{d}k, \tag{1.61}$$

where we used that the relation between the velocity power spectrum and the matter power spectrum is given as

$$P_v(k) = H_0^2 f^2 k^{-2} P(k), \tag{1.62}$$

where $P_v(k)$ is the velocity power spectrum. The physical interpretation of the power spectrum is to describe how strongly various modes, or in physical terms scales, contribute to the velocity variance. The window function is then a description of how sensitive we are to the various modes of the power spectrum. If a measurement of the velocity variance is completely insensitive to the power spectrum modes, this will translate to the window function being zero at that particular

value of k. On the other hand, if a measurement is completely sensitive to the modes of a specific scale then the window function will take the value one at that value of k. In practice what we measure is not the variance, rather it is a bulk flow of a defined local volume with regards to the dipole subtracted cosmic microwave background rest frame. As the velocity variance is inherently statistical in nature, it is therefore also necessary to compare the measured bulk flow with the full statistical prediction from linear theory. Specifically this will be a Maxwell-Boltzmann distribution of bulk flows that are given by the velocity variance. The likelihood distribution for bulk flows take the form

$$P(v)\mathrm{d}v = \sqrt{\frac{54}{\pi}}\left(\frac{v}{\sigma_v}\right)^2 \exp\left(-\frac{3}{2}\left(\frac{v}{\sigma_v}\right)^2\right)\frac{\mathrm{d}v}{\sigma_v}. \tag{1.63}$$

Taking the derivative of equation 1.63 allows us to show that the maximum likelihood bulk flow relates to the velocity variance by

$$v_{ML}(R) = \sqrt{2/3}\sigma_v(R). \tag{1.64}$$

While the most likely bulk flow can be of interest, it does not encapsulate the entirety of the theoretical prediction. When determining whether an observed bulk flow is in agreement with the theoretical prediction it is therefore necessary to fold the likelihood distribution of equation 1.63 into the statistical analysis.

Chapter 2

Reconciling Volumetric and Individual Galaxy Type Ia Supernova Rates

This chapter contains the paper "Reconciling volumetric and individual galaxy type Ia supernova rates" by Andersen, P. and Hjorth, J., 2018, arXiv:1801.00793

2.1 Abstract

Significant observational effort has been devoted to determining volumetric type Ia supernova rates at high redshifts, leading to clues about the nature of Ia supernova progenitors and constraints on the iron production in the universe. A complementary approach is to investigate type Ia supernova rates in individual, more nearby, galaxies. The popular A+B model for the specific supernova rate, while reliable for a wide range of galaxy properties, diverges for large specific star formation rates. Applying it outside its range of validity could lead to the prediction of excessive type Ia supernova rates. Moreover, the A+B model it is not directly derived from a delay time distribution. We here introduce a new model which is explicitly motivated by a simple delay time distribution composed of a prompt and a delayed component. The model is in remarkably good agreement with current observational constraints. It yields a prompt fraction of $f_p = 0.11^{+0.10}_{-0.06}$ in agreement with results based on volumetric rates of type Ia supernovae at high redshift (Rodney et al., 2014). The model is tested against realistic star formation rates from the Illustris-1 simulation and is found to be self consistent in the asymptotic limits. An analytic function that encapsulates the features of the new model is shown to be in excellent agreement with the data. In terms of goodness of fit, the new model is strongly preferred over the A+B model. At $\log(\mathrm{sSFR}) \gtrsim -9$ there are no constraints from observations. Observations in this regime will further constrain the delay time distribution of type Ia supernovae at short delay times.

2.2 Introduction

Type Ia supernovae (SNe) play a central role in modern astronomy. As standardisable candles they have been used to determine the apparent accelerated expansion of the universe (Riess et al.,

1998; Perlmutter et al., 1999). In the chemical evolution of the universe they act as an important source of iron (Tsujimoto et al., 1995; Maoz and Graur, 2017). Despite their prominence, the precise physics of the Ia SNe progenitor is unknown. This is often referred to as the progenitor problem. Different models for the progenitor predict different delay time distributions (DTD). The DTD parametrises the distribution of times between the formation of the progenitor and the subsequent SN explosion. In the limit where all star formation happens instantaneously, in a brief starburst, the DTD parametrisation will reflect the rate of SN explosions that follow the starburst. In practise, the star formation history is more complex, and the observed SN rate is a convolution of the DTD and the star formation rate. This complicates modelling of SN Ia rates which plays an important role in, e.g., cosmological astrophysics and chemical evolution modelling.

Different avenues can be taken when modelling SN rates. One is to measure volumetric SN rates as a function of redshift (Totani et al., 2008; Graur et al., 2014; Rodney et al., 2014) and fit an assumed DTD. This approach seems to suggest a DTD of the form DTD $\sim \tau^{-1}$, perhaps with a transition to becoming constant at early times (e.g., Rodney et al., 2014). This may be explained by a progenitor model with two distinct progenitors. These two progenitors are often referred to as a prompt component, with short delay times, and a delayed component, with longer delays between star formation and SN explosion. Another approach is to observe SN rates for individual galaxies as a function of star formation rate of the host galaxy, averaged over all observed galaxies. This approach does not formally define or assume a DTD, and instead assumes that the SN rate depends on physical parameters such as stellar mass and star formation rate of the host galaxy. The consensus model for this approach is the A+B model (Mannucci et al., 2005; Scannapieco and Bildsten, 2005), which, in the simplest form, relates the SN Ia rate linearly to the stellar mass and the star formation rate, i.e.,

$$\mathrm{SNR} = A\ M_* + B\ \mathrm{SFR}, \tag{2.1}$$

where SNR is the SN rate, M_* is the stellar mass, and SFR is the star formation rate. A and B are then the two free parameters of the model, with units of SNe yr^{-1} $M_\odot^{-1}$ and SNe yr^{-1}$(M_\odot\ \mathrm{yr}^{-1})^{-1}$ respectively. Often the stellar mass is eliminated from the above equation by dividing through with M_*, which in turn yields

$$\mathrm{sSNR} = A + B\ \mathrm{sSFR}, \tag{2.2}$$

where $\mathrm{sSNR} = \mathrm{SNR}/M_*$ is the specific supernova rate and $\mathrm{sSFR} = \mathrm{SFR}/M_*$ is the specific star formation rate. Alternatives to the A+B model of Scannapieco and Bildsten (2005) exist, see e.g. Smith et al. (2012) for a generalisation of the A+B model or Graur et al. (2015b) where a simple τ^{-1} DTD is combined with galaxy 'downsizing' to model specific supernova rates.

In Scannapieco and Bildsten (2005) the A+B model is motivated by an observed bimodal distribution of type Ia SNe luminosities; they argue that the brightest SNe are more prevalent in actively star forming galaxies while underluminous events occur primarily in galaxies with low star formation rates. Wang et al. (1997) and Hakobyan et al. (2016) additionally find that in star forming galaxies, type Ia SNe occur more often in the disk than in the bulge, which suggests that

the Ia rate is somehow dependent on recent star formation. Mannucci et al. (2006) furthermore argue that their finding that only DTDs including both a prompt and a delayed component are consistent with observations suggests that there exists two classes of Ia progenitors. Rodney et al. (2014) fit a DTD that includes a prompt and delayed component, and find that this model fits the $z < 1$ volumetric rates well with a prompt fraction of $f_p = 0.53^{\pm 0.09}_{\text{stat}}{}^{\pm 0.10}_{\text{sys}}$. At redshifts of $z > 1$ they find comparatively fewer Ia SNe, and a prompt fraction of $f_p = 0.21^{\pm 0.34}_{\text{stat}}{}^{\pm 0.49}_{\text{sys}}$, which they argue is an indication that prompt progenitors might be less numerous than the $z < 1$ sample suggests. The picture emerging from these studies is that the mechanism responsible for Ia explosions can have two channels, one prompt and one delayed, and that both contribute significantly to the observed supernova rate.

In this work we attempt to reconcile the approach using volumetric rates and the approach using individual rates. To do so we will assume a DTD functionally similar to the one adopted by Rodney et al. (2014). From this DTD we derive a model for the supernova rate as a function of star formation rate, and compare it to the A+B model. Additionally, from the functional form of the new model we will develop a simple expression that will predict supernova rates in the high redshift and high specific star formation regime.

The paper is structured as follows. First, in section 2.3, we derive a new model for the relation between sSNR and sSFR. In section 2.4 we discuss the currently available data and describe the data set used in this work. In section 2.5 we discuss the complications in fitting the models to the data, and proceed to fit both our new model and an A+B model. The results, including goodness of fit, using reduced χ^2 and Kolmogorov–Smirnov tests, are presented in section 2.6. In section 2.7 we validate that the model is self consistent in the limits of high and low sSFR using realistic star formation histories from the Illustris-1 simulation. Finally, in section 2.8, we discuss the applicability of the models in the high sSFR/high redshift regime and provide recommendations for how the new model can be used in practice.

2.3 Models

For clarity, we denote all times in this work that relate to the DTD with τ, all times related to SNR with t, while galaxy ages are denoted with an upper case T.

2.3.1 Piecewise model

Delay Time Distribution There is strong evidence for a DTD that follows a power law of τ^{-1}, see e.g. Maoz and Mannucci (2012) or Maoz et al. (2014), Fig. 8. In Rodney et al. (2014) a three-branched DTD is defined, as being zero up to 0.04 Gyr, then constant up to 0.5 Gyr, and finally declining as τ^{-1} for $\tau > 0.5$ Gyr. This corresponds to some fraction of the SNe making up a prompt fraction, and some a delayed fraction. Formally, the DTD of Rodney et al. (2014) takes

the form

$$\mathrm{DTD}(\tau) = \begin{cases} 0 & \text{for } \tau < \tau_0 \\ k_1 & \text{for } \tau_0 \leq \tau \leq \tau_1 \\ k_2 t^{-1} & \text{for } \tau_1 < \tau, \end{cases} \tag{2.3}$$

with (τ_0, τ_1) = (0.04 Gyr, 0.5 Gyr). For simplicity we neglect the zero part the DTD where $\tau < \tau_0$. This is equivalent to assuming that $\tau_0 = 0$. This has no strong impact as this DTD does not diverge as $\tau \to 0$. The DTD used throughout this work is therefore defined as

$$\mathrm{DTD}(\tau) = \begin{cases} k_1 & \text{for } \tau \leq \tau_1 \\ k_2 \tau^{-1} & \text{for } \tau_1 < \tau. \end{cases} \tag{2.4}$$

In the following we will derive the SNR in three regimes. For all regimes we apply the definition

$$\mathrm{SNR}(t) = \int_{t_a}^{t_b} \mathrm{SFR}(t-\tau)\mathrm{DTD}(\tau)\mathrm{d}\tau, \tag{2.5}$$

where the limits t_a and t_b are set such that $\mathrm{SNR}(t)$ is positive. As both $\mathrm{SFR}(t-\tau)$ and $\mathrm{DTD}(\tau)$ are positive, this means that the limits must be set such that $t_b > t_a$.

Short Duration Starburst at Early Times

We consider a galaxy with age T_a where the star formation takes place from T_a to $T_a - \Delta T$ in a short starburst of duration ΔT where $\Delta T \ll T_a$. Since we observe at late times, only the τ^{-1} component of the DTD is relevant. This yields

$$\begin{aligned} \mathrm{SNR}(t) = & \int_{T_a - \Delta T}^{T_a} \mathrm{SFR}(t-\tau) k_2 \tau^{-1} \mathrm{d}\tau \\ = & -\int_{T_a}^{T_a - \Delta T} \mathrm{SFR}(t-\tau) k_2 \tau^{-1} \mathrm{d}\tau \\ = & -k_2 \mathrm{SFR} \ln \frac{T_a - \Delta T}{T_a} \approx k_2 \mathrm{SFR} \frac{\Delta T}{T_a} \\ = & \frac{k_2}{T_a} M_*, \end{aligned} \tag{2.6}$$

where in the third line we Taylor expanded to first order and in the fourth line used that the product of the star formation rate and a time interval is the stellar mass produced. Additionally we assumed that the SFR is constant over the integrated time period, which is a valid assumption as $\Delta T \ll T_a$.

Recent Starburst

For a recent starburst at late times where $\tau < \tau_1$ the constant term of the DTD dominates, yielding

$$\mathrm{SNR}(t) = \int_0^t \mathrm{SFR}(t-\tau) k_1 \mathrm{d}\tau = \mathrm{SFR}\, k_1\, t, \tag{2.7}$$

when assuming that the SFR is constant over the integrated time, which for a recent starburst is a good approximation. Dividing equation 2.7 through by the mass M_* it yields

$$\mathrm{sSNR} = \mathrm{sSFR}\ k_1\ t. \tag{2.8}$$

In the recent starburst limit $sSFR \approx t^{-1}$. This follows from the relation between the mass M_* and SFR,

$$M_* = \int_0^t \mathrm{SFR}\,\mathrm{d}t = \mathrm{SFR}\,t, \tag{2.9}$$

and from the definition of the sSFR ,

$$\begin{aligned} \mathrm{sSFR} &= \frac{\mathrm{SFR}}{M_*} \\ &= t^{-1}. \end{aligned} \tag{2.10}$$

Inserting the result of equation 2.10 into equation 2.8 yields

$$\mathrm{sSNR} = k_1 \tag{2.11}$$

for $\tau < \tau_1$, i.e., the specific supernova rate tends to a constant at high sSFR. k_1 can in principle be measured directly by counting the number of SNe in high sSFR galaxies. This also gives a direct measurement of the prompt fraction, defined as

$$\begin{aligned} f_p &= \frac{\int_0^{t_1} k_1 \mathrm{d}t}{\int_0^{t_1} k_1 \mathrm{d}t + \int_{t_1}^{t_2} k_2 t^{-1} \mathrm{d}t} \\ &= \frac{k_1 t_1}{k_1 t_1 + k_2 \ln(\frac{t_2}{t_1})} \end{aligned} \tag{2.12}$$

where we follow Rodney et al. (2014) in denoting the prompt fraction f_p.

Intermediate Times

Above we derived the SNR in the early and late asymptotic limits. At intermediate times both the prompt and delayed component contribute. If we, for the sake of argument, assume that the SFR can be treated as a constant, then

$$\begin{aligned} \mathrm{SNR}(t) &= \int_0^{t_2} \mathrm{SFR}(t-\tau)\mathrm{DTD}(\tau)\mathrm{d}\tau \\ &= \int_0^{t_1} \mathrm{SFR}(t-\tau)k_1 \mathrm{d}\tau + \int_{t_1}^{t_2} \mathrm{SFR}(t-\tau)k_2\tau^{-1}\mathrm{d}\tau \\ &= \mathrm{SFR}\ (k_1 t_1 + k_2 \ln\frac{t_2}{t_1}). \end{aligned} \tag{2.13}$$

Dividing through with the mass M_* gives

$$\mathrm{sSNR}(t) = \mathrm{sSFR}\ \left(k_1 t_1 + k_2 \ln \frac{t_2}{t_1}\right). \tag{2.14}$$

The result of equation 2.14 is simply the product of the sSFR and a constant. The assumption of constant SFR is poor at intermediate times, so in order to generalise the behaviour we assume a power law in sSFR of the form

$$\mathrm{sSNR}(\mathrm{sSFR}) = \alpha\ \left(\frac{\mathrm{sSFR}}{1\,\mathrm{yr}^{-1}}\right)^{\beta}, \tag{2.15}$$

where in order to have the correct units a normalisation constant of size $1\,\mathrm{yr}^{-1}$ is introduced and α carries units of SNe $\mathrm{yr}^{-1}\,M_{\odot}^{-1}$.

Putting it all Together

In the previous three sections we have suggested that the SNR is constant in the asymptotic limits and a power law at intermediate times. To parametrise this requires four free parameters, when imposing the requirement of continuity and fitting the for the transition points between the asymptotic limits and intermediate times. These four parameters are two parameters determining the constant SNR in the asymptotic limits and two parameters to fix the transition between the limits and intermediate times. To simplify the equations we utilise an equivalent but simpler parametrisation that has the transition points and then β and α from equation 2.15 as free parameters. Combining this in a continuous piecewise function yields

$$\mathrm{sSNR}(\mathrm{sSFR}) = \alpha \begin{cases} S_1 & \text{for } \mathrm{sSFR} < \mathrm{sSFR}_2 \\ \left(\frac{\mathrm{sSFR}}{1\,\mathrm{yr}^{-1}}\right)^{\beta} & \text{for } \mathrm{sSFR}_2 < \mathrm{sSFR} < \mathrm{sSFR}_1 \\ S_2 & \text{for } \mathrm{sSFR} > \mathrm{sSFR}_1, \end{cases} \tag{2.16}$$

where

$$S_1 = \left(\frac{\mathrm{sSFR}_1}{1\,\mathrm{yr}^{-1}}\right)^{\beta}, \tag{2.17}$$

$$S_2 = \left(\frac{\mathrm{sSFR}_2}{1\,\mathrm{yr}^{-1}}\right)^{\beta}, \tag{2.18}$$

and the four parameters to be fit are sSFR_1, sSFR_2, β, and α.

2.3.2 Smooth logarithm parametrisation

The model of equation 2.16 is not convenient for purposes that require a continuous differentiable model. Therefore we introduce a parametrisation that contains the same features, but is a smooth

function for all values of sSFR. It is defined as

$$\mathrm{sSNR}(\mathrm{sSFR}) = a + \frac{a}{k}\log\left(\frac{\mathrm{sSFR}}{\mathrm{sSFR}_0} + b\right), \tag{2.19}$$

where the four free parameters to be fit are a, k, sSFR_0, and b.

2.4 Data

The available type Ia supernova versus sSFR data include that of Mannucci et al. (2005), Sullivan et al. (2006), Smith et al. (2012), Gao and Pritchet (2013), Graur et al. (2015b), and Botticella et al. (2017). Sullivan et al. (2006) use type Ia observations from the Supernova Legacy Survey (SNLS) in the redshift range $0.2 < z < 0.75$. In Smith et al. (2012) type Ia SN observations are taken from the Sloan Digital Sky Survey (SDSS-II) SN Survey (Frieman et al., 2008) which observed at redshifts of $z < 0.4$. The data of Sullivan et al. (2006) and Smith et al. (2012) are analysed in a fashion that makes it straightforward to combine the two data sets. This includes assuming the same cosmology, both using AB magnitudes, binning and treating their data in a similar fashion. Other data sets exist, including those of Mannucci et al. (2005). Mannucci et al. (2005) uses the SN observations of Cappellaro et al. (1999). Gao and Pritchet (2013) use spectroscopic data from the SDSS-II sample. Graur et al. (2015b) use a SN sample from SDSS Data Release 9. The most recent data is from the SUDARE survey (Botticella et al., 2017).

To work with data based on fully consistent assumptions and treatment of the data we choose to use the combined data set of Sullivan et al. (2006) and Smith et al. (2012) in the analysis of this work. The datapoint contaminated by systematically uncertain "ridge-line" galaxies of Smith et al. (2012) is on the basis of this contamination excluded from the analysis; see Fig. 5 of Smith et al. (2012) for details.

2.5 Method

For all models we fit for maximum likelihood parameters by minimising the χ^2 function given by

$$\chi^2(\mathrm{sSFR}; P) = \sum_i \left(\frac{\mathrm{sSNR}_{\mathrm{model}}(\mathrm{sSFR}; P) - \mathrm{sSNR}_{\mathrm{data},i}}{\sigma_i}\right)^2 \tag{2.20}$$

where $\mathrm{sSNR}_{\mathrm{model}}(\mathrm{sSFR}; P)$ is the sSNR predicted by the model in question given parameters P and $\mathrm{sSNR}_{\mathrm{data},i}$ is the i'th measurement with associated uncertainty σ_i. In practise what is done is we maximise the log-likelihood function which is related to χ^2 via

$$\log\mathcal{L}(\mathrm{sSFR}; P) = \frac{-\chi^2(\mathrm{sSFR}; P)}{2}. \tag{2.21}$$

Model	Maximum Likelihood Parameters	χ^2_{reduced}	BIC	AIC	KS
A+B	$A = (4.66 \pm 0.56) \cdot 10^{-14}$, $B = (4.88^{+0.54}_{-0.52}) \cdot 10^{-4}$	3.5	36.3	35.5	0.21
Piecewise	$\beta = 0.586 \pm 0.084$, $\alpha = (1.19 \pm 2.20) \cdot 10^{-7}$,	1.2	18.0	16.4	0.048
	$\text{sSFR}_2 = (1.01 \pm 0.55) \cdot 10^{-11}$				
	$\text{sSFR}_1 = (1.04 \pm 0.41) \cdot 10^{-9}$				
Smooth log.	$a = (1.12 \pm 2.34) \cdot 10^{-13}$, $k = 0.49 \pm 1.53$,	1.3	18.4	16.8	0.036
	$\text{sSFR}_0 = (1.665 \pm 0.002) \cdot 10^{-10}$, $b = 0.73 \pm 0.99$				

Table 2.1: Tabulated maximum likelihood parameter values and test values for the A+B model and the three models developed in this work. The two models from this work all have tests values that are comparable. This is unsurprising, as the models by construction contain the same functional features. The A+B model however consistently produce worse test values than the other models. The BIC and AIC tests are of special interest here as they penalise models for including additional fitting parameters, but despite this penalty the new models still produce significantly better test results than the A+B model. The units of A and B are SNe $\text{yr}^{-1}\, M_\odot^{-1}$ and SNe $\text{yr}^{-1}(M_\odot\, \text{yr}^{-1})^{-1}$ respectively. For the piecewise model sSFR_1 and sSFR_2 carry units of yr^{-1}, α has units of SNe $\text{yr}^{-1}\, M_\odot^{-1}$ while β is unitless. For the smooth logarithm a and sSFR_0 have units of yr^{-1} while k and b are unitless.

To fit the A+B model, the EMCEE (Foreman-Mackey et al., 2013) Markov chain Monte Carlo (MCMC) implementation was used to determine the maximum likelihood parameters utilising the log-likelihood function of Eq. 2.21. For the new models developed in this work the EMCEE MCMC approach is unfortunately not viable. The reason is that the likelihood space contains a large number of local extrema. This causes the peaks in the one dimensional marginalised likelihoods to be a combination of different extrema of the likelihood space for different parameters, resulting in parameters that are a poor fit to the model. Therefore another approach is used for these models where the log-likelihood is calculated for values in a discrete grid in the parameter space of the model in question. From the grid of likelihoods the global maximum likelihood parameters are then extracted. Since the likelihood space is highly degenerate it is difficult to associate simple uncertainties to the maximum likelihood parameters without imposing strict priors, which would result in prior driven uncertainties. We apply the Fisher information matrix method (see Albrecht et al. (2006) or King et al. (2014) for an introduction to Fisher matrix methodology) to estimate uncertainties on the maximum likelihood parameters. The Fisher matrix method is a second order approximation of the likelihood and assumes Gaussian measurement uncertainties. The Fisher matrix method will yield the best theoretically possible statistical uncertainties, and neglects contributions from non-Gaussianity and systematics. More details on how the models introduced in this work are fit and links to the fitting and analysis code can be found in appendix H.

To test the quality of the model fits we calculate the reduced χ^2, Bayesian information criterion (BIC), Akaike information criterion (AIC), and perform the Kolmogorov-Smirnov (KS) test for each model fit. The reduced χ^2 is defined as

$$\chi^2_{\text{reduced}} = \frac{\chi^2}{\nu} \tag{2.22}$$

where ν represents the degrees of freedom, given by $\nu = N - n_p$ where N is the number of data points and n_p is the number of free parameters. The BIC is defined as

$$BIC = \chi^2 + n_p \cdot \log N \tag{2.23}$$

and the AIC as

$$AIC = \chi^2 + 2\, n_p. \tag{2.24}$$

2.6 Results

We apply the method of section 2.5 to produce the fits shown in figure 2.1. The details of the fits and test values are listed in table 2.1.

The derived maximum likelihood parameters of $A = (4.66 \pm 0.56) \cdot 10^{-14}$ and $B = (4.88^{+0.54}_{-0.52}) \cdot 10^{-4}$ for the A+B model are consistent with those in the literature, see e.g. figure 1 of Gao and Pritchet (2013). Further fit details are available in figure 2.2. Table 2.1 shows that the A+B model provides the worst fit of the ones tested in this work for all test cases; reduced χ^2, BIC, AIC, and KS test. Especially the BIC and AIC are of interest here, as they contain a penalty for including additional free parameters; in this way they test whether including the additional parameters is justified. Both models developed in this work yield test values that are similar within the random noise that is expected when deriving reduced χ^2 values. This noise is simply a product of the uncertainty in each measurement, which in turn causes the reduced χ^2 value itself to be uncertain. It is unsurprising that the two models developed in this work yield so similar test results, as they by construction contain the same overall functional shape. From figure 2.1 this constructed similarity is apparent.

Our findings are in agreement with Smith et al. (2012) who find that the assumed linear relation of the A+B model provides a poor fit to data. Rather they find that a relation of $\mathrm{SNR} \propto M_*^{0.68}$ is preferred. Gao and Pritchet (2013) furthermore find that the A+B model provides a poor fit to their data and show that there exists tension between A+B model parameter estimates in the literature, although the tension is weak as the uncertainties are relatively large (see Figure 1 of Gao and Pritchet (2013)). Both of these studies indicate that there is some behaviour that the A+B model does not capture, and that additional fitting parameters are needed to adequately model the Ia supernova rates.

2.7 Comparison with Simulations

Assuming constant sSFR in section 2.3 will not hold true for all regimes of the piecewise model. In this section we test what the transition between the asymptotic limits looks like for realistic

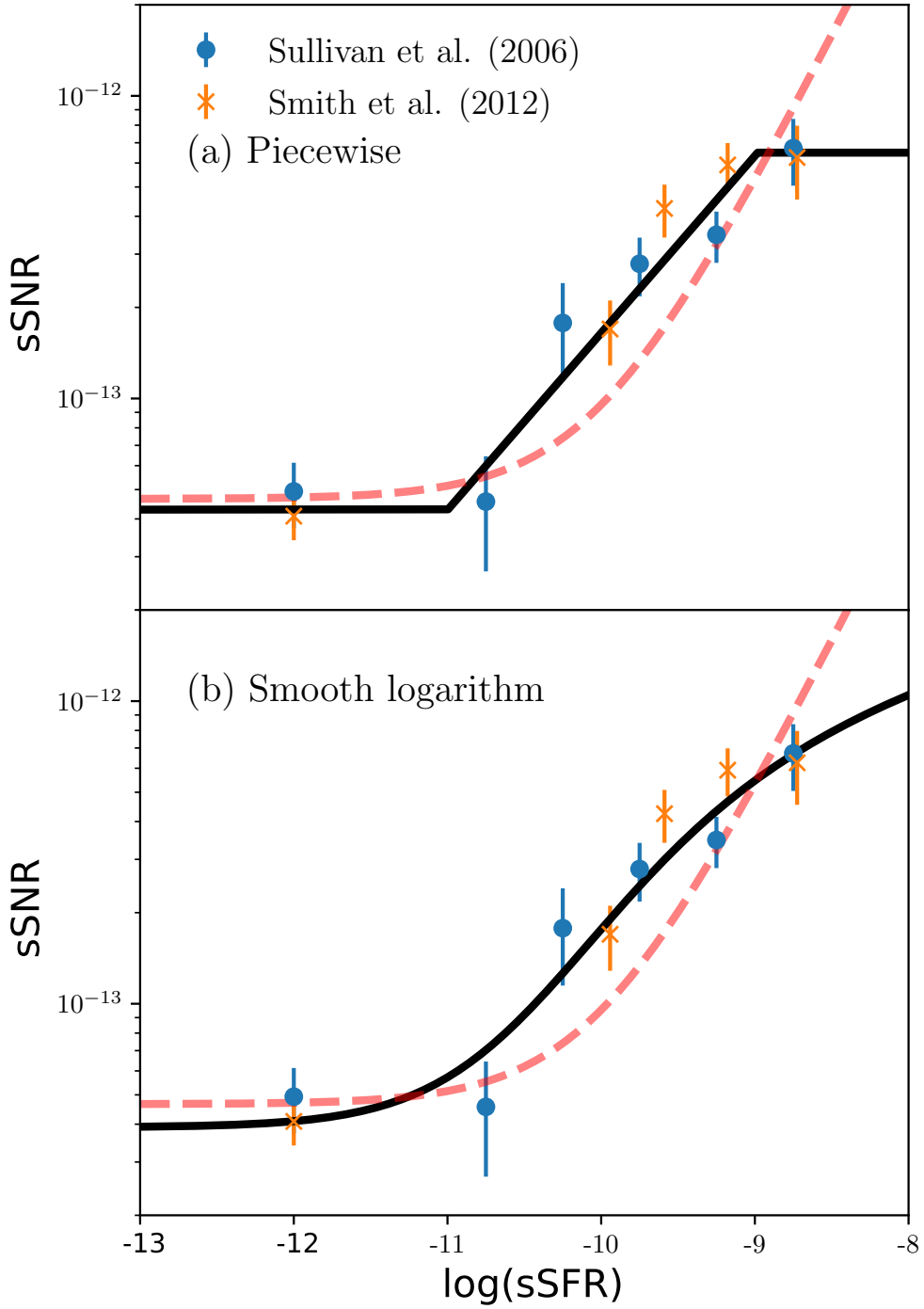

Figure 2.1: The piecewise and smooth logarithm maximum likelihood parameter fits plotted against the Sullivan et al. (2006) and Smith et al. (2012) data as well as the maximum likelihood AB model plotted as the dashed red line. The used parameters are shown in table 2.1. The plots show that the two models defined in this work are functionally similar, and that the A+B model increasingly deviates from these models at larger values of sSFR. As there is no data to constrain models at $\log(\mathrm{sSFR}) > -9$ the sSNR in this regime is associated with large uncertainty and is strongly model dependent. In terms of goodness of fit (results shown in table 2.1) both the piecewise and smooth logarithm models outperform the A+B model.

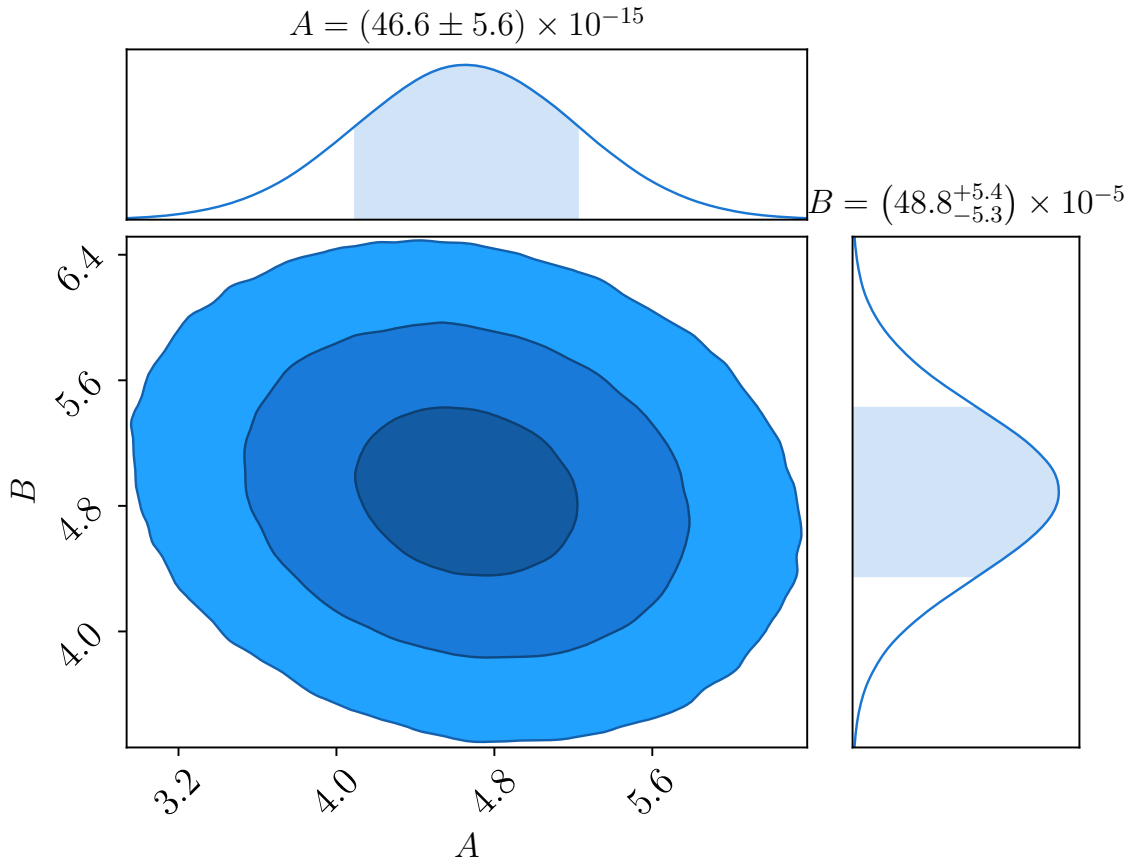

Figure 2.2: The corner plot from fitting the A+B model to the combined data set of Sullivan et al. (2006) and Smith et al. (2012) using the EMCEE MCMC tool. It is apparent from the contour plot, showing one, two, and three sigma uncertainties, that there is some mild covariance between the fitted parameters. The units of A and B are SNe $\mathrm{yr}^{-1}\, M_{\odot}^{-1}$ and SNe $\mathrm{yr}^{-1}(M_{\odot}\,\mathrm{yr}^{-1})^{-1}$ respectively. This figure was created using the CHAINCONSUMER package of Hinton (2016).

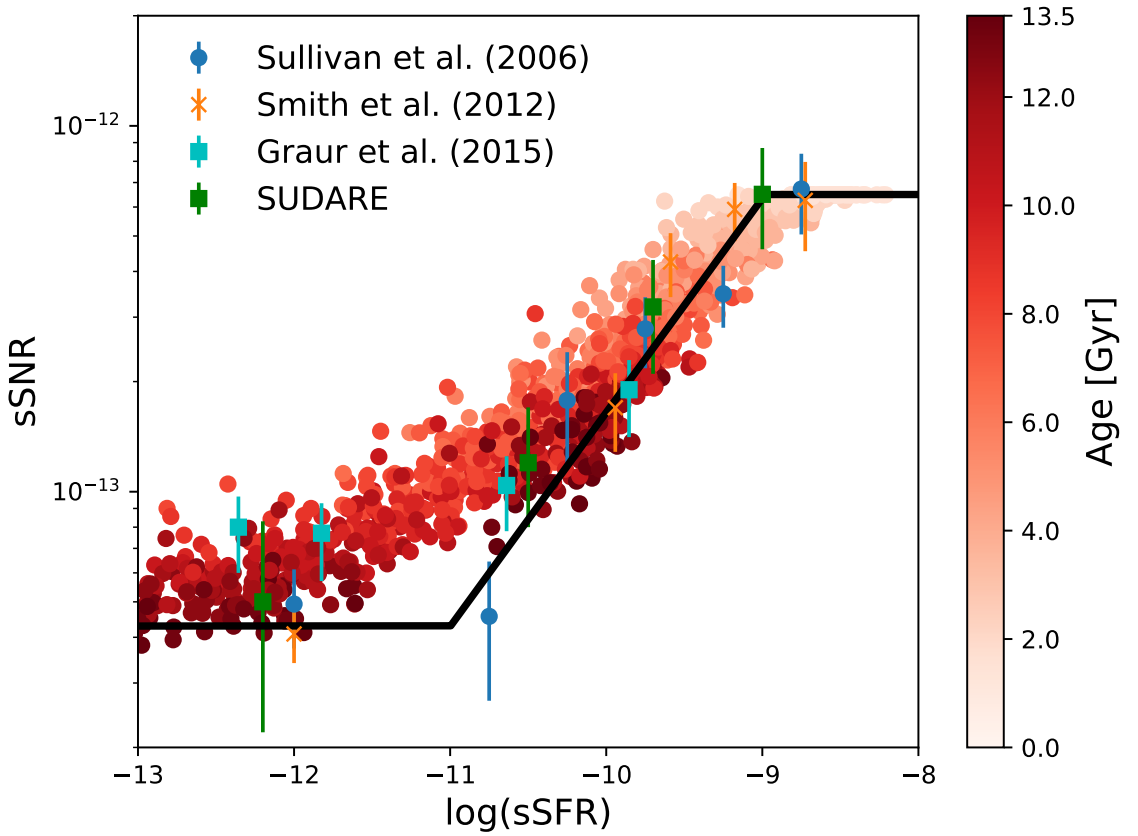

Figure 2.3: The red shaded dots show sSFR versus sSNR for star formation histories of simulated Illustris galaxies at discrete times in the range 1 Gyr to 13.7 Gyr. The colourbar shows the relation between colour and age, the redder the older the galaxy. The specific supernova rate is calculated for each galaxy using equation 2.5 where the DTD of equation 2.4 is assumed with the best fitting parameters for the piecewise model from table 2.1. The observations of Sullivan et al. (2006), Smith et al. (2012), Graur et al. (2015b), and SUDARE (Botticella et al., 2017) as well as the best fitting piecewise model to the observation of Sullivan et al. (2006) and Smith et al. (2012) is overplotted for comparison.

star formation histories. The applied approach is to determine the sSNR and sSFR for a number of galaxies with more realistic star formation rates using equation 2.5 and compare them with the predictions of the piecewise model. A source of realistic star formation histories can be found in the Illustris simulation (Vogelsberger et al., 2014a,b; Genel et al., 2014). Illustris is a hydrodynamical simulation going beyond simulating only the gravity of dark matter particles and also includes baryonic physics. Modelling gas and galaxies using computational fluid dynamics enables the Illustris simulation to predict the properties of the galaxies in the (106.5 Mpc)^3 large simulated volume. From 29,276 Illustris-1 galaxies with $M_* > 10^9 M_\odot$ a subsample of 100 galaxies is chosen such that galaxies from all mass ranges are represented. This data collection is based on the analysis tools from Sparre et al. (2015) and Diemer et al. (2017). For each galaxy the SFR as a function of time is extracted, and convolved in equation 2.5 with the DTD of equation 2.4 to produce supernova rates at discrete times ranging from 1 Gyr to 13.7 Gyr. Deriving the mass of the galaxy at each of these discrete times using

$$M_* = \int_0^t \mathrm{SFR}(t')\mathrm{d}t' \tag{2.25}$$

allows us to determine the specific star formation and specific supernova rates. The results are shown as the red shaded dots in figure 2.3. The shading of the dot indicates age, with darker shades meaning older galaxies. It is apparent that in the limits of very high or very low specific star formation rate the Illustris galaxies tends to the same specific supernova rates as the piecewise model. The exact values of specific supernova rate that the sample tends towards is a function of the assumed DTD parameters. If higher or lower k_1 and k_2 parameters were given as input in equation 2.4 this would be reflected in the limits the galaxies in figure 2.3 tend towards. As the piecewise function is fit to the observed data it captures the features therein, rather than the features of the Illustris galaxies. When the observations deviate from the Illustris results the piecewise model that best fits these observations will do the same. The reason for the slight discrepancy between Illustris and observations could be that a significant fraction of the stellar mass of galaxies is accreted rather than formed in situ. This additional mass from accretion is not taken into account when using equation 2.25 to determine the stellar mass. Figure 3 of Rodriguez-Gomez et al. (2016) shows that the accreted fraction is in the range of 0% for galaxies of mass $10^9 M_\odot$ to 80% for galaxies of mass $10^{12} M_\odot$. Another effect which can influence the mass of the galaxies is mass loss through massive stars dying and leaving remnant stars with masses smaller than the original ones. Figure 110 of Leitherer et al. (1999), figure 3 of Courteau et al. (2014), or equation 14 of Behroozi et al. (2013) show that on timescales of gigayears at most $\sim$50% of the mass is lost due to this effect. In summary, the effects of mass loss or accretion will typically yield a factor two increase or decrease in mass. Considering the effects discussed above and the statistical uncertainties on the observed data, the agreement between observations and the Illustris results is remarkably good.

2.8 Discussion

The DTD used in this work is functionally identical to the one of Rodney et al. (2014). Therefore it is possible to compare the value of the prompt fraction, f_p, from our fit to that of Rodney et al. (2014). In Rodney et al. (2014) the transition from a constant to τ^{-1} DTD is fixed at 0.5 Gyr. Following the prescription of equation 2.12, making it explicit that we fix the transition to be 0.5 Gyr with a subscript of 0.5, we arrive at a prompt fraction of $f_{p,0.5} = 0.11^{+0.10}_{-0.06}$ which is in slight tension with the result of $f_p = 0.53^{\pm 0.09\,\pm 0.10}_{\text{stat}\quad\text{sys}}$ where Rodney et al. (2014) utilise their full data set, but is in good agreement with the result of $f_p = 0.21^{\pm 0.34\,\pm 0.49}_{\text{stat}\quad\text{sys}}$ where only the CANDELS+CLASH sample of Ia supernovae was used. If we do not fix the transition to happen at 0.5 Gyr, and instead use the maximum likelihood fit value of $t_1 = 964^{+631}_{-273}$ Myr we find a prompt fraction of $f_p = 0.15^{+0.11}_{-0.09}$. This transition time is significantly larger than the fixed value of 0.5 Gyr of Rodney et al. (2014) but considering the uncertainties there is only slight tension.

From figure 2.1 it is apparent that the difference in predicted Ia supernova rate between the A+B model and the models developed in this work increase with sSFR. The fit suggests that the biggest shortcoming of the A+B model is that it diverges towards increasingly larger values of supernova rate with sSFR, where the models that instead plateau at these large sSFR values in our analysis perform better. This suggests that the A+B model and the assumed DTD of Rodney et al. (2014) are in tension. The high sSFR regime will become increasingly important as future surveys push observations to higher redshifts. See, e.g., figure 4 of Behroozi et al. (2013) showing that galaxies at high redshift are predominantly high sSFR galaxies with an sSFR in excess of $\log \mathrm{sSFR} \gtrsim -10$. A significant part of these galaxies will have sSFR values above $\log \mathrm{sSFR} > -9$. It is difficult to determine the validity of the models of this work in this regime as there are only few constraints from observations at $\log \mathrm{sSFR} > -9$. The reliability of the predicted sSNR in this regime will therefore be strongly dependent on the validity of the underlying assumed model, in this case specifically the DTD assumed in equation 2.4. Conversely, observations at high sSFR will constrain the DTD in this regime.

The test results quoted in table 2.1 corroborate the points made above, with an important additional point being that although the quoted uncertainties for the parameters of the models developed in this work are only estimates, these uncertainty estimates have no influence on the test results as the tests solely depend on the goodness-of-fit of the maximum likelihood parameters. Based on the above results and discussion we recommend that either the piecewise model or the smooth logarithm parametrisation developed in this work is used when predicting type Ia supernova rates.

Acknowledgements

The authors would like to thank Teddy Frederiksen for input and Patrick Kelly, Martin Sparre, and Tamara Davis for useful input and discussions. PA would like to thank Martin Sparre, Mathew Smith, Mark Sullivan, and Yan Gao for providing access to data. JH was supported by a VILLUM FONDEN Investigator grant (project number 16599).

Chapter 3

Cosmology with Peculiar Velocities: Observational Effects

This chapter contains the paper "Cosmology with peculiar velocities: Observational effects" by Andersen, P., Davis, T., and Howlett, C., 2016, MNRAS, doi: 10.1093/mnras/stw2252

3.1 Abstract

In this paper we investigate how observational effects could possibly bias cosmological inferences from peculiar velocity measurements. Specifically, we look at how bulk flow measurements are compared with theoretical predictions. Usually bulk flow calculations try to approximate the flow that would occur in a sphere around the observer. Using the Horizon Run 2 simulation we show that the traditional methods for bulk flow estimation can overestimate the magnitude of the bulk flow for two reasons: when the survey geometry is not spherical (the data do not cover the whole sky), and when the observations undersample the velocity distributions. Our results may explain why several bulk flow measurements found bulk flow velocities that *seem* larger than those expected in standard ΛCDM cosmologies. We recommend a different approach when comparing bulk flows to cosmological models, in which the theoretical prediction for each bulk flow measurement is calculated specifically for the geometry and sampling rate of that survey. This means that bulk flow values will not be comparable between surveys, but instead they are comparable with cosmological models, which is the more important measure.

3.2 Introduction

The term bulk flow in the context of cosmology refers to the average motion of matter in a particular region of space relative to the dipole subtracted cosmic microwave background (CMB) rest frame. One reason why bulk flows are interesting to cosmologists is that by measuring them we can learn more about the composition of the universe, the laws of gravity, and whether our current cosmological model is a good representation of the actual underlying dynamics.

A bulk flow is induced by density fluctuations, and thus the bulk motion we observe should match what we expect from the density distribution. The density distribution is in turn determined by cosmological parameters such as the strength of clustering, through σ_8, and the matter density, $\Omega_{\rm M}$. The magnitude of bulk flows can be predicted from theory given a model and set of cosmological parameters (e.g. σ_8 and $\Omega_{\rm M}$), some initial conditions (such as a fluctuation amplitude at the end of inflation), and a law of gravity (such as general relativity). If the observed bulk flow was to deviate from that predicted by theory, that would indicate that one or more of the given inputs is incorrect.

Currently tension exists in measurements of the bulk flow, with some measurements in apparent agreement with that predicted by ΛCDM (Colin et al., 2011; Dai et al., 2011; Nusser and Davis, 2011; Osborne et al., 2011; Turnbull et al., 2012; Lavaux et al., 2013; Ma and Scott, 2013; Feix et al., 2014; Ma and Pan, 2014; Planck Collaboration, 2014; Hong et al., 2014; Carrick et al., 2015) while others are not (Kashlinsky et al., 2008; Watkins et al., 2009; Feldman et al., 2010; Abate and Feldman, 2012; Watkins and Feldman, 2015). Relieving this tension is important if we are to gain physical insight into the nature of dark energy and dark matter.

The field of using large scale bulk flows to constrain cosmology has historically been limited by systematics due to the limited quality and quantity of the data available. Modern datasets now include peculiar velocity measurements of thousands of galaxies with moderate precision and hundreds of type Ia supernovae (SNe) with excellent precision. These have inspired a new generation of bulk flow studies. As these new datasets become increasingly abundant and precise, it is prudent to investigate the observational effects that may bias a bulk flow measured from one of these datasets.

One such effect is undersampling of the surveyed volume. Undersampling is especially relevant for estimates utilising a small number of distance indicators, like many recent estimates of the bulk flow done with observations of type Ia SNe (Haugbolle et al., 2007; Jha et al., 2007; Colin et al., 2011; Dai et al., 2011; Weyant et al., 2011; Turnbull et al., 2012). Attempts at addressing sampling issues have been proposed, see e.g. Watkins et al. (2009), Li et al. (2012) or Weyant et al. (2011). Another such effect is the geometry of a survey – namely whether the survey covers the whole sky or a narrow cone. Methods such as the minimum variance method proposed by Watkins et al. (2009) attempt to weight arbitrarily shaped survey geometries so that the bulk flow they calculate approximates what would have been measured if the distribution of data was spherical. Other effects, besides observational, might also play an important role. See e.g. Huterer et al. (2015) where the effects of velocity correlations between supernova magnitudes are included in the data covariance matrix, and are found to have a significant impact on the constraints from a derived bulk flow estimate.

The bias that might arise from estimating the bulk flow magnitude with a small number of peculiar velocities, effectively undersampling the surveyed volume, and with a non-spherical dis-

tribution of measurements, is the focus of this paper. We utilise data from the Horizon Run 2 (HR2; Kim et al., 2011) simulation to investigate how strong a bias undersampling introduces for various survey volumes, from spherically symmetric surveys, to hemispherical and narrow cone surveys. We focus on the Maximum Likelihood (ML) estimator of the bulk flow, as it is computationally cheap to perform, easy to interpret and used widely in the literature. Additionally, for a limited test case, we investigate how successful the Minimum Variance (MV) (Watkins et al., 2009) estimator is at alleviating the bias that comes from undersampling. The ML and MV estimators are described in Appendix A, where we take the opportunity to clarify some typographic errors and undefined terms in the original papers that can lead to confusion.

In section 3.3 we introduce the HR2 simulation. Then in section 3.4 we summarise the theoretical footing of large scale bulk flows, and provide an expansion beyond the usual spherical assumptions so that the theory is also valid for non-spherical geometries. The theoretical estimate is established as the benchmark against which we test the effects of undersampling. Then in section 3.5 we analyse the effects of undersampling on the Maximum Likelihood estimator, for a spherical, hemispherical and narrow cone geometry. Finally in section 3.6 we discuss our findings and the implications for future work using large scale bulk flows in cosmology.

Throughout this paper when we refer to the theoretically most likely bulk flow magnitude it will be denoted the *most probable* bulk flow magnitude, V_p, to avoid confusion with bulk flows from the Maximum Likelihood estimator.

3.3 Simulation: Horizon Run 2

Throughout this paper we use the Horizon Run 2 (HR2) cosmological simulation (Kim et al., 2011) to investigate how observational effects, in particular non-spherical survey geometries and undersampling, can influence bulk flow measurements in a ΛCDM universe. We choose this simulation for the following reason: the bulk motions of galaxies are primarily sensitive to large scale density perturbations, meaning that the bulk flow measured in apparently distinct patches drawn from a single simulation can remain significantly correlated. The HR2 simulation, containing 216 billion particles spanning a $(7.2h^{-1}\mathrm{Gpc})^3$ volume, is large enough that we can be confident our bulk flow measurements are effectively independent. The above simulation parameters result in a mass resolution of $1.25 \times 10^{11} h^{-1}\mathrm{M}_{\odot}$, which allows us to recover galaxy-size halos with a mean particle separation of $1.2h^{-1}\,\mathrm{Mpc}$. The power spectrum, correlation function, mass function and basic halo properties match those predicted by WMAP5 ΛCDM (Komatsu et al., 2009) and linear theory to percent level accuracy.

To generate our measurements we first draw spherical subsamples of radius $1h^{-1}\,\mathrm{Gpc}$ from the full HR2 dataset. The origin of each subset is chosen randomly, so that some will be chosen in higher than average density regions and some in lower than average density regions, incorporating the effects of cosmic variance. Knowledge of our local galactic surroundings could have been

folded into the selection of origins, so that the subsets chosen would more closely represent the local environment that we find ourselves in. We have not done this, which means that the results of this work are the zero-knowledge results with no assumptions made about our position in the cosmological density field. In essence, we are comparing our one measurement of the bulk flow of our local universe to the distribution of bulk flows that ΛCDM would predict. It would also be enlightening to investigate whether there are any aspects of our local universe that would bias such a measurement, as Wojtak et al. (2015) did for supernova cosmology. However, that is beyond the scope of this paper.

The HR2 subsets consist of approximately $3.1{\cdot}10^6$ dark matter haloes, each with six dimensional phase space information. Unfortunately a mock galaxy survey that fills the entire volume of the simulation does not exist, so in our analysis we assume that each DM halo corresponds to one galaxy. The smallest of the DM haloes are of a mass comparable to that of a galaxy, but the largest DM haloes of the HR2 simulation have a mass that would be equivalent to hundreds of galaxies. Effectively we are grouping galaxies in massive clusters into just one datapoint with the same probability of being subsampled as any other galaxy.

Fortunately, a limited number of mock SDSS-III (Eisenstein et al., 2011) galaxy catalogues have been produced for the HR2 simulation, which allow us to test how this assumption may affect our results. In Appendix B we perform an analysis of the bulk flow magnitude distribution of galaxies from one such mock catalogue, and compare the distributions derived from the DM halo velocities. Our analysis shows that the distributions are similar, and, as such, treating each halo as an individual galaxy has minimal effect on our results.

To look at the effect of undersampling and non-spherical geometries, we wish to compare the actual bulk flow magnitude of a given number of galaxies within some volume, to the magnitude recovered using the ML and MV estimators. Although a real survey only has peculiar velocity information along the line-of-sight direction, both of these estimators attempt to reconstruct the 3D distribution of velocities and estimate the bulk flow. In this sense a fair comparison is then between the output of these estimators and the most probable bulk flow measured using the full 3D velocity vector for each galaxy. The method we use to determine the most probable bulk flow magnitude as well as the upper and lower 1-σ limit for a particular subsample of the simulation is the following:

1. Randomly place a geometry in the simulation.
2. Of total N galaxies within the geometry, randomly draw n.
3. Derive the actual bulk flow vector of the n galaxies, using the 3D velocity vector for each object.
4. Store the magnitude of the bulk flow vector.
5. Repeat the above process until the resulting distribution has converged.

Analogous to the method above we can determine the most probable bulk flow magnitude and 1-σ upper and lower bounds for a specific bulk flow estimator, e.g. the ML estimator applied in section 3.5:

1. Randomly place a geometry in the simulation.
2. Of total N galaxies within the geometry, randomly draw n.
3. For the n galaxies compute the line-of-sight velocities.
4. Apply the ML estimator to the line-of-sight velocities and derive the ML bulk flow vector.
5. Store the magnitude of the ML bulk flow vector.
6. Repeat the above process until the resulting distribution has converged.

The uncertainty associated with each peculiar velocity measurement is calculated as in Appendix A of Davis et al. (2011), the implications of this are discussed in Appendix C. When determining upper and lower 1-σ bounds we apply an equal likelihood algorithm, so that the 1-σ limits are the equal likelihood bounds that encapsulate 68.27% of the normalised distirbution.

3.4 Linear Theory

Under the assumption of the cosmological principle, that the universe is statistically isotropic and homogeneous, and assuming Gaussian density fluctuations, the velocity field at any given location can be treated as Gaussian random variate with zero mean and variance given by the velocity power spectrum $P_{vv}(k)$. Hence the bulk flow vector measured within some volume can also be described as a Gaussian random variate with zero mean and variance

$$\sigma_V^2(\boldsymbol{r}) = \int \frac{\mathrm{d}^3k}{(2\pi)^3} P_{vv}(k) |\widetilde{W}(\boldsymbol{k};\boldsymbol{r})|^2. \tag{3.1}$$

Assuming isotropy, this becomes

$$\begin{aligned} \sigma_V^2(\boldsymbol{r}) &= \frac{1}{2\pi^2} \int_{k=0}^{\infty} \mathrm{d}k\, k^2 P_{vv}(k) |\widetilde{W}(k;\boldsymbol{r})|^2, \\ \implies \sigma_V^2(R) &= \frac{H_0^2 f^2}{2\pi^2} \int_{k=0}^{\infty} \mathrm{d}k P(k) \widetilde{W}(k;R)^2, \end{aligned} \tag{3.2}$$

where the Hubble constant, H_0, growth rate, f, and velocity and matter power spectra $P_{vv}(k)$ and $P(k)$ define a particular cosmology. The second equality of Eq. 3.2, which is commonly associated with the RMS velocity expected for a bulk flow vector (Coles and Lucchin, 2013) follows from the assumption of a spherically symmetric window function and the linear approximation that $P_{vv} = H_0^2 f^2 k^{-2} P_{\theta\theta}(k) \approx H_0^2 f^2 k^{-2} P(k)$, where $P_{\theta\theta}$ is the power spectrum of the velocity divergence field (See Chapter 18 of Coles and Lucchin (2013) for a review of the relationship between the density, velocity divergence and velocity fields, and Jennings (2012) for measurements of $P_{\theta\theta}$ from simulations). As can be seen in Fig. 1, $P_{\theta\theta}(k) = P(k)$ is typically a good assumption on the

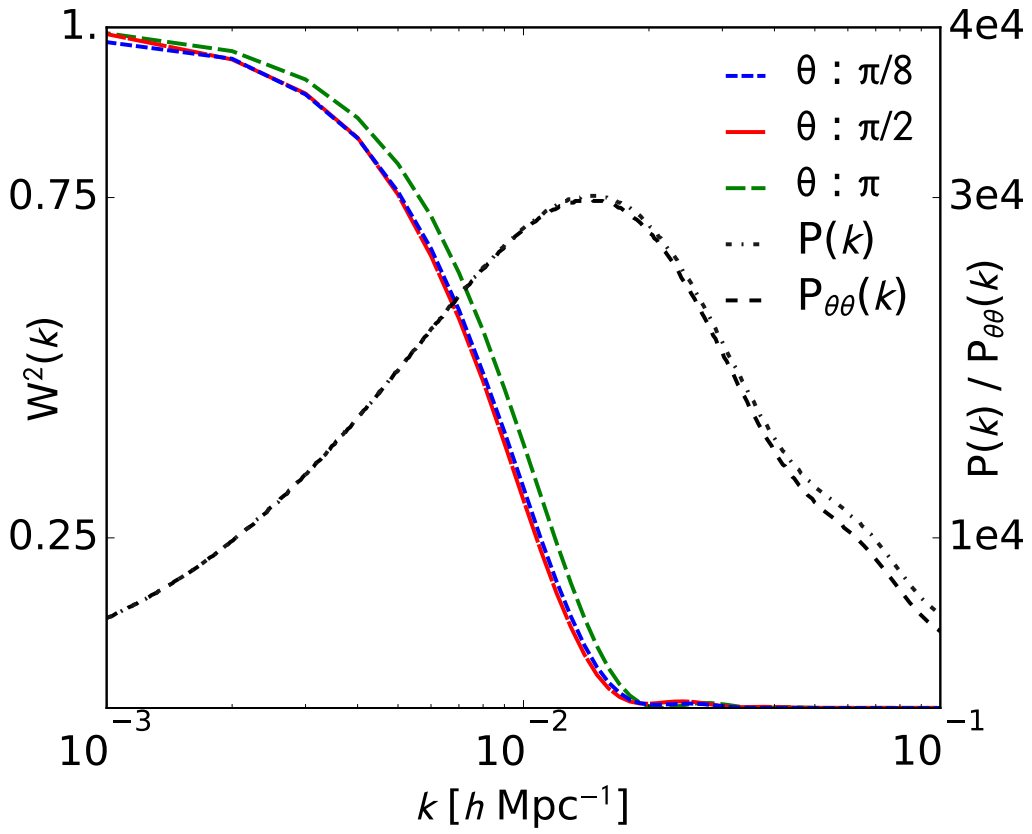

Figure 3.1: Window functions for the geometries used in this paper plotted along with the matter-matter and velocity divergence power spectra from COPTER. $P(k)$ is the matter power spectrum, and $P_{\theta\theta}(k)$ the velocity divergence power spectrum. The geometries used are equal volume spherical cones with opening angles θ, ranging from fully spherical $\theta = \pi$ to a very narrow cone with $\theta = \pi/8$

large scales probed by bulk flow measurements.

In Eq. 3.2 $\widetilde{W}(k;\boldsymbol{r})$ is the Fourier transform of the window function, $W(\boldsymbol{r})$, for the geometry of the specific survey making that bulk flow measurement. The window function is a function of both k and the volume in which the bulk flow is being measured. It measures how sensitive we are to measuring the statistical fluctuations at a particular scale. If the window function is large for a particular k it means that we are highly sensitive to measuring fluctuations at the scale k represents. The window function will be dependent on the geometry of the measurements taken to derive the bulk flow, and is therefore unique for each particular survey. For a fully spherical geometry of radius R the window function takes the form

$$\widetilde{W}(k;R) = \frac{3(\sin kR - kR\cos kR)}{(kR)^3}. \tag{3.3}$$

How strongly the window function of a particular survey will deviate from this spherical case will be determined by the geometry of the survey in question. Example window functions for conical geometries with a variety of opening angles are shown in Fig. 3.1. How these were calculated is

detailed in section 3.4.1.

To calculate all the theoretical values of σ_V in this paper we use a velocity divergence power spectrum, generated with the implementation of Renormalised Perturbation Theory (Crocce and Scoccimarro, 2006) in the COPTER code (Carlson et al., 2009). A linear CAMB[1] (Lewis et al., 2000; Howlett et al., 2012) matter transfer function with the same cosmological parameters as HR2 and WMAP5 was used as input. From this COPTER produces both a non-linear matter power spectrum as well as a non-linear velocity divergence power spectrum. We found that the difference between using the COPTER velocity divergence power spectrum, the non-linear matter power spectrum, or the linear power spectrum was negligible, except for very narrow or small geometries where effects at $k \gtrsim 0.05$ become important. In Fig. 3.1 we can see that for the geometries used in our analysis the differences when using the three power spectra are small as the spectra only differ in the regime where the window function vanishes. Nonetheless, throughout this paper we use the COPTER velocity divergence power spectrum as that is most appropriate when working with bulk flows.

To calculate the theoretical most probable bulk flow magnitude $V_p(R)$ we use the fact that the peculiar velocity distribution is Maxwellian (Li et al., 2012) with RMS velocity σ_V, which gives us a probability distribution for the bulk flow amplitude of the form (Coles and Lucchin, 2013)

$$p(V)\mathrm{d}V = \sqrt{\frac{2}{\pi}}\left(\frac{3}{\sigma_V^2}\right)^{3/2} V^2 \exp\left(-\frac{3V^2}{2\sigma_V^2}\right)\mathrm{d}V. \tag{3.4}$$

For this distribution the maximum probability value is then given by the relation

$$V_p(R) = \sqrt{2/3}\,\sigma_V(R). \tag{3.5}$$

When referring to the theoretical most probable bulk flow magnitude throughout this paper, it is this value based on a Maxwellian distribution of velocities that we are referencing. We confirmed that the velocities of halos in the HR2 simulation do indeed follow a Maxwellian distribution.

It is important to note that while the most probable bulk flow magnitude is a discrete value, it is still a value from a distribution with a variance. Optimally the theoretical distribution should be compared to an observed distribution of bulk flow magnitudes, but this is not practical in most situations. The best we can do is to compare our measured bulk flow magnitude with the most probable bulk flow magnitude from theory, but importantly remember to account for the variance on our theoretical prediction in our statistics.

3.4.1 Non-Spherical Geometries

As well as investigating the effects of undersampling on a spherical geometry, we wish to additionally develop a theoretical estimate for non-spherical geometries, that is we wish to break the

[1] http://camb.info/readme.html

assumption of spherical symmetry used to derive Eq. 3.3. For uniformly distributed surveys the window function takes the form

$$\widetilde{W}(\boldsymbol{k};\mathbf{r}) = \frac{1}{V}\int_V \exp\left(i\mathbf{k}\cdot\mathbf{r}\right)\mathrm{d}\mathbf{r}, \tag{3.6}$$

where $\exp\left(i\mathbf{k}\cdot\mathbf{r}\right)$ can be expanded to (Coles and Lucchin, 2013),

$$\exp\left(i\mathbf{k}\cdot\mathbf{r}\right) = \sum_{l,m} j_l(kr)i^l(2l+1)\mathcal{P}_l^{|m|}(\cos\theta)\exp\left(im\phi\right), \tag{3.7}$$

where $\mathcal{P}_l^{|m|}$ are the Associated Legendre Polynomials. The integral of Eq. 3.6 then becomes

$$\begin{aligned}\int_V &\exp\left(i\mathbf{k}\cdot\mathbf{r}\right)\mathrm{d}\mathbf{r} \\ &= \sum_{l,m} i^l(2l+1)\int_0^{\phi_{max}}\exp\left(im\phi\right)\mathrm{d}\phi \\ &\int_0^{\theta_{max}}\mathcal{P}_l^{|m|}(\cos\theta)\sin\theta\mathrm{d}\theta\int_0^R j_l(kr)r^2\mathrm{d}r\end{aligned} \tag{3.8}$$

which for the spherical case where $(\theta_{max},\phi_{max}) = (\pi, 2\pi)$ reduces to Eq. 3.3. For a spherical cone geometry, with radius related to volume and opening angle by

$$r = \left(\frac{3V}{2\pi(1-\cos\theta)}\right)^{1/3}, \tag{3.9}$$

we can set $\phi_{max} = 2\pi$ but let θ_{max} vary in the interval $(0;\pi]$. Regardless of the values of l, all terms of m vanish except for the $m = 0$ term. Therefore for non-spherical geometries we have to sum over l to infinity. Although this approach is theoretically correct, in practice we would sum over l only until the function value had converged to within computational accuracy. This is however very impractical since the complexity of the terms increase rapidly with l making it difficult to include terms above $l \approx 20$. Unfortunately, we find that for our geometries that are very non-spherical only using terms $l \leq 20$ is not sufficient to guarantee convergence. Hence this approach is still only practical for geometries close to a sphere.

Another approach to solving the window function for a given k is to reformulate the volume integral in Cartesian coordinates

$$\widetilde{W}(k;\mathbf{r}) = \frac{1}{V}\int_0^X\int_0^Y\int_0^Z w(x,y,z)e^{i(kx+ky+kz)}\mathrm{d}x\mathrm{d}y\mathrm{d}z. \tag{3.10}$$

The triple integral is over a cube that is at least large enough to contain the volume V from Eq. 3.6. The $w(x,y,z)$ function is introduced, defined as being one inside the volume and zero otherwise, which makes sure the volume integrated over is conserved. The conversion to Cartesian coordinates makes it simpler to solve the integral numerically. It should be noted that even though we only consider rotationally symmetric windows with constant number density in this study, the

above equation can be extended to include surveys of arbitrary geometry and non-constant number density, simply by choosing a suitable function $w(x, y, z)$.

Based on Eq. 3.10 we developed two pieces of code to solve the problem numerically, one calculating the integral using MCMC methods and the other applying a trapezoidal volume integral.[2] The independence of the two codes is used to confirm the validity of the results; the outputs from the two codes are consistently within 3% percent of one another.

To see how this theoretical prediction compares with the actual underlying bulk flow of the HR2 simulation, we plot the most probable bulk flow magnitude as well as the upper and lower 1-σ limits as a function of geometry in Fig. 3.2. The geometry in this case is a spherical cone where the opening angle θ is varied. It is worth noting that the volume of the geometry is kept constant as the opening angle θ is varied. This is achieved by varying the radial extent of the geometry along with θ according to Eq. 3.9. Keeping the volume constant helps keep the simulation and theoretical results almost constant as θ is varied. For all opening angles we see that our theoretical value matches that measured from the simulations extremely well.

3.5 Geometry and Sampling Effects

In this section we present how non-spherical geometries and undersampling of the cosmological volume can impact the results of the ML and MV estimators. We use the theoretically predicted most probable bulk flow magnitude as a benchmark; the closer the estimator comes to replicating the theoretical distribution the better.

We first investigate the scenario where we use a fixed number of objects ($n = 500$) and compare both the performance of the ML and MV estimator. The results can be seen in Fig. 3.2. Both the ML and MV estimator have a bias towards measuring larger bulk flow magnitudes on average than the actual underlying bulk flows. As the survey geometry becomes narrower, however, this bias increases, with the most narrow geometry having the strongest bias. The behaviour of the ML and MV estimators is very similar.

In the narrow cone regime, both the ML and MV estimators predict significantly larger most probable bulk flows than would be expected from theory. Hence, incorrectly accounting for non-spherical geometries in the ML and MV estimators could potentially lead one to conclude they had measured a larger bulk flow than would be expected in a ΛCDM universe.

Next we investigate how the sampling rate can create biases in the most probable bulk flow calculated using the ML and MV estimates for a fixed geometry. For the values $n \in [50, 500, 1000, 2000, 4000]$ and opening angles $\theta \in [\pi/8, \pi/2, \pi]$, corresponding to a narrow spherical cone, a hemisphere,

[2] For details and link to the source code see https://github.com/per-andersen/MV-MLE-BulkFlow

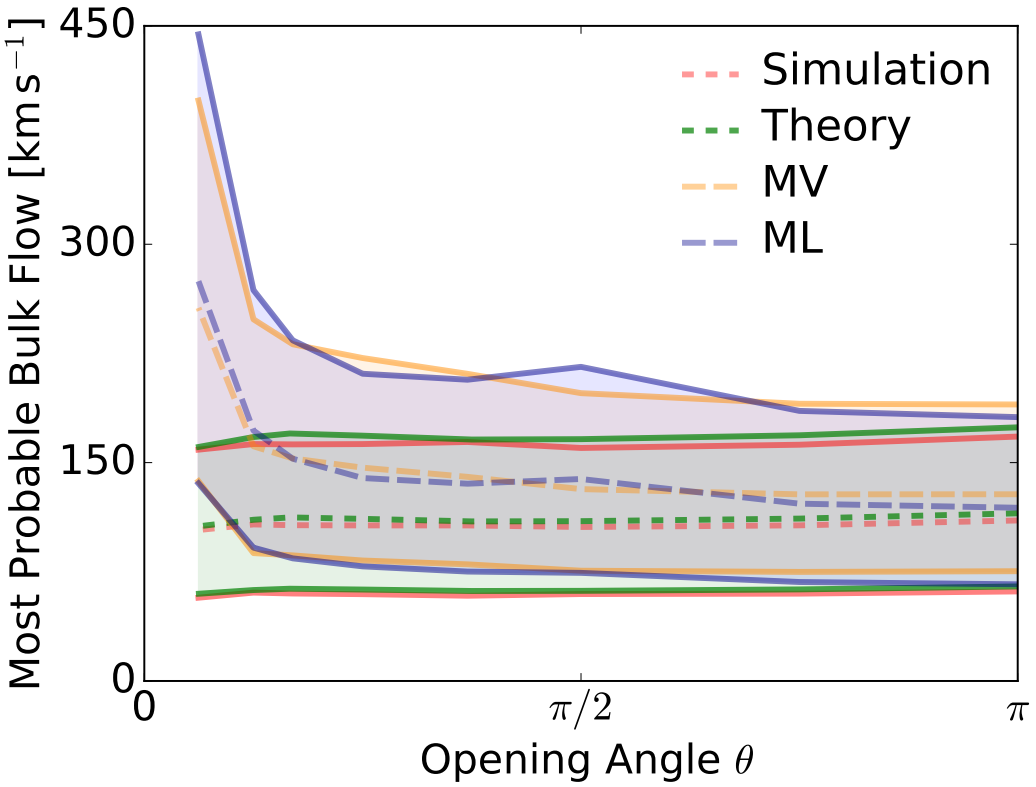

Figure 3.2: The most probable measured bulk flow magnitude as a function of opening angle for a spherical cone geometry. The tested geometries vary in opening angle from the fully spherical situation where $\theta = \pi$, over a hemisphere to the most narrow geometry tested being $\theta = \pi/16$. The distributions from the simulation, theory, MV estimator, and ML estimator are shown with the dashed line being the most probable bulk flow magnitude and the colored band showing the upper and lower 1-σ limits. For both the ML and MV estimators the sampling was fixed at $n = 500$. For the MV estimator the ideal radius R_I was set to 50 Mpc h^{-1}.

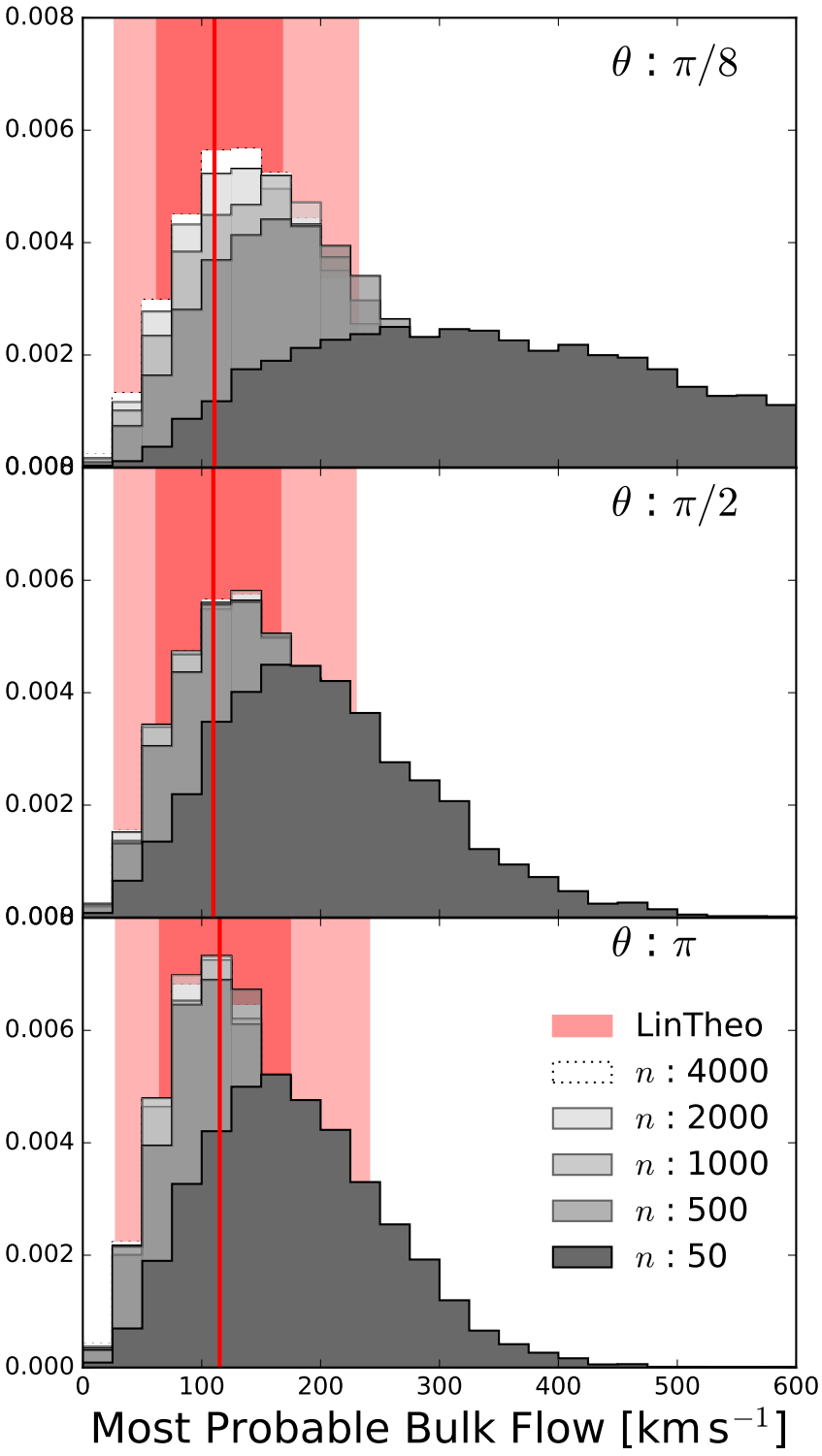

Figure 3.3: Distributions of ML bulk flow magnitudes for various sampling rates, n. The top/middle/bottom distributions correspond to a geometry with opening angle $\frac{\pi}{8}/\frac{\pi}{2}/\pi$. The volume is kept constant as opening angle is varied, resulting in a radius of 631/267/210 Mpc h^{-1}.

and a full sphere, we apply the ML estimator as described in section 3.3. The results can be seen in Fig. 3.3. There are two noteworthy trends from this plot. The first is that for all geometries the estimated most probable value is shifted to be 1-σ away from the actual most probable value when the sampling is less than $n \lesssim 500$. The second is that this effect is stronger for narrow geometries, in our case the geometry with opening angle $\theta = \pi/8$ is much more adversely affected by undersampling than the hemispherical or spherical case. What this means in practice is that estimates of the bulk flow magnitude that utilise a small number of peculiar velocities are likely to be biased by undersampling effects in such a way that we would measure on average a larger bulk flow magnitude than the actual underlying bulk flow being probed. Of particular interest is the fact that this remains true even for spherical geometries if the number of objects is small.

The most probable bulk flow velocities for the distributions in Fig. 3.3, as well as a few additional configurations of sampling rate and opening angles, are listed in Table 3.1. The absolute differences between the most probable bulk flow values derived from simulation and theory are also listed. This absolute difference is an indicator of how strong a bias we might expect in the distribution of bulk flows derived for a particular sampling rate and survey geometry. A small absolute difference between most probable bulk flow velocities from simulation and theory indicates that the sampling rate is sufficient, and that minimal bias is to be expected for that particular survey geometry. In using Table 3.1 it is important to note that not only the most probable bulk flow velocity, V_p, is shifted towards larger values. Rather, the entire distribution of bulk flow velocities is shifted, including the one and two sigma limits. Looking at, e.g., line seven of Table 3.1 where $n = 50$ and $\theta = 0.125\,\pi$ we see that even though the theory predicts something close to $\sim$100 km s^{-1} a measured bulk flow value of $\sim$500 km s^{-1} is still within the one sigma confidence limits, and hence is still well within the expectations of a ΛCDM cosmology.

The cause for the bias from poor sampling is the increased variance of the bulk flow velocity components; in Fig. 3.4 the x-components of the bulk flow velocities from the top panel of Fig. 3.3 are plotted for the various sampling rates. When sampling decreases variance increases, which in turn causes the most probable bulk flow value to shift according to Eq. 3.5. Note that σ_V in Eq. 3.5 denotes the variance of the bulk flow *vector*, which is equal to the RMS because the distribution of bulk flow vectors is Gaussian. The variance in any one Cartesian component of the bulk flow vector is then $\sigma_V/\sqrt{3}$. For the bulk flow *magnitude* σ_V refers only to the RMS, due to the relationship between Maxwellian and Gaussian distributions. The variance of the bulk flow magnitude is then given by[3] $\sigma^2 = \sigma_{\rm V}^2(1 - \frac{8}{3\pi})$.

Another way to illustrate this effect is to imagine a large volume where the galaxies within obey the cosmological principle such that if you sum over the velocities of all N galaxies you will derive a bulk flow magnitude of exactly zero. This will be true even if only the line-of-sight

[3]To derive this use $p(V)dV$ from equation 3.4 in the definition of variance $\sigma^2 \equiv \int_0^\infty p(V)(v-\bar{v})^2 dV$, where the standard integral $\int_0^\infty x^n e^{-bx^2} dx = \frac{(2k-1)!!}{2^{k+1}b^k}\sqrt{\frac{\pi}{b}}$ with $n = 2k$ and $b > 0$ comes in handy; note $(2k-1)!! \equiv \Pi_{i=1}^{k}(2i-1) = \frac{(2k)!}{2^k k!}$.

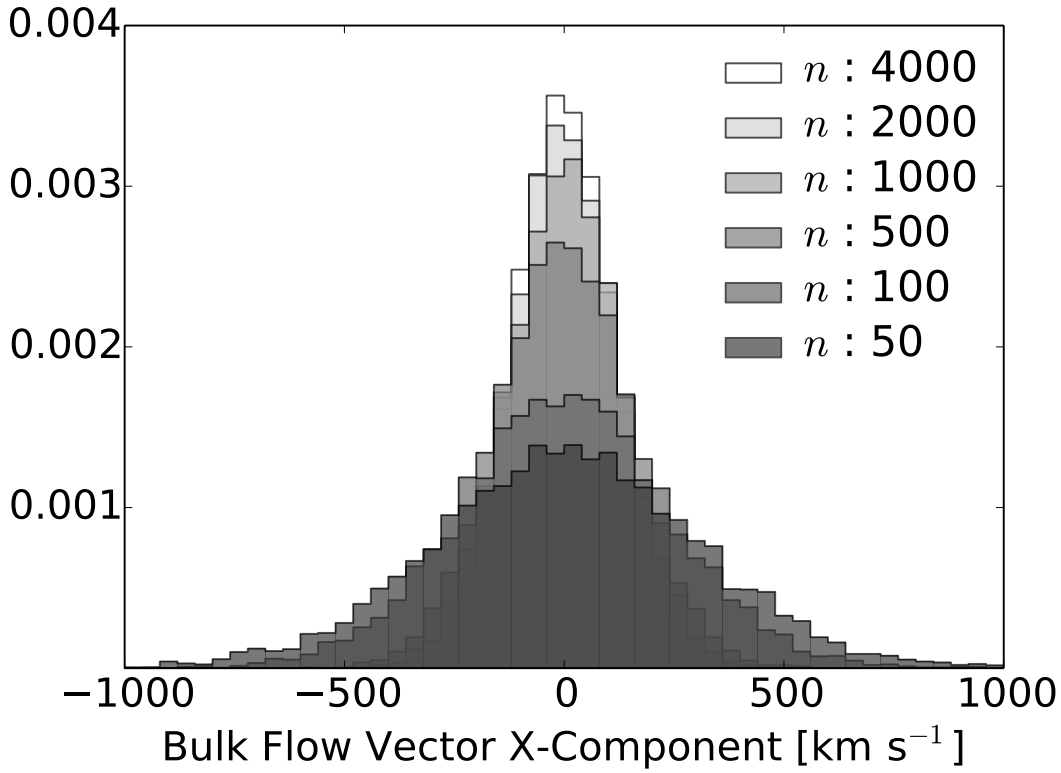

Figure 3.4: The distribution of the x-components of the bulk flows from the top panel of Fig. 3.3 where the opening angle is $\theta = \pi/8$. Poorer sampling leads to a larger variance in the Gaussian-distributed velocity components, which in turn causes the most probable bulk flow to shift to a larger value.

components of the peculiar velocities are observed. If then only $n < N$ peculiar velocities are observed, it is very likely that a non-zero bulk flow magnitude will be measured, and since a magnitude can only ever be positive we are now dealing with some non-zero positive number. We might redraw a new set of n galaxies and derive a different magnitude, but it is still going to be some non-zero positive number. If $n \approx N$ then we are likely to measure a magnitude that is closer to zero than if we only draw $n \ll N$ galaxies. In other words, undersampling *always* increases our RMS velocity and skews the most probable measured magnitude towards larger values.

3.6 Discussion & Conclusion

After reviewing linear theory we showed how it can be expanded to be valid for non-spherical geometries, developing code that numerically calculates the theoretical bulk flow magnitude for any arbitrary survey geometry. To test the validity of the developed code, the derived theoretical bulk flow magnitude was compared to that of a variety of spherical cone geometries in the Horizon Run 2 (HR2) cosmological simulation and found to be within 5% or better agreement for all tested geometries.

	θ	V_p km s^{-1}	68% Limits km s^{-1}	$\lvert V_p - V_{p,\mathrm{theory}} \rvert$ km s^{-1}	Sample Density $(h^{-1}\mathrm{Mpc})^{-3}$
n : 8000	0.125 π	$132\ ^{+73}_{-61}$	71 - 205	26	200×10^{-6}
n : 4000	0.125 π	$136\ ^{+75}_{-63}$	73 - 210	29	100×10^{-6}
n : 2000	0.125 π	$142\ ^{+79}_{-66}$	75 - 221	35	50×10^{-6}
n : 1000	0.125 π	$153\ ^{+86}_{-72}$	80 - 238	46	25×10^{-6}
n : 500	0.125 π	$173\ ^{+97}_{-81}$	92 - 269	66	12×10^{-6}
n : 100	0.125 π	$257\ ^{+143}_{-119}$	137 - 399	150	2×10^{-6}
n : 50	0.125 π	$326\ ^{+203}_{-166}$	160 - 528	219	1×10^{-6}
n : 8000	0.5 π	$131\ ^{+74}_{-62}$	68 - 205	21	200×10^{-6}
n : 4000	0.5 π	$131\ ^{+74}_{-61}$	69 - 204	22	100×10^{-6}
n : 2000	0.5 π	$132\ ^{+75}_{-63}$	69 - 207	22	50×10^{-6}
n : 1000	0.5 π	$133\ ^{+76}_{-63}$	69 - 208	23	25×10^{-6}
n : 500	0.5 π	$136\ ^{+77}_{-64}$	72 - 213	27	12×10^{-6}
n : 100	0.5 π	$158\ ^{+89}_{-74}$	84 - 247	49	2×10^{-6}
n : 50	0.5 π	$180\ ^{+96}_{-81}$	99 - 275	70	1×10^{-6}
n : 8000	1.0 π	$110\ ^{+58}_{-49}$	61 - 168	3	200×10^{-6}
n : 4000	1.0 π	$110\ ^{+58}_{-49}$	61 - 167	3	100×10^{-6}
n : 2000	1.0 π	$111\ ^{+59}_{-49}$	61 - 169	2	50×10^{-6}
n : 1000	1.0 π	$113\ ^{+59}_{-50}$	62 - 171	0	25×10^{-6}
n : 500	1.0 π	$116\ ^{+61}_{-51}$	64 - 176	3	12×10^{-6}
n : 100	1.0 π	$138\ ^{+72}_{-61}$	77 - 210	25	2×10^{-6}
n : 50	1.0 π	$159\ ^{+83}_{-70}$	89 - 241	46	1×10^{-6}

Table 3.1: V_p is the most probable bulk flow for the distribution of bulk flows derived from simulation using the ML estimator, for the given survey geometry, defined by the opening angle θ, and sampling rate, given by n, which is the number of peculiar velocities per derived bulk flow estimate. The upper and lower one sigma equal likelihood limits encapsulating 68% of the likelihood are also listed. $\lvert V_p - V_{p,\mathrm{theory}} \rvert$ is the absolute difference between the most probable bulk flow velocity derived from estimate and from linear theory. A small absolute difference indicates that the sampling rate is sufficient for the given geometry, such that the derived distribution matches the actual underlying distribution. In the final column the survey sample density is listed for reference.

However, when simulating more realistic surveys and applying the Maximum Likelihood (ML) estimator we found that undersampling effects severely bias measurements of the bulk flow magnitude when a small number ($n \lesssim 500$) of peculiar velocities are used in the bulk flow estimate. On average, undersampling pushes the measured bulk flow to higher values, with the bias being amplified when narrower survey geometries are used.

For our fixed volume of $40{\cdot}10^6(h^{-1}\mathrm{Mpc})^3$ using 500 SNe corresponds to a sampling density of $\sim 13\,\mathrm{SNe}/10^6(h^{-1}\mathrm{Mpc})^3$. Hence we expect undersampling could affect many recent measurements of the of the bulk flow magnitude utilising type Ia SNe as a distance indicator (i.e, Haugbolle et al. 2007; Jha et al. 2007; Colin et al. 2011; Dai et al. 2011; Weyant et al. 2011; Turnbull et al. 2012; Feindt et al. 2013) where the number of supernovae are well below 300 and the sampling density is also well below $13\ \mathrm{SNe}/10^6(h^{-1}\mathrm{Mpc})^3$.

Without a detailed analysis of each of the previous bulk flow estimates, which is beyond the scope of this paper, it is hard to determine whether or not a particular result is affected by undersampling. However, some examples that might deserve attention include e.g. Feindt et al. (2013) where the SNe are subdivided into four shells, and for the SNe in each shell a bulk flow is estimated. We would expect the bulk flow to converge to the CMB frame as we go to higher redshifts and larger volumes, and yet Feindt et al. (2013) find that in shells of both increasing redshift and increasing volume there is no clear trend in the magnitude of the bulk flow. Instead, the trend they see could potentially be explained by undersampling. Their bins contain varying numbers of supernovae, namely $n = [128, 36, 38, 77]$, in which they find bulk flows of $V_\mathrm{p} = [243, 452, 650, 105]\mathrm{km\,s^{-1}}$. So there is a trend by which the bins with fewer supernovae find larger bulk flows (e.g. compare the middle two bins with the outer two bins).

Similarly, Turnbull et al. (2012) provide two measurements of the ML bulk flow: one with all 245 SNe from the First Amendment compilation, the other with a subset of 136 SNe that excludes the nearby ones (excludes $z < 0.02$). Naive expectations would suggest that the sample focussing on higher redshift SNe should be closer to converging on the CMB and thus have a lower bulk flow, however they find the opposite. The higher-redshift-only sample has a higher bulk flow, but since it has fewer data points than the full sample that would be consistent with our finding that undersampling overestimates the bulk flow.

Both Feindt et al. (2013) and Turnbull et al. (2012) found bulk flows that exceeded the predicted flow based on known density distributions in the nearby universe, so whether the estimates are inflated by undersampling is potentially an interesting question (although neither claimed significant deviation from ΛCDM). While we have selected these two as the most significant examples that could be affected by the sampling biases we discuss in this paper, we note that this trend is pervasive, as no other samples show significant opposing trends. Some show slight reduction in bulk flow with smaller samples, but it is much less significant than the positively correlated examples above (and much smaller than the uncertainties), e.g. in Colin et al. (2011) increasing the sample from 61 to 109 SNe increases the estimated bulk flow from 250 $\mathrm{km\,s^{-1}}$to 260 $\mathrm{km\,s^{-1}}$, an effect of less than 5%.

For bulk flow estimates where the typical number of observed peculiar velocities in a survey is $n \gtrsim 3000$, i.e., most estimates using the Tully-Fisher or Fundamental Plane relation (Nusser and

Davis, 2011; Ma and Pan, 2014; Watkins and Feldman, 2015; Scrimgeour et al., 2016), we found no bias from undersampling. It is however important to note that the analysis of this paper assumes type Ia SNe are used as distance indicators, and therefore the uncertainties in each distance measurement are small (Appendix C). The typically larger uncertainties derived from Tully-Fisher or Fundamental Plane estimates would increase the variance in the individual bulk flow components, which in turn could mean we require larger numbers of objects to avoid biases than is found here.

Effects from uneven sampling have previously been discussed in the literature. One example is Eq. 10 of Li et al. (2012) where a method of dividing the measured peculiar velocities by their selection function is proposed. In Aaronson et al. (1982) and Haugbolle et al. (2007) Monte Carlo simulations of observations are used to better understand systematic effects, including sampling effects. Other works (Weyant et al., 2011; Watkins et al., 2009) develop new estimators such as the Weighted Least Squares (WLS), the Coefficient Unbiased (CU), or the Minimum Variance (MV) estimators, with the MV estimator being the most popular alternative to the ML estimator. The MV estimator is constructed in part to account for sampling bias (with the motivation to be able to compare measurements of bulk flow between surveys); in our work we found that the MV estimator suffered the same bias as the ML estimator, again with the bias increasing for narrower geometries.

A number of recent papers compare a measured bulk flow directly to a ΛCDM prediction based on linear theory and an assumption of spherical symmetry. For example Colin et al. (2011), Dai et al. (2011), and Scrimgeour et al. (2016) plot bulk flow measurements as a function of redshift compared to a generic ΛCDM prediction. Our analysis suggests that such a comparison between bulk flows derived from different surveys, and therefore different survey geometries and sampling rates, is potentially problematic.

In Park et al. (2012) the HR2 simulation was used to show that the size of the large scale structure known as the Sloan Great Wall (SGW) is in agreement with what we statistically expect from ΛCDM cosmology, something that had previously been disputed. Similarly, as early as Aaronson et al. (1982) simulations were being used to compare measured bulk flows to theoretical predictions. Analogous to their arguments, our study highlights the importance of considering the full distribution of bulk flow magnitudes from theory, including sampling effects, rather than focusing on only the most probable bulk flow magnitude. That is, we propose that bulk flows should not be compared to the prediction from linear theory, but with the bulk flow magnitude distribution derived from a cosmological simulation using the method described above, with the actual survey geometry given as input.

Acknowledgements

Parts of this research were conducted by the Australian Research Council Centre of Excellence for All-sky Astrophysics (CAASTRO), through project number CE110001020. The Dark Cosmology Centre was funded by the DNRF.

Chapter 4

Peculiar Velocity Correction for Dark Energy Survey Type Ia Supernovae

This chapter contains the unpublished notes on peculiar velocity correction for the Dark Energy Survey type Ia supernovae by Andersen, P., 2018.

4.1 Abstract

These notes detail first how we currently correct redshifts for peculiar velocities when doing cosmology with the Dark Energy Survey (DES) type Ia supernovae (SNe). Secondly we discuss how we can improve the current prescription by associating the current correction with an uncertainty.

4.2 Introduction

The observed velocity of a galaxy is a sum of the recession velocity which is attributed to the Hubble flow, as well as the peculiar motion caused by a gravitational pull from small and large scale structures. At redshifts of ≥ 0.1 the recession velocity is approximately of order $c\,z \sim 30000$ km s^{-1}where typical peculiar motions are of order 300 km s^{-1}and therefore a sub percent contribution. At lower redshifts peculiar velocities contribute significantly to the observed redshift and in the context of Ia SN cosmology it is therefore crucial to understand the effects that peculiar velocities have on cosmology fitting. If the peculiar velocities of the SNe in the observed sample were distributed isotropically they would add an additional source of scatter in the Hubble diagram at low redshifts. This would in turn not bias the derived cosmological parameters, rather just add to the statistical uncertainty on those parameters. However, if the low redshift SNe are embedded in a large scale flow this will introduce a non trivial systematic shift in the low redshift part of the Hubble diagram which in turn will systematically bias the derived cosmological parameters. Whether this systematic bias from correlated flows is significant depends on the size of the this bulk motion. In table 5 of Scrimgeour et al. (2016) is a summary of recent size estimates of the bulk motion, which range from $\sim$200km s^{-1}to $\sim$1000 km s^{-1}, with a mean value weighted by the uncertainties yielding $\sim$347 km s^{-1}. 347 km s^{-1}corresponds to a redshift bias of $\frac{347\mathrm{km\,s^{-1}}}{c} \approx$

0.0012. Different methods have been proposed to correct for the peculiar motion of galaxies and hence for the systematic bias in the cosmological parameters. One of the first to perform a correction on a one correction per supernova basis was Conley et al. (2011) who applied the method described in Neill et al. (2007) which is based on linear pertubation theory,

$$\mathbf{v} = \frac{\beta}{4\pi} \int^{R_{\max}} \delta(\mathbf{r}') \frac{\mathbf{r}' - \mathbf{r}}{|\mathbf{r}' - \mathbf{r}|} d^3\mathbf{r}' + \mathbf{V}. \tag{4.1}$$

Here $\mathbf{v}$ is the peculiar velocity field at position $\mathbf{r}$ where $\mathbf{V}$ is a dipole term that takes into account flows on scales larger than $R_{\max}$ and β which is a scaling parameter. Conley et al. (2011) then assumed that the uncertainty associated with this correction was 150km s^{-1}for all supernovae in their sample. Later the study in Betoule et al. (2014a) adopted the same methodology as Conley et al. (2011) when correcting observed redshifts for effects of peculiar velocities. More recently Riess et al. (2016a) correct redshifts for peculiar velocities based on the density maps of Scolnic et al. (2014, 2015), and assume a constant uncertainty associated with this correction of 250km s^{-1}. In this work we will investigate the size of this bias specifically in the context of the Dark Energy Survey (DES) and define the method used to correct the SNe in the DES sample for peculiar velocities.

4.3 Current Peculiar Velocity Correction

The peculiar velocity field used for corrections comes from the 2M++ redshift compilation (`http://cosmicflows.iap.fr/download.html`). The data is a three dimensional discrete grid where for each point in the grid we have velocities in the x, y, and z direction. The grid runs from -200 to 200 Mpc/h with a grid spacing of 1.5625 Mpc/h yielding a total of 256^3 grid points. The velocities are in the CMB frame in Galactic Cartesian coordinates, with the best fitting external dipole of $V_{\rm ext} = (89, -131, 17)$ already added (Carrick et al. (2015), Table 3).

When correcting a supernova for the peculiar velocity we start by getting the peculiar velocity from the 2M++ grid nearest to the supernova in question. If the supernova happens to be outside of the 200 Mpc/h large grid a zero velocity is returned, effectively causing a zero-correction. Once the peculiar velocity is known the correction can be applied. The input to the correction function is a redshift in the heliocentric frame, $z_{\rm h}$. Therefore two corrections need to be applied: One that converts from the heliocentric frame to the CMB frame, $z_{\rm CMB}$, and one that applies the peculiar velocity correction in the CMB frame. The corrected redshift can therefore be calculated by

$$z_{\rm cor} = \frac{1 + z_{\rm cmb}}{1 + C_p} - 1, \tag{4.2}$$

where

$$z_{\rm cmb} = (1 + z_{\rm h})(1 + C_h) \tag{4.3}$$

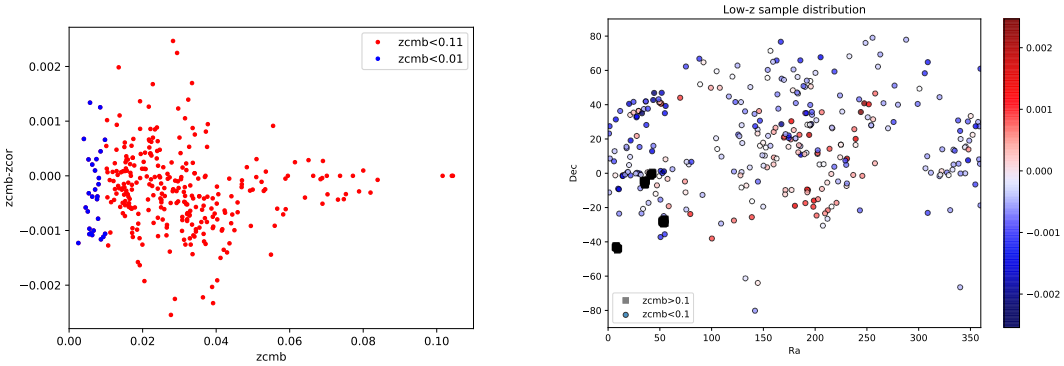

Figure 4.1: Size of the peculiar velocity redshift correction as a function of redshift (left) and position (right). *Left*: The horizontal axis shows the redshift in the CMB frame, z_{CMB}, after correcting the observed redshift for the Earth's motion. The vertical axis is the difference between z_{CMB} and the redshift after correcting for our estimate of the distant galaxy's peculiar velocity, z_{cor}. Thus z_{cor} should be the true cosmological redshift after the peculiar velocities of both the observer (Earth) and emitter (distant galaxy) have been removed. The plot illustrates that for larger redshifts the flow tends towards the CMB dipole, but for smaller redshifts there is some variation due to smaller scale flows. *Right*: Colours indicate the magnitude of the peculiar velocity correction ($z_{\mathrm{CMB}} - z_{\mathrm{cor}}$) applied for supernova positions indicated by the RA and Dec shown on the axes. Squares indicate the positions of our four high-z sample regions (the DES regions).

and

$$C_h = \frac{v_h}{c}\left(\sin b \sin b_h + \cos b \cos b_h \cos\left(l - l_h\right)\right) \tag{4.4}$$

$$C_p = \frac{v_p}{c} \cdot \begin{pmatrix} \cos l \cos b \\ \sin l \cos b \\ \sin l \end{pmatrix} . \tag{4.5}$$

Here C_p is the peculiar velocity correction term and C_h the heliocentric correction term. Additionally z_{cmb} is the CMB frame uncorrected redshift, z_h the heliocentric redshift and, b_h, l_h, and v_h are constants defining the direction of the sun's movement in the CMB frame given by $(b_h, l_h, v_h) = (48.25°, 263.85°, 371\,\mathrm{km\,s^{-1}})$. The above correction is implemented in code in the SpectroSN repository on GitHub (`https://github.com/dessn/SpectroSN/tree/master/data/nearby`).

4.4 Understanding our sample

The peculiar velocity correction is only applied to low-redshift data that has $z < 0.1$ and has a predicted peculiar velocity value in the 2M++ grid. Figure 4.1 shows the magnitude of the peculiar velocity redshift correction both as a function of redshift (left) and position (right).

4.5 Effects of Incompleteness in 2M++ Peculiar Velocity Field

Before describing how we we introduce uncertainties on the correction made in the previous section, we first wish to investigate the effects of data incompleteness, possibly causing some local

structures to be missing in the peculiar velocity field. This could introduce a spurious dipole in the correction, and would systematically apply an incorrect correction. If this is potentially a large effect we need to properly take it into account when correcting redshifts for peculiar velocities. If it is a minor effect we can instead include it in the uncertainty budget for the peculiar velocity correction, which is not entirely correct, but much easier for our cosmology fitter people to work with. Michael Hudson has given us a crude ballpark estimate that this effect is of order 100 $\mathrm{km\,s^{-1}}$. To test the effects of this on cosmological parameter estimation we introduce the factor f which systematically shifts all corrected redshifts with same fraction of the size of the correction. In the code we implement this by shifting z_{cor} to

$$z_{\mathrm{cor}} \to z_{\mathrm{cor}} + f\Delta z \tag{4.6}$$

where $\Delta z \equiv (z_{\mathrm{cmb}} - z_{\mathrm{cor}})$ is the difference between the uncorrected CMB-frame redshift and the peculiar-velocity-corrected CMB-frame redshift. Testing f values in the range $f \in [-1, 1]$ corresponds to testing miscalibrated dipoles of $[-160, 160]\,\mathrm{km\,s^{-1}}$. The parameters Ω_m, w_0 from the $f = 0$ case will then be compared with the $f \in [-1, 1]$ results. The results of this analysis are summarised in table 4.1, and the full corner plots for each fit can be found at the end of these notes. From table 4.1 we see that w_0 is very stable. Ω_m however is shifted on order of 10-15%.[1] That shift is less than the one-sigma uncertainty, so not statistically significant, but nevertheless it is a systematic bias we want to avoid. Given that it is a sub-dominant uncertainty we consider it reasonable to treat it roughly by adding an uncertainty to the diagonal of the covariance matrix (or to the simulations).

f	Ω_m	w_0	Ω_m offset
0	$0.15^{+0.23}_{-0.15}$	$-0.47^{+0.13}_{-0.21}$	-
0.5	$0.17^{+0.23}_{-0.16}$	$-0.47^{+0.13}_{-0.22}$	12%
-0.5	$0.17^{+0.23}_{-0.15}$	$-0.48^{+0.13}_{-0.21}$	12%
1.0	$0.18^{+0.23}_{-0.17}$	$-0.47^{+0.14}_{-0.23}$	17%
-1.0	$0.14^{+0.23}_{-0.14}$	$-0.47^{+0.12}_{-0.21}$	-7%

Table 4.1: The derived Ω_m and w_0 values for various values of f with associated 68% likelihood uncertainties. The value of f dictates the size of the introduced synthetic dipole. The range $f \in [-1, 1]$ corresponds to synthetic dipoles in the range $[-160, 160]\,\mathrm{km\,s^{-1}}$. Therefore when f is zero there is no synthetic dipole, which is used as the benchmark to compare the other derived cosmological parameters against. The sign of f determines the direction of the introduced synthetic dipole.

[1] Note that the degeneracy direction means this shift can move to a shift in w_0 if the best fit happened to be at higher $\Omega_{m,0}$. See figure 4.2 that shows the covariance between $\Omega_{m,0}$ and w_0.

4.6 Adding Uncertainties

4.6.1 Simple Approach

In order to estimate the uncertainty on the peculiar velocity correction we add the sources of uncertainty in quadrature.

$$\sigma_{z,\mathrm{pec}}^2 = \frac{\sigma_{\mathrm{LT}}^2 + \sigma_{\mathrm{SN}}^2 + \sigma_{\mathrm{MD}}^2}{c^2} \tag{4.7}$$

where the uncertainties are σ_{LT} from the limits of linear theory, σ_{SN} from shot noise, and σ_{MD} from missing data in units of $\mathrm{km\,s^{-1}}$. Linear theory assumes that the universe is statistically isotropic and homogeneous containing only Gaussian density fluctuations. On smaller scales this is not strictly the case, including the scales at which the peculiar velocity correction is relevant; that is the source of the σ_{LT}^2 term. From Carrick et al. (2015) and correspondence with Prof. Michael Hudson we estimate that this term is of order 150 $\mathrm{km\,s^{-1}}$. From Prof. Michael Hudson we additionally have that the shot noise term, σ_{SN}^2, is of order 125 $\mathrm{km\,s^{-1}}$, and the missing data term, σ_{MD}^2, is of order 100 $\mathrm{km\,s^{-1}}$. Together this gives a $\sigma_{z,\mathrm{pec}} \approx 0.0007$ (corresponding to a peculiar velocity uncertainty of 220$\mathrm{km\,s^{-1}}$). The total uncertainty in the observed redshift is then $\sigma_z = (1+z_{\mathrm{cor}})\sigma_{z,\mathrm{pec}}$ (see Davis et al. (2011), Eq. A1). For practical reasons it is easier to convert this uncertainty on redshift to an uncertainty on the distance modulus, μ, using the relation (Davis et al. (2011), Eq. A4)

$$\sigma_\mu(z_{\mathrm{cor}}) = \sigma_z \frac{5}{\ln(10)} \left[\frac{(1+z_{\mathrm{cor}})}{z_{\mathrm{cor}}(1+z_{\mathrm{cor}}/2)}\right] = \sigma_{z,\mathrm{pec}} \frac{5}{\ln(10)} \left[\frac{(1+z_{\mathrm{cor}})^2}{z_{\mathrm{cor}}(1+z_{\mathrm{cor}}/2)}\right] \tag{4.8}$$

where z_{cor} is the redshift of the galaxy in question in the CMB frame corrected for peculiar velocities. In the derivation of equation 4.8 an empty universe is assumed. At high redshift this is a poor assumption, but for redshifts up to and under $z = 0.1$ this assumption gives at worst rise to a 2% fractional error in σ_μ when comparing the σ_μ for the assumed empty universe to that of a $\Omega_{m,0} = 0.3$, $\Omega_{\Lambda,0} = 0.7$ ΛCDM universe.

4.6.2 Correlated Approach

We could choose to build upon the approach of the previous subsection by taking into account spatial correlations in the peculiar velocity corrections. Like previously we have an uncertainty on the redshift $\sigma_{z,\mathrm{cor}}$ given by

$$\sigma_{z,\mathrm{pec}}^2 = \frac{\sigma_{\mathrm{LT}}^2 + \sigma_{\mathrm{SN}}^2}{c^2} \tag{4.9}$$

where we still have a term from the limits of linear theory and shot noise, but not for the missing data. Rather, to more properly take into account the effects of the missing data we add a term

$\sigma^2_{\mathrm{MD}}/c^2$ to the diagonal of the data covariance matrix

$$\Sigma = \begin{pmatrix} \sigma_{1,1} + \sigma^2_{\mathrm{MD}}/c^2 & \sigma_{1,2} & \cdots & \sigma_{1,n} \\ \sigma_{2,1} & \sigma_{2,2} + \sigma^2_{\mathrm{MD}}/c^2 & \cdots & \sigma_{2,n} \\ \vdots & \vdots & \ddots & \vdots \\ \sigma_{m,1} & \sigma_{m,2} & \cdots & \sigma_{m,n} + \sigma^2_{\mathrm{MD}}/c^2 \end{pmatrix}. \tag{4.10}$$

In the above $\sigma_{m,n}$ is shorthand for the multiplication $\sigma_m \, \sigma_n$. The reason why this approach is more appropriate is that the uncertainties of galaxies in close proximity are correlated. If we have large uncertainties for one particular supernova then nearby supernovae are likely to also have large uncertainties. To calculate the values to add to the diagonal of Σ we would have to simulate our sample of SNe multiple times. This is not trivial, as it is crucial to get the assumptions made when performing these simulations right. Considering the size of the uncertainties and the potential impact of this effect (see e.g. table 4.1 and the figure attached below) we have chosen to not perform these simulations, and stick with the approach of section 4.6.1.

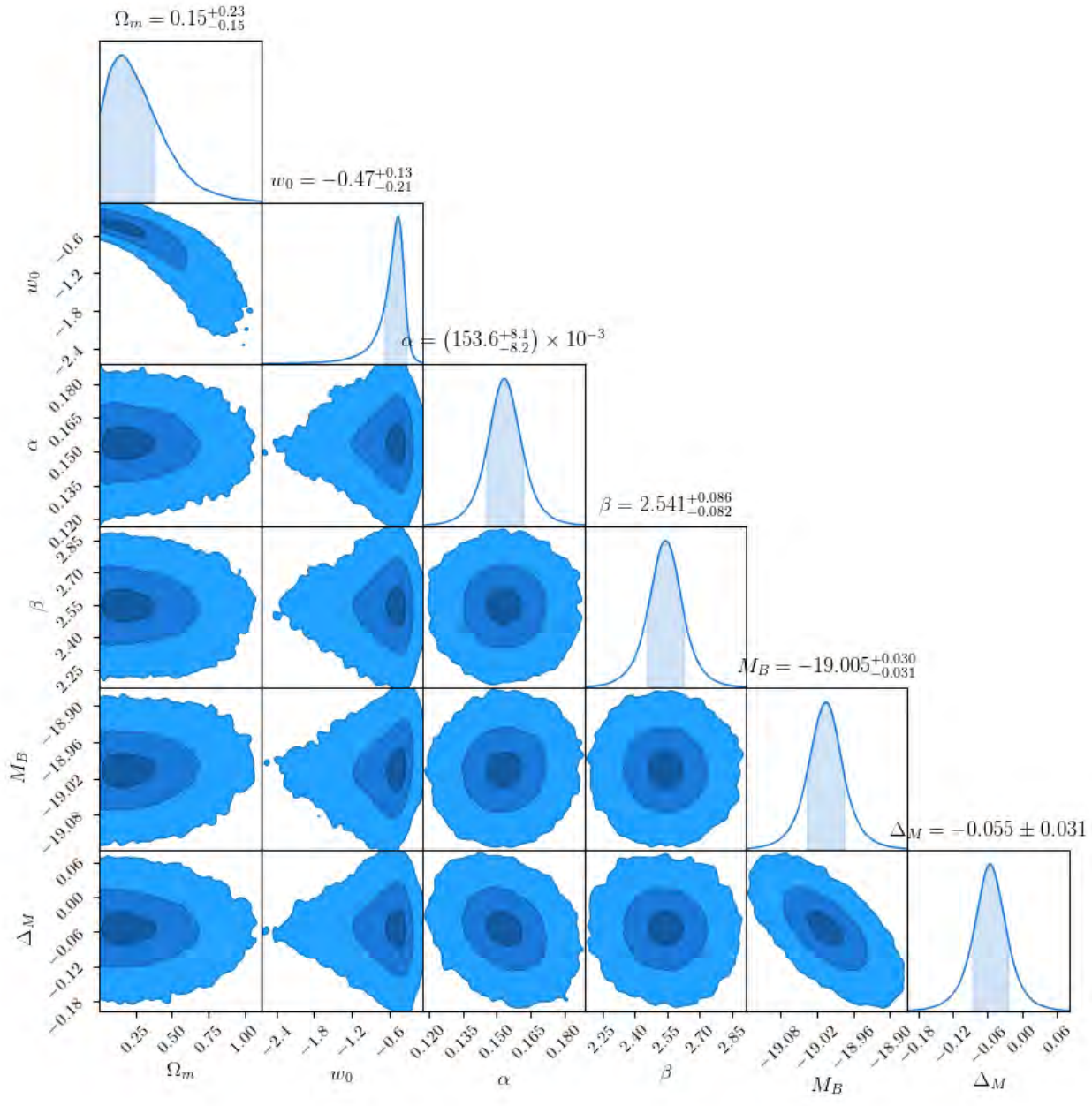

Figure 4.2: Corner plot showing the covariance between fitted parameters and maximum likelihood parameters and associated 68% likelihood marginalised uncertainties for the $f = 0.0$ case.

Chapter 5

Discerning Dark Energy Models with High-Redshift Standard Candles

This chapter contains the paper "Discerning dark energy models with high-redshift standard candles" by Andersen, P., and Hjorth, J., 2017, MNRAS, doi: 10.1093/mnras/stx1975

5.1 Abstract

Following the success of type Ia supernovae in constraining cosmologies at lower redshift ($z \lesssim 2$), effort has been spent determining if a similarly useful standardisable candle can be found at higher redshift. In this work we determine the largest possible magnitude discrepancy between a constant dark energy ΛCDM cosmology and a cosmology in which the equation of state $w(z)$ of dark energy is a function of redshift for high redshift standard candles ($z \gtrsim 2$). We discuss a number of popular parametrisations of $w(z)$ with two free parameters, w_zCDM cosmologies, including the Chevallier-Polarski-Linder and generalisation thereof, nCPL, as well as the Jassal-Bagla-Padmanabhan parametrisation. For each of these parametrisations we calculate and find extrema of $\Delta\mu$, the difference between the distance modulus of a w_zCDM cosmology and a fiducial ΛCDM cosmology as a function of redshift, given 68% likelihood constraints on the parameters $P = (\Omega_{m,0}, w_0, w_a)$. The parameters are constrained using cosmic microwave background, baryon acoustic oscillations, and type Ia supernovae data using CosmoMC. We find that none of the tested cosmologies can deviate more than 0.05 mag from the fiducial ΛCDM cosmology at high redshift, implying that high redshift standard candles will not aid in discerning between a w_zCDM cosmology and the fiducial ΛCDM cosmology. Conversely, this implies that if high redshift standard candles are found to be in disagreement with ΛCDM at high redshift, then this is a problem not only for ΛCDM but for the entire family of w_zCDM cosmologies.

5.2 Introduction

The concordance ΛCDM model, containing a dark energy (Λ) component with constant equation of state and a cold dark matter (CDM) component, has been successful in explaining observations

of a large number of cosmological probes, including supernovae (SNe), baryon acoustic oscillations (BAO) and the power spectrum of the cosmic microwave background (CMB). Anomalies do however exist (Ade et al., 2016), and a number of alternatives to ΛCDM have been proposed. One proposed modification is allowing the equation of state to vary with redshift. We call this family of models w_zCDM models. A number of other alternative modifications include modified gravity, such as $f(R)$ models (Buchdahl, 1970; Sotiriou and Faraoni, 2010) where the Ricci scalar R is replaced with a function of R, or redshift remapping (Wojtak and Prada, 2017) where the assumption of a $a = (1 + z)^{-1}$ relation between the scale factor a and redshift z is broken in favour for a relation that is a function of redshift. In this work we focus exclusively on the first kind of models, the w_zCDM cosmologies.

Type Ia supernovae (SNe) are used as standard candles at lower redshifts. At redshifts of $z \gtrsim 2$ they are less useful, in part due to the decreasing Ia SNe rate (Rodney et al., 2014). Recently a range of high redshift standard candles have been proposed, including active galactic nuclei (AGN) (King et al., 2013; Hönig et al., 2017), gamma ray bursts (GRB) (Amati et al., 2016), gamma ray burst supernovae (GRB-SNe) (Li et al., 2014; Cano, 2014), superluminous supernovae (SLSNe) (Inserra and Smartt, 2014; Scovacricchi et al., 2016), quasars (Risaliti and Lusso, 2015; Lopez-Corredoira et al., 2016) and high redshift HII galaxies (Terlevich et al., 2015). In this work we investigate the usefulness of such high redshift standard candles for constraining dark energy models. We choose to neither use a Fisher matrix approach, where ΛCDM parameters are assumed, nor to assume a ΛCDM cosmology to generate mock datasets. Rather, we introduce the quantity $\Delta\mu(z)$ which is defined as the difference between the distance modulus of a w_zCDM cosmology and fiducial ΛCDM cosmology as a function of redshift. Fiducial ΛCDM cosmology is in this work defined as the best fitting ΛCDM cosmology. Previous work has applied a similar approach (Perlmutter and Schmidt, 2003; Aldering et al., 2007) to argue that discerning a non-constant dark energy component from a constant dark energy will require high precision measurements. Since then the amount of data to constrain proposed cosmologies has grown, not only in quantity but also extended to increasingly higher redshifts. This allows us to revisit this approach, specifically asking whether any w_zCDM cosmology can deviate significantly in predicted distance modulus from fiducial ΛCDM at high redshift, given current cosmological constraints. If w_zCDM cosmologies are indistinguishable from the fiducial ΛCDM cosmology at high redshifts, this would imply that high redshift ($z \gtrsim 2$) data points will have limited usefulness over low redshift ($z \lesssim 2$) equivalents when discerning between the two types of cosmologies. Additionally it would imply that if precise measurements of standard candles at high redshift are shown to be in disagreement with ΛCDM cosmology, this would not only challenge ΛCDM cosmology but also the entire family of w_zCDM cosmologies.

Quintessence is a proposed form of dark energy (Ratra and Peebles, 1988; Caldwell et al., 1997; Tsujikawa, 2013), which introduces a scalar field that is minimally coupled to gravity to explain the apparent accelerated expansion observed at low redshifts. In this work we use theoretical concepts from quintessence to guide us in determining which w_zCDM models to test. In

quintessence exists two subgroups of dark energy models, the thawing (Scherrer and Sen, 2008; Chiba, 2009; Gupta et al., 2015) and the freezing (Scherrer, 2006; Sahlén et al., 2007; Schimd et al., 2007) models. In thawing dark energy models the scalar field is nearly frozen due to the potential being dampened by Hubble friction in the early matter dominated universe, with the scalar field then starting to evolve once the field mass is below the Hubble expansion rate. In freezing dark energy models the potential is steep enough in the early universe that a kinetic term develops. At later stages the evolution of the field, and therefore also the evolution of the equation of state, steadily slows down as the potential is tending towards being shallow. These two families of models produce distinct behaviours for the evolutions of the equation of state. The equation of state function $w(z)$ of thawing dark energy models are generically convex decreasing functions of redshift, while freezing dark energy models produce $w(z)$ functions that are convex increasing functions of redshift. Phenomenological parametrisations of $w(z)$ with two free parameters can produce either convex increasing or decreasing behaviour, but not both, making them more suited to fit either an underlying freezing or thawing dark energy model (Pantazis et al., 2016).

The $w(z)$ parametrisations investigated in this work will include some generalisations of ΛCDM, limited to two parameters w_0 and w_a where w_0 is a constant term and the magnitude of w_a determines the strength of the evolution with redshift. Specifically we investigate the Chevallier-Polarski-Linder (CPL) (Chevallier and Polarski, 2000; Linder, 2003) and Jassal-Bagla-Padmanabhan (JBP) (Jassal et al., 2004) parametrisations as well as the nCPL generalisation of Pantazis et al. (2016).

In section 5.3 we introduce and motivate the parameter $\Delta\mu$, and discuss previous work that has used a similar approach. Then in section 5.4 we discuss parametrisations of $w(z)$ and the reasoning behind choosing the subset of parametrisations adopted in this paper. In section 5.5, we describe the method used to derive extrema of $\Delta\mu$ for the chosen parametrisations, and in section 5.6 we present the results. Finally in section 5.7 we discuss the implications of our results for using high redshift standard candles to constrain dark energy models.

5.3 The $\Delta\mu$ parameter

Previous works have discussed the utility of high redshift standard candles in constraining cosmological parameters (King et al., 2013; Scovacricchi et al., 2016) by using either Fisher matrix formalism or simulating data from a high redshift standard candle. While these approaches are appropriate for forecasting the constraining power of a survey, they are less suited for our purpose. Therefore we introduce the $\Delta\mu$ parameter, given as $\Delta\mu(z, P) = \mu_{w_z\mathrm{CDM}}(z, P) - \mu_{\Lambda\mathrm{CDM}}(z)$. Here $\mu_{w_z\mathrm{CDM}}(z, P)$ is the distance modulus of a w_zCDM cosmology given a set of parameters $P = (\Omega_{m,0}, w_0, w_a)$, and $\mu_{\Lambda\mathrm{CDM}}(z)$ the distance modulus of the best fitting ΛCDM cosmology, for a given redshift z.

Looking at the differences in magnitude as a function of redshift predicted by different cosmologies has been done before in the literature. Perlmutter and Schmidt (2003) plot the magnitude difference between a ($\Omega_{m,0}$, $\Omega_{\Lambda,0}$)=(0.3, 0.7) ΛCDM cosmology and a wCDM cosmology where the equation of state of dark energy is allowed to vary between $w = -1.5$ and $w = -0.5$, out to a redshift of $z = 1.7$. Within the parameter range they find a maximum magnitude difference of approximately $\sim$0.3 mag. Aldering et al. (2007) determine the magnitude difference between a ΛCDM cosmology with $w = -1$ and wCDM cosmologies with $w = +1$, $w = 0$, and $w = -\infty$, respectively, in the redshift range [1.7,3]. The maximum magnitude difference they find is less than 0.04 mag. In this work we define a method that for a chosen w_zCDM cosmology selects a range of parameter values $P = (\Omega_{m,0}, w_0, w_a)$ which reflect how strongly constrained the parameters are by the data. This is done by selecting all parameter values that lie within the 68% likelihood contour spanning the $\Omega_{m,0}$, w_0, and w_a parameter space, given observational constraints. The method is described in detail in section 5.5 and Appendix E.

5.4 Dark Energy Equation of State Parametrisations

Testing all proposed models for $w(z)$ is not possible so a sample thereof must be chosen. We use concepts from quintessence dark energy models as a guide. Specifically we apply the predicted evolution of $w(z)$ from the two subclasses of quintessence, the thawing and freezing models. In quintessence, thawing models produce convex decreasing $w(z)$ functions of redshift whereas freezing models produce convex increasing $w(z)$ functions of redshift. For a review of current constraints on some freezing and thawing quintessence models see Dhawan et al. (2017). When going beyond thawing and freezing quintessence, phenomenological models can produce concave behaviour of $w(z)$ and also enter the phantom regime where $w(z) < -1$. This is illustrated in Fig. 5.1. In this work we do not exclude solutions where the $w(z)$ function enters the phantom regime. However, we clearly indicate any results in both figures and discussion that arise from such phantom models.

Regardless of whether the phantom regime is excluded, models better suited for fitting an underlying thawing cosmology are unable to deviate significantly from the fiducial $w = -1$ at high redshifts unless they also do so at low redshifts. The bulk of the current cosmological constraints exists at low redshifts. We therefore expect that models better suited for fitting an underlying freezing dark energy are able to deviate from fiducial ΛCDM cosmology at higher redshifts more than models better suited for fitting an underlying thawing dark energy model. This motivates dividing phenomenological models into two categories, those better suited for fitting an underlying thawing dark energy and those better suited for fitting and underlying freezing dark energy. Pantazis et al. (2016) show that CPL, JBP, and n=3 nCPL (n3CPL) are better suited for fitting an underlying thawing cosmology and a n=7 nCPL (n7CPL) model is better suited for fitting an underlying freezing cosmology.

A phenomenological model better suited for fitting an underlying thawing dark energy can re-

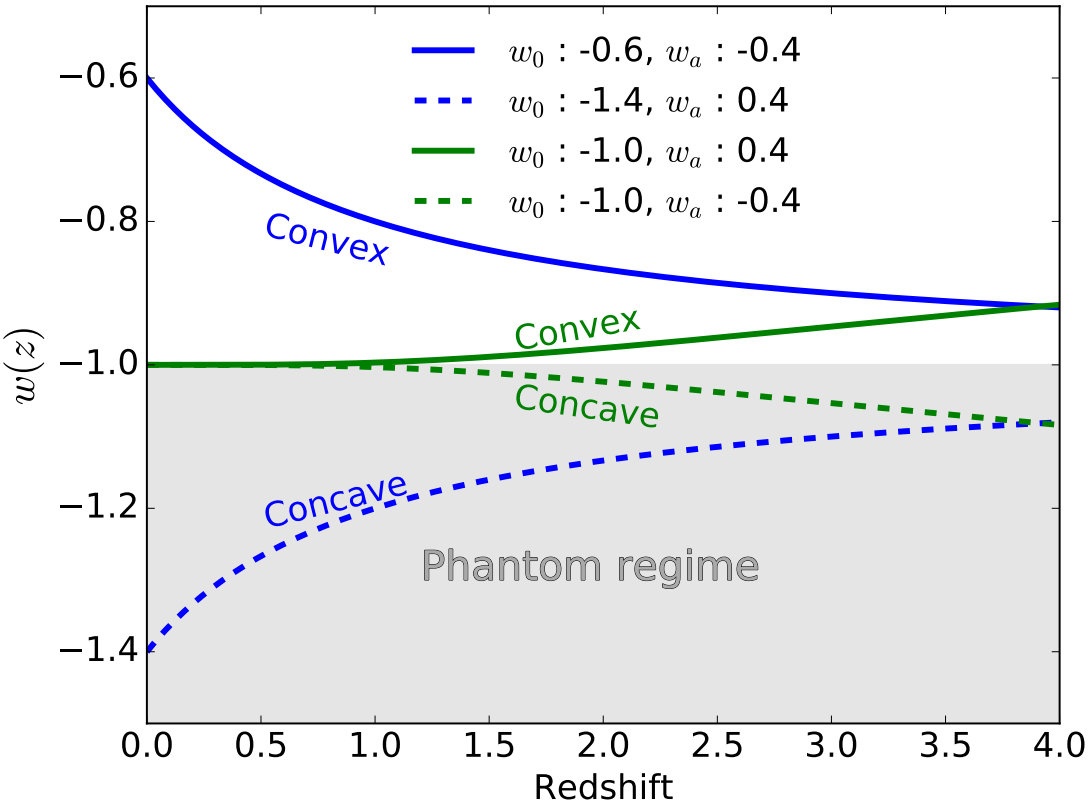

Figure 5.1: A plot of the equation of state parameter as a function of redshift for the CPL (blue) model and n7CPL (green) model. Looking at the full lines this figure illustrates the convex decreasing and increasing behaviour of thawing and freezing dark energy models, respectively. If the $w(z)$ are allowed to enter the phantom regime where $w(z) < -1$ then the dashed concave behaviour becomes possible. In the phantom regime we see the CPL function being concave instead of convex, and increasing instead of decreasing. Likewise the n7CPL model in the phantom regime changes behaviour to become concave instead of convex, and decreasing instead of increasing.

produce observables for a cosmology with a freezing dark energy. Putter and Linder (2008) show that the CPL model reproduces distances of freezing dark energy models, such as the supergravity inspired SUGRA model, to within 0.1%. However, as shown by Pantazis et al. (2016), fitting a freezing dark energy with a model better suited for fitting an underlying thawing dark energy, and vice versa, can lead to incorrect values of $w(z = 0)$ or phantom behaviour which are not present in the underlying cosmology.

We therefore include the CPL model (Chevallier and Polarski, 2000; Linder, 2003)

$$w_{\rm CPL} = w_0 + w_a(1 - a) = w_0 + w_a \frac{z}{1 + z}, \tag{5.1}$$

the JBP model (Jassal et al., 2004)

$$w_{\rm JBP} = w_0 + w_a(1 - a)a = w_0 + w_a \frac{z}{(1 + z)^2}, \tag{5.2}$$

and the nCPL model (Pantazis et al., 2016)

$$w_{n\rm CPL} = w_0 + w_a(1 - a)^n = w_0 + w_a \left(\frac{z}{1 + z} \right)^n, \tag{5.3}$$

where we, guided by Fig. 16 of Pantazis et al. (2016), choose a n3CPL and a n7CPL cosmology. Since models appropriate for fitting an underlying freezing dark energy are much less constrained in especially the w_a parameter, running CosmoMC until convergence takes much longer time for this type of model than for the models better suited for fitting an underlying thawing dark energy. Therefore only one model of the first type is included, namely the n7CPL model.

5.5 Method

To derive 68% likelihood constraints on the models described in the previous section, the CosmoMC (Lewis and Bridle, 2002; Lewis, 2013) MCMC tool was utilised. All cosmologies were fit with the same data, including observations of type Ia supernovae from the Joint Light-Curve Analysis, baryon acoustic oscillations from SDSS-III and 6dF and the cosmic microwave background from the Planck Collaboration. For more details and references to the data sets used see Appendix F. To allow maximum flexibility in the fitting routines all parameters for the datasets used were kept free for CosmoMC to fit, e.g. the stretch and colour parameters α and β for the JLA sample. Since our focus is to investigate the effects of different dark energy models, and to limit computation time, we assume flatness, and neglect radiation. For each of the models described above (CPL, nCPL, and JBP) we derive the 3-dimensional likelihood contours of $\Omega_{m,0}$, w_0, and w_a. When searching for extrema of $\Delta\mu(P, z)$ as a function of redshift, only the parameter values $P = (\Omega_{m,0}, w_0, w_a)$ that lie on the surface of the 68% likelihood volume are used. Appendix E discusses how this is possible by applying the extreme value theorem.

For a Hubble constant in units of km s^{-1}Mpc^{-1}, the distance modulus is given by

$$\mu(P,z) = 5\log_{10}\left[D'_L(P,z)\right] + 5\log_{10}\left[c/H_0\right] + 25 + \sigma_m, \tag{5.4}$$

where $D'_L(P,z)$ is the unitless luminosity distance (D'_L=$D_L\,H_0\,c^{-1}$), D_L is the luminosity distance, and σ_m is a constant representing how far this magnitude is from the correct intrinsic absolute magnitude of the observed supernovae. σ_m and $5\log_{10}\left[c/H_0\right]$ are both additive terms, and combined in a parameter K to be marginalised over,

$$K = 5\log_{10}\left[c/H_0\right] + 25 + \sigma_m. \tag{5.5}$$

The marginalisation process is performed by minimising the sum

$$\begin{aligned}\chi^2(K) &= \sum_i \left(\frac{\mu_{w_z\mathrm{CDM},i}(P,z) - \mu_{\mathrm{JLA},i}}{\sigma_{i,\mathrm{JLA}}}\right)^2 \\ &= \sum_i \left(\frac{5\log_{10}\left[D'_L(P,z)_{w_z\mathrm{CDM},i}\right] + K - \mu_{\mathrm{JLA},i}}{\sigma_{i,\mathrm{JLA}}}\right)^2\end{aligned} \tag{5.6}$$

by varying K. The sum goes over the JLA type Ia SNe (Betoule et al., 2014b) with distance modulus $\mu_{\mathrm{JLA},i}$ and associated uncertainty on the distance modulus $\sigma_{i,\mathrm{JLA}}$. The scheme explained above to recover K is similar in purpose to the process described in Appendix A.1 of Goliath et al. (2001). The process of finding the value of K that minimises Eq. 5.6 is done for all parameter values $P = (\Omega_{m,0}, w_0, w_a)$ that lie on the surface of the 68% likelihood contour. Having determined the value K that minimises Eq. 5.6, we can calculate $\Delta\mu$ as a function of redshift for parameters P of, e.g., the CPL model

$$\begin{aligned}&\Delta\mu_{CPL}(P,z) = \\ &\mu_{\mathrm{CPL}}(P,z) + K_{\mathrm{CPL}}(P) - (\mu_{\Lambda\mathrm{CDM,bf}}(z) + K_{\Lambda\mathrm{CDM},bf}).\end{aligned} \tag{5.7}$$

In summary the process to derive $\Delta\mu$ values for a given dark energy model is

1. Run CosmoMC for given dark energy model.
2. Derive from CosmoMC output 68% likelihood contours for parameters $P = (\Omega_{m,0}, w_0, w_a)$.
3. Calculate K for all parameter values $P = (\Omega_{m,0}, w_0, w_a)$ on 68% likelihood contour.
4. Calculate $\Delta\mu(P,z)$ for all parameter values $P = (\Omega_{m,0}, w_0, w_a)$ on 68% likelihood contour.

The above process would not be necessary if H_0 and the absolute magnitude of the standard candle were known exactly. If they were known, their values could be substituted directly into Eq. 5.4.

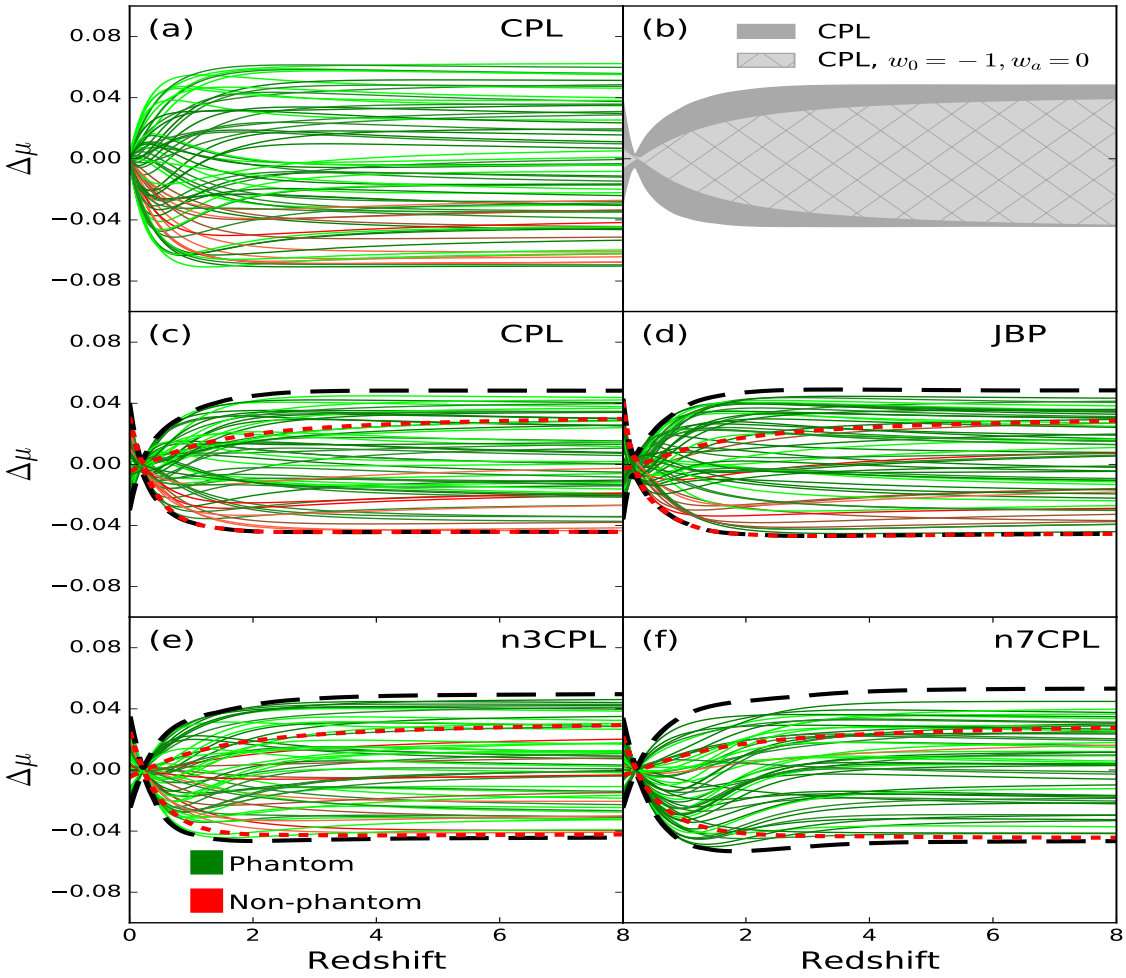

Figure 5.2: $\Delta\mu(z, P)$ as a function of redshift for the tested cosmologies. The green and red lines show $\Delta\mu(z, P)$ curves for a representative subsample of all tested parameters $P = (\Omega_{m,0}, w_0, w_a)$. Green lines correspond to $\Delta\mu$ values from a dark energy model that crosses the phantom divide, $w < -1$, where red lines are models where for all redshifts $w \geq -1$. Likewise the black dashed lines show extrema when placing no restrictions on evolution of equation of state and red dashed lines showing extrema when excluding models where the equation of state enters the phantom region. **(a)** $\Delta\mu$ plot for the CPL w_zCDM cosmology showing the extrema of $\Delta\mu(z, P)$ as a function of redshift given the 68% likelihood constraints derived using CosmoMC, ignoring the marginalisation constant K from Eq. 5.5. **(b)** $\Delta\mu$ plot for the CPL w_zCDM cosmology, showing the extrema of $\Delta\mu(z, P)$ as a function of redshift, given the 68% likelihood constraints derived using CosmoMC. The dark grey shaded area is where all parameters $\Omega_{m,0}$, w_0, w_a have been allowed to vary, and the light grey hatched where only $\Omega_{m,0}$ varies and w_0 and w_a are fixed at the ΛCDM values of $w_0 = -1$ and $w_a = 0$ respectively. The plot illustrates that most of the magnitude discrepancy with the best fitting ΛCDM comes from the uncertainty in $\Omega_{m,0}$, rather than the choice of dark energy model and uncertainty in w_0 and w_a. **(c)** $\Delta\mu$ plot for the CPL w_zCDM cosmology, showing the extrema of $\Delta\mu(z, P)$ as a function of redshift, given the 68% likelihood constraints derived using CosmoMC. Black dashed lines show extrema for $\Delta\mu$. Red dashed lines show extrema for $\Delta\mu$ excluding dark energy models that at any redshift has a phantom value for the quation of state of dark energy, $w < -1$. **(d)** Like panel (c) but for the JBP w_zCDM cosmology. **(e)** Like panel (c) but for the n3CPL w_zCDM cosmology. **(f)** Like panel (c) but for the n7CPL w_zCDM cosmology.

5.6 Results

The results are shown in Fig. 5.2. Before discussing them we address two important topics. Firstly, the effects of the constant K (Eq. 5.5). Secondly, how large a part of $\Delta\mu$ that originates from uncertainty in $\Omega_{m,0}$ and how large a part that comes from the choice of dark energy model and uncertainty in w_0 and w_a. In discussing these topics we only investigate the CPL model in detail and summarise results for the JBP, $n3$CPL, and $n7$CPL models; an in-depth discussion for the latter three models can be found in Appendix G.

5.6.1 Effects of K

$\Delta\mu$ values for a representative sample of the parameters $P = (\Omega_{m,0}, w_0, w_a)$ lying on the 68% likelihood surface of $\Omega_{m,0}$, w_0, w_a parameter space for the the CPL cosmology are shown in panel (a) of Fig. 5.2. Importantly in this figure the marginalisation constant K from Eq. 5.5 has been ignored. As one would then expect, $\Delta\mu \to 0$ for $z \to 0$. However, ignoring the marginalisation constant K gives an incomplete picture. Neither the Hubble constant nor the intrinsic absolute magnitude of the type Ia SNe are known precisely. If they were then panel (a) would be appropriate, but since they are not we must include the marginalisation parameter K. The $\Delta\mu$ values for the CPL cosmology, including the marginalisation constant K, are shown in panel (c) of Fig. 5.2, with the extrema of $\Delta\mu$ shown as dashed lines. Including the marginalisation constant introduces scatter around $z \approx 0$, which is due to the fact that the values of K differ for different parameter values. Furthermore, the extrema of the $\Delta\mu$ values become smaller. This is to be expected, as the marginalisation process finds the value of K that minimises the difference between the distance moduli of the cosmological models and the observed SNe Ia magnitudes, for both the w_zCDM and the ΛCDM cosmology. This decreases any disagreement that might exist between the predicted distance moduli of w_zCDM and ΛCDM cosmology. This result also holds true for the JBP, $n3$CPL, and $n7$CPL cosmologies, i.e. including K causes scatter around $z = 0$ and a narrower distribution of $\Delta\mu$ values.

5.6.2 $\Delta\mu$ contribution from $\Omega_{m,0}$ versus w_0 and w_a

When looking at the extrema of $\Delta\mu$ as a function of redshift it is not straightforward to disentangle how large a part of the magnitude difference is caused by uncertainty in $\Omega_{m,0}$ and how much stems from the choice of CPL w_zCDM cosmology and associated uncertainty in w_0 and w_a. Therefore we produce panel (b) of Fig. 5.2. The dark grey shaded area in panel (b) of Fig. 5.2 is the range of possible $\Delta\mu$ values when all parameters, $\Omega_{m,0}$, w_0, and w_a have been allowed to vary. The light grey hatched area is where only $\Omega_{m,0}$ varies and w_0 and w_a are fixed at the ΛCDM values of $w_0 = -1$ and $w_a = 0$ respectively. Panel (b) of Fig. 5.2 illustrates that most of the magnitude discrepancy with the best fitting ΛCDM comes from the uncertainty in $\Omega_{m,0}$, rather than the choice of dark energy model and uncertainty in w_0 and w_a. Figures analogous to panel (b) of Fig. 5.2, but for the JBP, $n3$CPL, and $n7$CPL cosmologies can be found in Appendix G. They likewise show that the majority of the discrepancy with the best fitting ΛCDM cosmology comes from the

uncertainty in $\Omega_{m,0}$, rather than the choice of w_zCDM model and uncertainty in w_0 and w_a.

5.6.3 Thawing Models

In this subsection the results for the models better suited for fitting an underlying thawing model are presented, namely the results of the CPL, JBP, and $n3$CPL models. In panels (c), (d), and (e) of Fig. 5.2, $\Delta\mu$ values are plotted for a representative sample of the parameter values $P = (\Omega_{m,0}, w_0, w_a)$ on the 68% likelihood contours of the CPL, JBP, and $n3$CPL cosmologies. The overall agreement between the models is remarkable. The extrema of $\Delta\mu$ for all three models are found at redshift $z \sim 2$, which aligns with the prediction of ΛCDM that dark energy has negligible influence at larger redshifts. Our results are consistent with the findings of King et al. (2013) who use Fisher matrix analysis to show that a long redshift baseline is important to achieve tight constraints on w_0 and w_a for the CPL cosmology, but any measurements beyond a redshift of $z \sim 2$ provide negligible additional constraints compared to that of a lower redshift equivalent.

The maximum absolute value of $\Delta\mu$ when placing no restrictions on the evolution of the equation of state of dark energy is approximately 0.05 mag for all models discussed in this section. When discarding results where the equation of state enters the phantom regime the lower limits are not strongly affected, but the upper extrema reduces to approximately 0.03 mag.

These results imply that the additional power of high redshift standard candles to discern between ΛCDM and CPL, JBP, and $n3$CPL cosmology is limited when compared to low redshift standard candles. It also indicates that CPL, JBP, and $n3$CPL cosmology can only deviate slightly from ΛCDM at large redshifts.

5.6.4 Freezing Model

In this subsection the results for the model better suited for fitting an underlying freezing cosmology, namely the $n7$CPL model, are presented. In panel (f) of Fig. 5.2 a representative sample of $\Delta\mu$ values as well as the extrema as dashed lines are plotted for the $n7$CPL cosmology. Overall the similarity to the corresponding plots for the CPL, JBP and $n3$CPL models is strong. In Fig. 5.3 the $\Delta\mu$ extrema for all tested cosmologies are overplotted for comparison. It is apparent that the CPL, JBP, and $n3$CPL models give similar results at both low and high redshift. As expected the $n7$CPL model has the largest extrema at high redshift, but only slightly larger values. This analysis suggests that the conclusion for the $n7$CPL cosmology is similar to that of the CPL, JBP and $n3$CPL cosmologies. Given current constraints they are all unable to deviate significantly from fiducial ΛCDM at high redshifts. For the $n7$CPL model most of the disagreement with the fiducial ΛCDM comes from the uncertainty in $\Omega_{m,0}$, rather than the choice of dark energy or uncertainty in w_0 and w_a, just as was the case with the CPL, JBP, and $n3$CPL models.

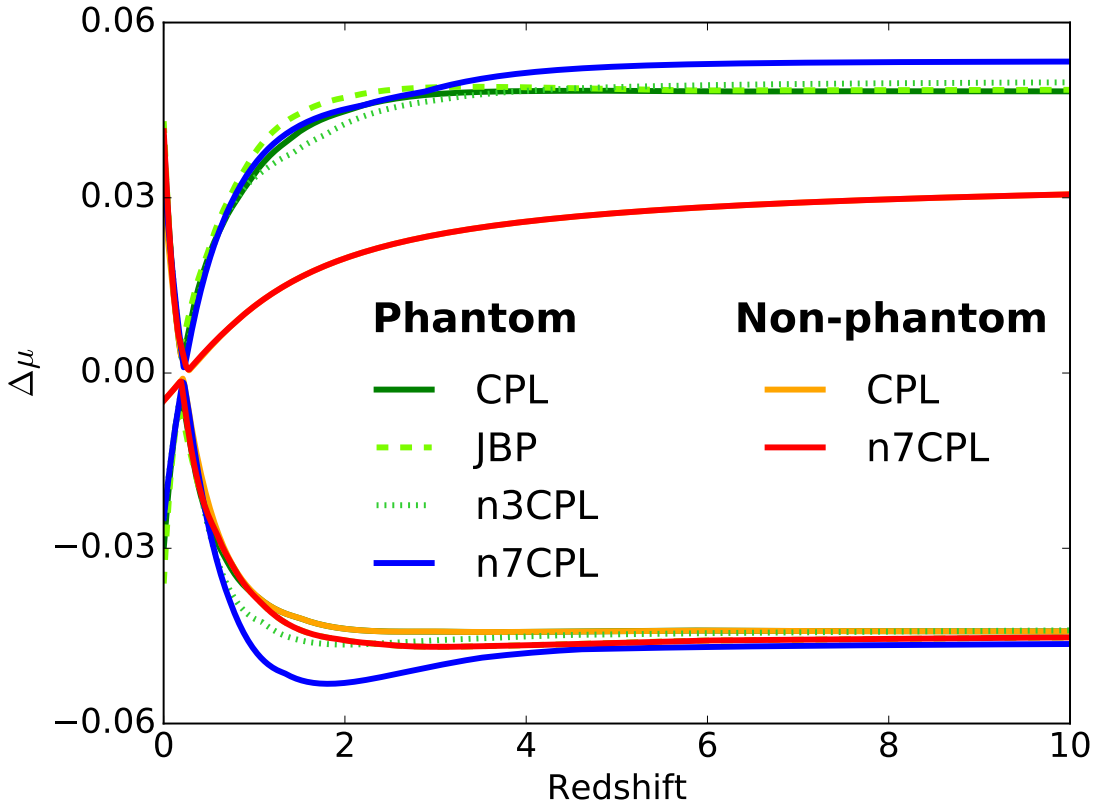

Figure 5.3: The extrema of $\Delta\mu$ for the CPL, JBP, $n3$CPL, and $n7$CPL models. The figure illustrates that the models better suited for fitting an underlying thawing dark energy, CPL, JBP and $n3$CPL, all give very similar results. The one model better suited for fitting an underlying freezing dark energy, $n7$CPL, has only slightly larger extrema for $\Delta\mu$ at high redshift. The red and orange lines show the extrema of the CPL and $n7$CPL excluding phantom models. The non-phantom extrema of the JBP and $n3$CPL models are indistinguishable from those of the CPL model and are therefore not shown.

5.7 Discussion

Our analysis shows that none of the tested cosmologies can deviate significantly from fiducial ΛCDM cosmology at high redshift, given current cosmological constraints. As a consequence, high redshift ($z \gtrsim 2$) standard candles will not add significant additional constraints over that of low redshift equivalent standard candles, when discerning between ΛCDM cosmology and CPL, JBP, $n3$CPL, or $n7$CPL cosmology. Since our analysis further shows that the bulk of the disagreement with the fiducial ΛCDM cosmology for all tested models primarily comes from the uncertainty in $\Omega_{m,0}$, rather than the choice of dark energy model and uncertainty in w_0 and w_a, we conjecture that if the analysis was to be carried out for any other w_zCDM cosmology, it would arrive at results very similar to those of our analysis. The choice of dark energy model seems to have negligible impact on high redshift behaviour, regardless of whether we consider the models better suited for fitting an underlying freezing or thawing cosmology.

From our analysis alone it is not possible to conclude that in general no other model better suited for fitting an underlying freezing dark energy could significantly deviate from fiducial ΛCDM at high redshifts. Linder (2017) investigated a number of freezing dark energy models. Specifically, Linder (2017) produced two parameter functions to calculate observables, such as the dark energy equation of state, for a number of models including the inverse power law (IPL) and supergravity (SUGRA) models. Combined these models span a wide range of possible behaviours for the dark energy equation of state as a function of redshift. Linder (2017) shows that the observables of these complicated models can be approximated with a phenomenological function of two parameters. Varying just these two parameters is sufficient to reproduce the behaviour of these more complicated models with many parameters to within 2.4% accuracy in the equation of state. The findings of Linder (2017) are not directly transferable to our analysis, but indicate that the complicated behaviour of these dark energy models can be reproduced reliably with just two free parameters. This suggests that even more complicated dark energy models may have very similar behaviour in the equation of state of dark energy, and that our test of the $n7$CPL model may therefore be representative for the much larger family of possible w_zCDM models better suited for fitting an underlying freezing dark energy. This indicates that no w_zCDM cosmology with only two free parameters for the dark energy redshift behaviour, either thawing or freezing, can deviate significantly from the best fitting ΛCDM at high redshift.

At high redshift additional observational effects beside precision of measurements can impact the usefulness of standard candles. Holz and Linder (2005) discuss the effects of gravitational lensing, noting that since the amplification probability distribution is skewed towards deamplification, gravitational lensing will introduce a bias in the measured magnitudes. Holz and Linder (2005) find that for a standard candle with intrinsic dispersion of 0.1 mag at redshift 2, gravitational lensing introduces an offset with a mode of 0.03 mag. This effect is of similar size to the maximum offset of 0.05 mag we find for the models tested in this work. This further strengthens the argument that if high redshift standard candles are found to be in disagreement with ΛCDM

cosmology, no w_zCDM cosmology will be able to resolve that disagreement.

Current or future surveys investing time into measuring high redshift ($z \gtrsim 2$) standard candles could do so for a number of reasons. If the goal is to discern any w_zCDM model of the types tested here from a standard ΛCDM cosmology then the time is best spent observing at redshifts of $z \sim 2$ or lower. However, if the goal is to determine whether the predictions of ΛCDM hold true at high redshift then going to $z \gtrsim 2$ or higher is recommended, since in this regime there is the added bonus that if ΛCDM is found to give incorrect predictions, then so will any w_zCDM cosmology of the kinds tested in this work.

Acknowledgements

The authors would like to thank Eric Linder for useful comments and Tamara Davis for many discussions on the content as well as useful comments. The Dark Cosmology Centre was funded by the Danish National Research Foundation.

Chapter 6

Summary and outlook

Looking back at the last century of progress within cosmology, it is remarkable how much progress we have made in answering the questions that existed at the time. At the same time we did however unearth a plethora of questions that still today demand an answer. The discovery of dark energy and dark matter implicates that the baryonic universe that we are a part of only make up roughly five percent of the total energy balance. It could therefore be argued that what we have learnt in the last century of doing cosmology is that we now know that we really know very little about the actual makeup of the universe.

Understanding the physics of the type Ia supernova progenitor is crucial if supernova cosmology is to remain competitive in the future. While there is not solid evidence either way, observations suggest that there may exist more than one type Ia supernova progenitor channel. This has a direct impact on supernova Ia cosmology. See e.g. Zhang et al. (2017) section 3.2.2 where an extra corrective magnitude term ΔM_B is added to magnitude of type Ia supernovae in the most massive galaxies. This can seem like an ad hoc solution to a problem that exists because the underlying physics of the observed object, in this case a type Ia supernovae, is not fully understood. One avenue that allows us to probe the underlying physics is through understanding the delay time distribution of the proposed type Ia supernova progenitors. Delay time distributions also play a role in chemical evolution modelling and modelling proposed surveys of type Ia supernovae. It is with this motivation that chapter 2 discusses two complimentary approaches to describing supernova rates and whether the two approaches can be reconciled. One of the approaches is to measure volumetric rates, while the other looks at averaged rates measured in individual galaxies, typically held up against galaxy properties such as stellar mass and star formation rate. The approach in chapter 2 is to assume a delay time distribution going as τ^{-1} with a transition to being constant at short delay times. From this delay time distribution a model to predict type Ia supernova rate from stellar mass and star formation rate of a galaxy is derived. This model is in excellent agreement with the current observational constraints. The model is then compared to the A+B model through various measures for goodness of fit. For all measures the A+B model performs worse. It is especially in the high specific star formation rate regime that the performance of the A+B model is poor, and the fact that this disagreement exists with a model based on a $\sim\tau^{-1}$ delay time dis-

tribution suggests that there is tension between the A+B model and the τ^{-1} delay time distribution.

There are two points in which the study of chapter 2 can improve significantly. One is in the range in which it makes predictions. In the domain where specific star formation rate values are $\log \mathrm{sSFR} \gtrsim -9$ there is very little data available to constrain models. It is therefore not possible to either confirm or deny whether the developed model is valid in this high specific star formation rate regime. As star formation rate scales (in a non trivial way) with redshift, as more type Ia supernova are observed at larger redshifts it will become possible to constrain models in this regime. Already today there exists data from surveys, e.g. the Ia supernova sample of the Dark Energy Survey, which has so far not been analysed to constrain Ia supernova rates. Upcoming surveys that have just started, like the Zwicky Transient Facility, will also be able to add additional constraints. When these samples are analysed and added to the current data it justifies spending some additional time looking at the statistical modelling. While the A+B model is fairly simple in that it only has two free parameters whose likelihood profiles are fairly gaussian in nature, that is not the case for the more complicated models such as that of Smith et al. (2012), Graur et al. (2015a) or the one presented in chapter 2. Bayesian modelling of the data is a way to improve the statistical rigour and aid in solidifying which model best fits the available data. Especially when it comes to the uncertainties Bayesian modelling will be a significant leap forward, compared to the methods applied in 2.

In chapter 3 we look at utilising peculiar velocities of type Ia supernovae as a signal, specifically we investigate the effects that survey geometry and incomplete sampling of the surveyed volume can have on what bulk flow we should theoretically expect to observe. In order to do this we developed two separate numerical methods that take as input the survey geometry and sampling rate and gives as output the likelihood distribution of bulk flows from linear theory. The two methods are in good agreement and predict bulk flows within a few percent of one another. We find that survey geometry and in particular sampling effects can significantly influence the linear theory prediction. This may explain why some estimates of the local bulk flow are in apparent disagreement with theory, see e.g. Feindt et al. (2013) where the observed type Ia supernovae are divided into bins, and the bins with fewer supernovae predict larger bulk flow velocities. The conclusion is a recommendation that measured bulk flows are not compared to the prediction from linear theory assuming spherical survey geometry and perfect sampling. Rather they should be compared to the linear theory prediction that takes into account the specific survey geometry and sampling rate of the survey in question. Some comparisons between theory and observation in the literature have focused exclusively on the maximum likelihood bulk flow velocity predicted by linear theory. While it is simpler to compare observed bulk flows against this one value, it can result in incorrect or misleading conclusions since the theoretical prediction is not a single value, rather it is a likelihood distribution. We therefore also stress the necessity of folding this entire likelihood distribution into any comparison of theory and observations.

While we show that observational effects such as survey geometry and sampling rates are important, there are multiple opportunities to go even further in improving the methodology when

constraining parameters such as $\Omega_{m,0}$ and σ_8 with peculiar velocities and bulk flows. One avenue is to improve the statistical modelling. This could be done using e.g. STAN, which is open source software for Bayesian statistical inference, to fully take into account the likelihood distribution from theory. Another approach is to improve the quality and quantity of data. With current type Ia supernova data the bulk flow constraints are not tight enough to derive competitive constraints on cosmological parameters. Upcoming surveys such as the Zwicky Transient Facility (Bellm and Kulkarni, 2017) will observe and derive distances to a large number of type Ia supernovae which will help tighten the constraints from bulk flows in two ways. Firstly it will decrease the uncertainties on the measured bulk flow. Secondly the survey geometry will be close to hemispherical, including the galactic band that so far has been avoided in similar surveys, and the large number of observed Ia supernovae allows for much better sampling of the surveyed volume. The effects of non-spherical survey geometry and sampling is that the worse sampling and the more non-spherical the survey geometry is the wider the theoretical distribution of bulk flows becomes. The high sampling rate and much improved survey geometry of the Zwicky Transient Facility will therefore help tighten the theoretical prediction of bulk flows from linear theory, which will make it easier to determine whether or not the theoretical prediction and observations are in tension.

Peculiar velocities of type Ia supernovae contribute to the observed redshifts of the supernova. If the peculiar velocities were distributed isotropically they could simply be interpreted as a source of scatter on the cosmological redshifts. As the local environment is embedded in a bulk motion, these peculiar velocities will however induce a non-trivial systematic redshift effect. In the context of type Ia supernova cosmology we are interested in the cosmological redshift of the type Ia supernovae, and it is therefore necessary to correct the observed redshifts for the effects of these peculiar velocities. In chapter 4 is a discussion of how previous type Ia supernova cosmology studies have corrected for the systematic redshift effects of peculiar velocities and whether these methods are sufficient for the Dark Energy Survey type Ia supernova sample. The uncertainties on the peculiar velocity fields used in these corrections can be quite large. An analysis of the uncertainty on the 2M++ peculiar velocity field used for peculiar velocity correction in the Dark Energy Survey is therefore carried out in chapter 4. The uncertainties on the peculiar velocity field include contributions from the limits of linear theory, shot noise, and missing data and add up to a redshift uncertainty of roughly $\sigma_{z,\mathrm{pec}} \approx 0.0007$ which equates to an uncertainty of 220 km s^{-1}. To determine whether it is necessary to go beyond this method of peculiar velocity correction we wish to determine how large the systematic effects of peculiar velocity are relatively to the statistical uncertainty. To determine this we therefore fit the Dark Energy Survey 3-year Ia supernova sample first with no modifications and thereafter with a synthetic dipole introduced. This synthetic dipole systematically shifts all redshifts below redshift 0.1 (above this redshift the effect is still there, but is insignificant). The size and direction of the synthetic dipole is varied in the range [-160,160] km s^{-1}. We then look at the shift in the cosmological parameters of interest, $\Omega_{m,0}$ and w_0, between the unmodified sample and the samples with a synthetic dipole included. We find that w_0 is nearly unaffected but that $\Omega_{m,0}$ in extreme cases is shifted roughly $\sim$10%. Since this is still below the statistical uncertainty of the Dark Energy Survey 3-year Ia supernova sample the

conclusion is that in this case the current method of peculiar velocity correction is sufficient.

It should be noted that the conclusion reached in chapter 4 is relevant for the Dark Energy Survey Ia supernova sample, and other samples with similar redshift distribution and number of supernovae in their sample. For future surveys with larger number of Ia supernovae the statistical uncertainty will become smaller, and the systematics will therefore become more important, relatively speaking. While the constant redshift uncertainty of $\sigma_{z,\mathrm{pec}} \approx 0.0007$ found in chapter 4 is a sort of averaged out worst case scenario there may be large differences in the local uncertainties of the peculiar velocity field used as the source of peculiar velocities. Specifically some areas of the sky are sampled much more sparsely than others, and in these sparsely sampled regions the peculiar velocity field will have larger uncertainties. Another effect that may be important to propagate in the uncertainty budget is correlations between the peculiar velocities of nearby Ia supernovae. Since the density field is smooth in nature and the peculiar velocity field is derived from the density field these correlations may be quite strong. It is therefore crucial for future Ia supernovae surveys intended for cosmological use to study the potential influence of peculiar velocity effects on their sample and uncertainties. A survey that in particular is interesting in the context of type Ia supernova cosmology and peculiar velocities is the Zwicky Transient Facility which had first light in late 2017. What makes the Zwicky Transient Facility interesting is the combination of three factors. First that they expect to observe over five thousand type Ia supernovae per year, which will significantly decrease the significance of statistical uncertainties. Secondly that they will observe their own sample of low redshift type Ia supernovae to be used in e.g. peculiar velocity corrections and thirdly that they will also be observing in the galactic plane which will improve the sampling rate in regions that have historically suffered from very poor sampling. So similar to the case of bulk flows the Zwicky Transient Facility promises to bring significant progress to the area of peculiar velocity corrections which will aid in keeping future cosmological constraints from type Ia supernovae competitive.

In chapter 5 the utility of high redshift standard candles in discerning between dark energy models is investigated. This is done by introducing the parameter $\Delta\mu(z)$ which is the largest possible magnitude difference between a ΛCDM and some other cosmology at a given redshift, given 68% likelihood constraints. These constraints are derived using CosmoMC and cosmic microwave background, baryon acoustic oscillations, and type Ia supernova data. The non-standard cosmologies are restricted to w_zCDM cosmologies where the equation of state of dark energy is modelled with two free parameters, w_0 which is constant with redshift and w_z which has some model dependent evolution with redshift. The w_zCDM models tested include models classified as thawing, which if they are $w \approx -1$ at low redshift can not deviate from this significantly at larger redshifts, and freezing models which have more freedom to deviate from $w \approx -1$ at larger redshifts and still have a value of w close to -1 at low redshifts. However neither freezing or thawing models of dark energy can deviate significantly from ΛCDM at high redshifts given current constraints, all deviating less than 0.05 magnitudes from ΛCDM cosmology. The reason why all the tested models yield comparable results for $\Delta\mu(z)$ is that the majority of the contribution to $\Delta\mu(z)$ comes from the uncertainty in $\Omega_{m,0}$ rather than the uncertainty in w_0 and w_z. The implication is that if

the question asked by future cosmologists is which of the proposed w_zCDM cosmologies best fit the observations, then high redshift surveys going beyond redshift of $z \approx 2$ will not significantly aid in this effort more than observations at redshifts at or slightly below redshift $z \approx 2$. If however the question asked is whether ΛCDM accurately describes the observed magnitudes of standard candles in the $z \gtrsim 2$ regime then going to higher redshift makes more sense as the discussion in chapter 5 implies that if there is disagreement between observations and ΛCDM at high redshift, then this disagreement will also exist for w_zCDM cosmologies. It will then be possible to potentially falsify not only ΛCDM but also the entire family of w_zCDM cosmologies.

In the context of type Ia supernovae cosmology the results of chapter 5 are interesting, as observing type Ia at redshifts larger than $z \approx 2$ poses significant challenges. These challenges are in part due to the optical light from type Ia supernovae being shifted into the near-infrared or infrared spectrum at these redshifts which is difficult to observe from ground based telescopes. Another challenge is that the type Ia rates at larger redshifts may be decreasing (Rodney et al., 2014), which would imply that there simply are not that many type Ia supernovae to be observed at these redshifts. That $\Delta\mu(z)$ plateaus at a redshift of $\sim$2 indicates that even though it appears unlikely that type Ia supernovae will be observed at significantly above redshift two, they will still likely be a competitive probe of dark energy in the future. Current surveys, such as the Dark Energy Survey, have observed type Ia supernovae out to a redshift of $\sim$1.8 from ground based telescopes while type Ia supernovae have been observed out to a redshift of $\sim$2.5 by space telescopes. At much larger redshifts exists other standard candles such as active galactic nuclei, quasars, gamma ray bursts, gamma ray burst supernovae, superluminous supernovae, and high redshift HII galaxies. Some of these standard candles have been suggested to be viable up to a redshift of $\sim$10 (Demianski et al., 2018). While it will be extremely difficult to distinguish between various w_zCDM cosmologies at these redshift (or rather practically impossible), there is still some value in extending cosmological inquiries to these redshifts. In particular it will be useful in testing the underlying assumptions that are typically made when testing ΛCDM and w_zCDM cosmologies, e.g. the assumption of flatness and general relativity, as e.g. $f(R)$ modifications to general relativity benefit from having observations spanning a large range of redshifts

Going slightly beyond the focus of this thesis on type Ia supernovae there are some very interesting developments in astronomy lately which will impact cosmology, including Ia supernova cosmology. Specifically the observation of a binary neutron star merger (Abbott et al., 2017b) in the nearby universe where an optical counterpart in the form of a kilonova (Abbott et al., 2017c) was observed. These observations enable binary neutron star mergers to be used as standard sirens and distances to the host galaxy that are independent of the distance ladder to be determined. Currently the single observed event constraints the Hubble constant to a precision of $H_0 = 70.0^{+12.0}_{-8.0}$ km s^{-1} Mpc^{-1}. See figure 6.1 for the full confidence interval. As the number of observed binary neutron star mergers increases, so does their utility. The current binary neutron star merger rate estimate of $R = 1540^{+3200}_{-1220}$Gpc^{-3}yr^{-1} (Abbott et al., 2017b) combined with LIGO currently having a detection horizon of $\sim$190 Mpc (Abbott et al., 2017c) for these events results in an estimated $\sim$44 events observed per year. The interferometers of both the LIGO and Virgo experiments are

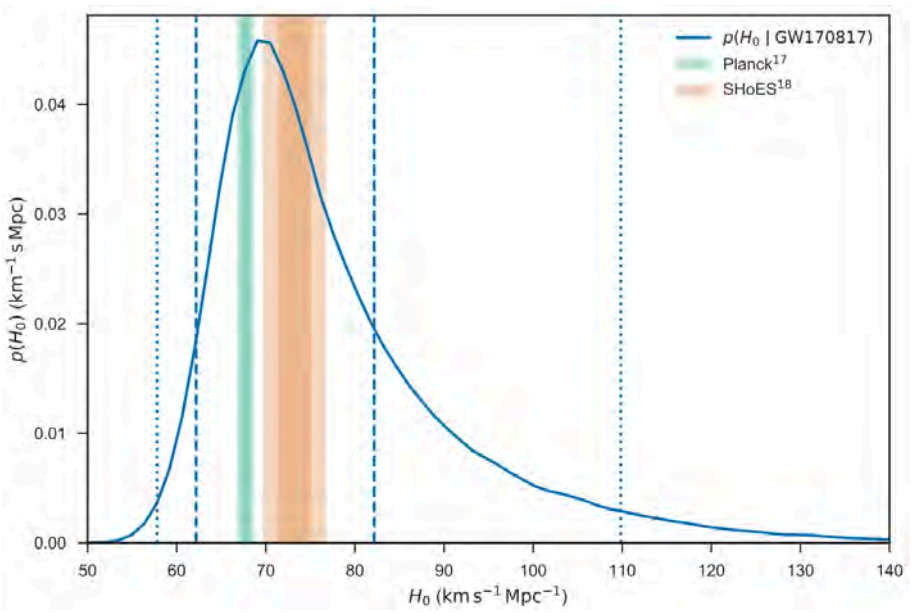

Figure 6.1: Blue curve is the marginalised posterior density for the Hubble constant. 1-σ and 2-σ constraints from the Planck Collboration (Planck Collaboration, 2016) and SHoES (Riess et al., 2016b) are shown as the green and orange shadings respectively. The maximum a posteriori value and 68.3% likelihood interval is $H_0 = 70.0^{+12.0}_{-8.0}$ km s^{-1} Mpc^{-1}. Reproduced from Abbott et al. (2017a).

undergoing continuous upgrades to their sensitivity and additional experiments such as IndIGO in India and KAGRA in Japan will be coming online in the coming years. This will contribute immensely to the ability to localise observed events, observe events at larger distances, and importantly the sheer volume of observed events. There are at least two use cases where binary neutron star mergers can help push type Ia supernova cosmology forward. If a sufficiently large amount of binary neutron star mergers and their optical counterpart are observed it will make it possible to probe the local bulk flow through these observations. These observations will be completely independent of the distance ladder and depend almost exclusively on the assumed model of gravity, typically general relativity. The crucial part here is that a sufficient number of events are observed such that the degeneracy between distance and inclination of the merger event can be broken. Another use case for binary neutron star merger events is as calibration for the absolute luminosity of type Ia supernovae. Calibration is one of the most significant sources of systematic uncertainty. If we can improve the calibration of the absolute magnitude of type Ia supernovae it will therefore have a huge impact on the overall uncertainty of future surveys. Today typically cepheid variable stars are used as calibration. The question becomes how many neutron star merger events need to be observed in galaxies where a type Ia supernovae has also been observed before this becomes a competitive calibration method. Both of these questions are very much open, and depend strongly on the rate estimate which is currently highly uncertain. Whether competitive multi-messenger cosmology arrives in the near or more distant future is currently impossible to say, although it will be an interesting journey regardless of the timeframe.

Resume på Dansk

I de sidste årtier har det faktum at type Ia supernovaer kan bruges som standardlys spillet en central rolle i at bestemme de kosmologiske parametre fra den kosmologiske standardmodel til høj præcision. På trods af den prominente rolle har vi endnu ikke identificeret det underliggende fysiske system som leder til type Ia supernovaer. For at kunne forstå alle systematiske bidrag til den usikkerhed der er associeret med at observere type Ia supernovaer er det nødvendigt at vi er i stand til pålideligt at identificere det fysiske system som har ledt til den på gældende supernova. En måde at begrænse modellerne for disse fysiske systemer er ved at sammenligne den forsinkelse mellem stjernedannelse og supernova eksplosion vi observerer og den forudsagt af forskellige modeller. På den baggrund sammenligner vi to forskellige måder at måle type Ia supernovaraten på og forener dem i en ny model. Vi finder at den nye model er i god overenstemmelse med data og er foretrukket i forhold til den nuværende koncensusmodel. For at modellen kan anvendes i regioner med høj stjernedannelse er det dog nødvendigt med flere observationer i det regime. Type Ia supernovaer kan bruges til at få indsigt i den samlede bevægelse i forhold til den kosmiske baggrundsstråling. Nogle studier har fundet at denne bevægelse er større end hvad der er i overensstemmelse med den kosmologiske standardmodel. Vores studie finder at hvis man tager højde for geometri og hvor komplet volumenet er observeret er denne samlede bevægelse ikke længere i modstrid med den teoretiske model. Supernovaers egenbevægelse kan systematisk påvirke den observerede rødforskydning hvilket igen kan føre til at de udledte kosmologiske parametre kan påvirkes systematisk. Med fokus på de type Ia supernovaer Dark Energy Survey har observeret bestemmes det at den nuværende standard metode for at korrigere for disse effekter er tilstrækkelig også for Dark Energy Survey. Denne korrektion for egenbevægelse skal dog associeres med en hvis usikkerhed da det datasæt som egenbevægelserne tages fra også er usikkert. På baggrund af den success som type Ia supernovaer har haft som standardlys ved lavere rødforskydninger har der været søgt efter et tilsvarende standardlys ved højere rødforskydninger. Vi undersøger derfor den potentielle nytteværdi af disse foreslåede standardlys i forhold til at sortere nogle af de modeller der findes for mørk energi fra. Vi finder at fordi ingen af de undersøgte modeller kan afvige signifikant fra standard kosmologi vil standardlys ved højere rødforskydninger ikke bidrage mere end standardlys ved lavere rødforskydninger. Det inverse argument betyder dog også at hvis et standardlys afviger fra den standard kosmologiske model ved højere rødforskydninger vil det være et problem ikke bare for standardkosmologien, men ogsåfor alle de testede modeller for mørk energi.

Appendices

A ML and MV Bulk Flow Estimators

To compare the measured bulk flow with theoretical predictions, it is necessary to have a method to turn the individually observed peculiar velocities into a bulk flow. In this paper we focus on two estimators, the Maximum Likelihood (ML) and the Minimum Variance (MV) estimators. In the original paper introducing the MV estimator (Watkins et al., 2009) there were a few typographic errors and unexplained terms; for completeness and to help others avoid confusion the procedures used to carry out the ML and MV estimators in this work are explained in this appendix.

Maximum Likelihood

The ML estimator is by far the easiest of the two to implement and is computationally much cheaper than the MV estimator. The result of the ML estimator is a vector containing the velocity components corresponding to each of the three spatial dimensions. Each of the three components is given by a sum over the individual peculiar velocity components multiplied by some weight. The sum has the form

$$u_i = \sum_n w_{i,n} S_n \tag{1}$$

where i is the placeholder for either the x, y, or z index and the sum goes over all n peculiar velocities. S_n is the n'th measured peculiar velocity, $w_{i,n}$ is the associated weight for that peculiar velocity and u_i is the calculated bulk flow where again $i = (x, y, z)$. This equation holds true for both the ML and the MV estimators. Where they differ is how they go about calculating the $w_{i,n}$ weights.

For the ML estimate the weights are given by

$$w_{i,n} = \sum_j \frac{\hat{x}_j \cdot \hat{r}_n}{(\sigma_n^2 + \sigma_\star^2)} A_{ij}^{-1}. \tag{2}$$

The sum is over the $j = (x, y, z)$ components, and $\hat{x}_j \cdot \hat{r}_n$ is the projection of the unit vector $\hat{r}$ pointing from the observer to the galaxy in question. σ_n is the uncertainty on the velocity of the n'th measurement, and $\sigma_\star$ is a constant of order 250 km s^{-1} meant to account for the non-linear

flows on smaller scales. Finally A_{ij}^{-1} is the inverse of matrix A_{ij} given by

$$A_{ij} = \sum_n \frac{(\hat{x}_i \cdot \hat{r}_n)(\hat{x}_j \cdot \hat{r}_n)}{(\sigma_n^2 + \sigma_\star^2)}. \tag{3}$$

In practise when calculating the ML weights the first step is to calculate the A_{ij} matrix, taking advantage of the symmetry $A_{ij} = A_{ji}$. The inverted matrix A_{ij}^{-1} is then computed, and the weights $w_{i,n}$ are calculated. This is a fairly simple process, and is cheap in computation time needed.

Minimum Variance

For the Minimum Variance estimator, first an ideal survey is constructed by generating x,y,z coordinates uniformly randomly in the range $[-4R_I; 4R_I]$ and then drawing points according to the distribution $n(r) \propto r^2 \exp(-r^2/2R_I^2)$. This constructed ideal survey is spherically symmetric and isotropic. It is constructed such that the window function of the MV method is sensitive in the range where we wish to probe the bulk flow, namely on scales of R_I. In order to stay consistent R_I will be set to 50 Mpc h^{-1} in this work, unless otherwise stated. The number of points in the constructed ideal survey is set to 1200 throughout this work. It was found that increasing the number of points in the ideal survey beyond 1200 did not contribute to the stability of the MV method but only served to increase the already considerable computation time.

For readability matrix notation is used so that $w_{i,n}$ becomes column matrix $\mathbf{w}_i$ of n elements. $\mathbf{w}_i$ is computed with

$$\mathbf{w}_i = (\mathbf{G} + \lambda \mathbf{P})^{-1} \mathbf{Q}_i. \tag{4}$$

$\mathbf{G}$ is a symmetric square n by m matrix where n and m correspond to the n'th and m'th measurement. The matrix $\mathbf{G}$ is the covariance matrix for the individual velocities S_n and S_m. In linear theory we can write the matrix elements G_{nm} as a sum of two terms

$$G_{nm} = \langle S_n S_m \rangle \tag{5}$$

$$= \langle v_n v_m \rangle + \delta_{nm}(\sigma_\star^2 + \sigma_n^2). \tag{6}$$

The second term is known as the noise term and is the Kronecker delta function; 0 for $n \neq m$ but $\sigma_\star^2 + \sigma_n^2$ when $n = m$. The first term is the geometry term which is given by

$$\langle v_n v_m \rangle = \frac{\Omega_m^{1.1} H_0^2}{2\pi^2} \int \mathrm{d}k \, P(k) \, f_{mn}(k) \tag{7}$$

where H_0 is the Hubble constant in units[1] of h km s^{-1} Mpc^{-1}, and $\Omega_m^{1.1}$ is the growth of structure parameter $f^2 \approx \Omega_m^{1.1}$. $P(k)$ is the matter power spectrum, which in this work is calculated using COPTER (Carlson et al., 2009; Lewis et al., 2000; Howlett et al., 2012). The function $f_{mn}(k)$ is

[1]Which is always 100, per definition of $h = (H_0/100)$ km s^{-1} Mpc^{-1}.

the angle averaged window function which is explicitly given as

$$f_{mn}(k) = \int \frac{\mathrm{d}^2\hat{k}}{4\pi}(\hat{\mathbf{r}}_n \cdot \hat{\mathbf{k}})(\hat{\mathbf{r}}_m \cdot \hat{\mathbf{k}}) \times \exp[ik\hat{\mathbf{k}} \cdot (\hat{\mathbf{r}}_n - \hat{\mathbf{r}}_m)]. \tag{8}$$

Although Eq. 8 is often quoted in the literature as the function used to calculate $f_{mn}(k)$ it is far from being a practical expression and in reality the expression used is from Ma and Zhang (2011) who showed that we can express the angle averaged window function as

$$f_{mn}(k) = \frac{1}{3}\cos(\alpha(j_0(kA) - 2j_2(kA))) + \frac{1}{A^2}j_2(kA)r_n r_m \sin^2(\alpha) \tag{9}$$

where

$$A = (\, r_n^2 + r_m^2 - 2r_n r_m \cos(\alpha)\,)^{0.5} \tag{10}$$

and α is the angle between the n'th and m'th galaxy given by

$$\alpha = \arccos(\hat{\mathbf{r}}_n \cdot \hat{\mathbf{r}}_m). \tag{11}$$

The $j_0(x)$ and $j_2(x)$ functions are spherical Bessel functions given by

$$j_0(x) = \frac{\sin(x)}{x}\ ,\ j_2(x) = \left(\frac{3}{x^2} - 1\right)\frac{\sin(x)}{x} - \frac{3\cos(x)}{x^2}. \tag{12}$$

Putting all this together gives us the G_{nm} elements. Finding the P_{nm} elements of $\mathbf{P}$ is then fairly simple as it is simply the $k = 0$ limit of f_{nm} which is

$$P_{nm} = \frac{1}{3}\cos(\alpha). \tag{13}$$

The principal idea of the MV method is to minimise the variance between the bulk flow measured by the galaxy survey and the bulk flow that would be measured by an ideal survey. The $\mathbf{G}$ and $\mathbf{P}$ matrices are the components of the weight that take as input the measured data. The last component, the $\mathbf{Q}$ matrix, takes as input the position and peculiar velocities from the galaxies of the constructed ideal survey. It is calculated in much the same way as the G_{nm} elements with the $Q_{i,n}$ elements being given by

$$Q_{i,n} = \sum_{n'=1}^{N'} w'_{i,n'}\langle v_{n'} v_n \rangle \tag{14}$$

and

$$\langle v_{n'} v_n \rangle = \frac{\Omega_m^{1.1} H_0^2}{2\pi^2}\int \mathrm{d}k\, P(k)\, f_{n'n}(k), \tag{15}$$

where $f_{n'n}(k)$ is analogous to Eq. 9 but with the difference that n' and n run over the galaxies in the constructed ideal survey, in contrast to n and m that run over the galaxies from the actual observed galaxies of our survey. The ideal weights $w'_{i,n'}$ will be given by

$$w'_{i,n'} = 3\frac{\hat{\mathbf{x}}_i \cdot \hat{\mathbf{r}}_n}{N_{\mathrm{ideal}}} \tag{16}$$

where $N_{\rm ideal}$ is the total number of galaxies in the constructed ideal survey.

The final step is to solve for the value of λ, which is a Lagrange multiplier inherent from the minimisation process. It enforces the normalisation constraint

$$\sum_m \sum_n w_{i,n} w_{i,m} P_{nm} = \frac{1}{3}. \tag{17}$$

A simple method to solve for λ is to vary λ and calculate the above sum, until a value for λ that makes the above equality true is found.

Calculating the MV bulk flow vector is a rather involved process and is orders of magnitude more expensive computationally than the ML estimator. In this work the analysis is done using mainly the ML estimator, with the MV estimator only being tested in a more limited scenario. If computation time was no concern then the full analysis could be carried out for the MV estimator as well.

The implementation of the MV estimator used in this work is based on that of Dr. Morag Scrimgeour which is available at https://github.com/mscrim/MVBulkFlow.

B Mock Galaxy Surveys versus Dark Matter Halos

As explained in section 3.3 the full HR2 dataset consists of DM halos, not individual galaxies. To test that this does not affect our results, we apply a mock SDSS-III galaxy catalogue produced from the HR2 cosmological DM halo simulation. This mock catalogue lies in a sphere with radius 1 Gpc h^{-1} and origin at (x, y, z) = (1.8, 1.8, 1.8) Gpc h^{-1}. From the full HR2 DM halo simulation we slice a sphere that also has radius 1 Gpc h^{-1} and origin at (x, y, z) = (1.8, 1.8, 1.8) Gpc h^{-1}. The distributions of bulk flow magnitudes using the ML estimator are then calculated for both the SDSS-III mock catalogue and the sliced sphere of DM halos. The distributions are shown in Figure 2 and the most probable and RMS values are shown in Table 1. We see that for the same number of galaxies per bulk flow, n, the distributions look very similar. From Figure 2 and Table 1 we can see that the distributions of bulk flow magnitudes, as well as their most probable values and RMS values, are in good agreement. This shows that it is indeed possible to use the DM halos of the full HR2 simulation to perform our analysis, including investigating the effects of survey geometry on the measurements of bulk flow magnitudes.

C Estimating Peculiar Velocity Measurement Uncertainty

To estimate the peculiar velocity measurement uncertainty, $\sigma_{v,Ia}$, as a function of redshift we follow the approach of Davis et al. (2011). Using the terminology of Davis et al. (2011) the measurement uncertainty is

$$\sigma_{v,Ia} = c \cdot \sigma_z = c \cdot \sigma_\mu \cdot \frac{\ln(10)}{5} \frac{\bar{z}(1 + \bar{z}/2)}{1 + \bar{z}} \tag{18}$$

	SDSSIII Mock	DM Halo
	n : 50 - (180^{+99}_{-83})km s^{-1}	(180^{+99}_{-83})km s^{-1}
	n : 100 - (147^{+79}_{-66})km s^{-1}	(145^{+77}_{-65})km s^{-1}
	n : 500 - (101^{+52}_{-44}) km s^{-1}	(110^{+55}_{-47})km s^{-1}

Table 1: Most probable bulk flow with upper and lower 1-σ bounds for bulk flow magnitude distributions of SDSSIII mock survey galaxy catalogue and DM halo slice of the full HR2 simulation, for varying number of galaxies per bulk flow calculation, n. The numbers should be compared across horizontally. All the numbers are within 0.1 σ of each other, which shows that using DM Halos gives comparable results to using a mock galaxy catalogue.

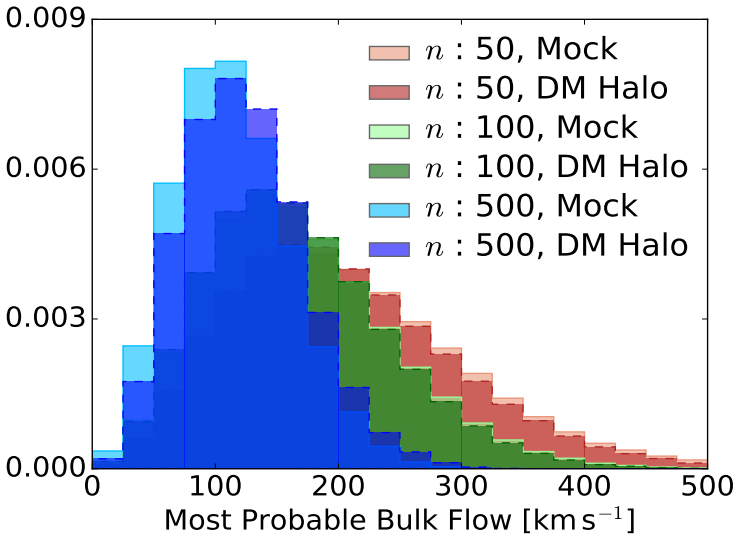

Figure 2: ML bulk flow magnitude distributions for SDSS-III mock galaxy catalogue subsamples and DM halo subsamples, both taken from the same position in the full HR2 simulation. The bulk flow magnitude distributions for the DM halo subsamples are labelled 'DM Halo', with the distributions for the SDSS-III mock catalogue samples labelled 'Mock'. The individual pairs of bulk flow magnitude distributions (e.g. $n = 500$, $n = 100$ and $n = 50$) all show similar behaviour in their bulk flow velocity distributions.

where c is the speed of light in vacuum, $\bar{z}$ is the recession redshift and σ_μ is the uncertainty on the distance modulus measurement. To obtain an estimate for the peculiar velocity measurement uncertainty one has to assume a value for σ_μ, we have chosen to set $\sigma_\mu = 0.1$ throughout this paper, as it is the optimistic value of σ_μ that modern type Ia SNe surveys can achieve, although it is a bit lower than what was possible for legacy surveys where a value of $\sigma_\mu = 0.15$ would be more appropriate. To reiterate the point made in section 3.6, using a larger uncertainty in the peculiar velocity measurements will only increase the variance in each component of the bulk flow vector, and any potential biases. Hence by adopting an optimistic error, we are in fact being conservative in our estimates of potential biases.

D Dark Energy Equation of State Parametrisations

nCPL

When working with a nCPL cosmology ($w(a) = w_0 + w_a(1-a)^n$), the solution to the continuity equation

$$\begin{aligned} \Omega_\Lambda(z) &= \Omega_{\Lambda,0} \exp\left[\int_{a_0}^{a} \frac{-3(1+w_\Lambda(a))}{a} \mathrm{d}a\right] \\ \Omega_\Lambda(z) &= \Omega_{\Lambda,0} f(a) \end{aligned} \tag{19}$$

for the chosen value of n, determines how dark energy evolves with time in the chosen cosmology. Here $f(a)$ is shorthand notation for the function describing the evolution of dark energy with scale factor or redshift. Ω_Λ is the energy density of dark energy normalised with the critical energy density, the subscript 0 indicating the value at the present day. The integral on the right hand side of Eq. 19 is of particular interest, as deriving a general solution would enable directly observing the behaviour of dark energy for the chosen value of n for the nCPL cosmology. Using that in the nCPL cosmology $w_{n\mathrm{CPL}}(a) = w_0 + w_a(1-a)^n$ and substituting gives

$$f(a) = \int_{a_0}^{a} \frac{-3(1+w_0+w_a(1-a)^n)}{a} \mathrm{d}a \tag{20}$$

which has the solution

$$f(a) = -3\left[\frac{w_a(1-a)^n \left(\frac{a-1}{a}\right)^{-n} F(n,a)}{n} + (w_0+1)\log(a)\right] \tag{21}$$

with $F(n,a)$ being a power series from the hypergeometric function ${}_2F_1(-n,-n;1-n;\frac{1}{a})$ and using that $a_0 = 1$.

Although the general solution is rather unpleasant to work with, specific cases where $n = 1,2,3$ can be easily solved. The solution for $n = 1$ is

$$\Omega_\Lambda(a)_{n=1} = \Omega_{\Lambda,0} a^{-3(1+w_0+w_a)} \exp\left(-3w_a(1-a)\right). \tag{22}$$

For $n = 2$

$$\Omega_\Lambda(a)_{n=2} = \Omega_{\Lambda,0} a^{-3(1+w_0+w_a)} \exp\left(-\frac{3}{2} w_a (1-a)(3-a)\right). \tag{23}$$

For $n = 3$

$$\begin{aligned}\Omega_\Lambda(a)_{n=3} =& \Omega_{\Lambda,0} a^{-3(1+w_0+w_a)} \times \\ & \exp\left(-\frac{1}{2} w_a (1-a)(2a^2 - 7a + 11)\right).\end{aligned} \tag{24}$$

Inspired by Pantazis et al. (2016) the solution for the $n = 7$ case is also derived.

$$\begin{aligned}&\Omega_\Lambda(a)_{n=7} = \Omega_{\Lambda,0} a^{-3(1+w_0+w_a)} \exp\left[-\frac{1}{140} w_a (1-a) \times\right. \\ &\left.(60a^6 - 430a^5 + 1334a^4 - 2341a^3 + 2559a^2 - 1851a + 1089)\right].\end{aligned}$$

JBP

Similar to the approach in the previous section the continuity equation for the JBP parametrisation, $w(a)_{\rm JBP} = w_0 + w_a(1-a)a$, is solved yielding

$$\Omega_\Lambda(a)_{\rm JBP} = \Omega_{\Lambda,0} a^{-3(1+w_0)} \exp\left(\frac{3}{2} w_a (1-a)^2\right). \tag{25}$$

E Application of Extreme Value Theorem

When determining the extrema of $\Delta\mu$ in the space of 68% likelihood $(\Omega_{m,0}, w_0, w_a)$ values it is helpful to apply the extreme value theorem to state that extrema do exist, and they exist only on the boundary. First, in order for this argument to hold true, we need to prove that $\frac{\partial \Delta\mu}{\partial \lambda_i} \neq 0$ for all allowed values of one or more of the parameters $\lambda_i \in (\Omega_{m,0}, w_0, w_a)$. For the following math to be as simple as possible, we will focus on the case where $\lambda_i = w_0$. First, we define the needed equations. We simplify $\frac{\partial \Delta\mu}{\partial w_0}$ by noting that

$$\begin{aligned}\frac{\partial \Delta\mu}{\partial w_0} &= \frac{\partial(\mu_{w_z CDM} - \mu_{\Lambda CDM})}{\partial w_0} \\ &= \frac{\partial \mu_{w_z CDM}}{\partial w_0} - \frac{\partial \mu_{\Lambda CDM}}{\partial w_0} \\ &= \frac{\partial \mu_{w_z CDM}}{\partial w_0} - 0 \\ &= \frac{\partial \mu_{w_z CDM}}{\partial w_0} \\ &= \frac{\partial \mu}{\partial w_0}\end{aligned} \tag{26}$$

where for simplicity we defined $\mu = \mu_{w_z CDM}$ in the final line. Following King et al. (2013) the equations needed now are

$$\frac{\partial \mu}{\partial w_0} = \frac{5}{D_M^{'} \ln(10)} \frac{\partial D_M^{'}}{\partial w_0}, \tag{27}$$

where $D_M^{'}$ is the dimensionless tangential comoving distance $D_M^{'} = (H_0/c) D_M$. In the limit where the curvature term Ω_k approaches zero, i.e. a cosmology that is close to flat, this gives

$$\lim_{\Omega_k \to 0} \frac{\partial D_M^{'}}{\partial w_0} = \frac{\partial \chi^{'}}{\partial w_0}, \tag{28}$$

$$\frac{\partial \chi^{'}}{\partial w_0} = -\frac{1}{2} \int_0^z \frac{1}{E(z^{'})^3} \frac{\partial \mathcal{E}(z^{'})}{\partial w_0} \mathrm{d}z^{'}, \tag{29}$$

$$\frac{\partial \mathcal{E}(z)}{\partial w_0} = \Omega_x \frac{\partial f(z)}{\partial w_0}, \tag{30}$$

$$\frac{\partial \mathcal{E}(z)}{\partial w_0} = 3 \Omega_x f(z) \ln(1+z), \tag{31}$$

and finally

$$\mathcal{E}(z) = H(z)^2 / H_0^2 = E(z)^2, \tag{32}$$

$$E(z)^2 = \Omega_{m,0}(1+z)^3 + \Omega_k (1+z)^2 + \Omega_{\Lambda,0} \exp\left(3 \int_0^z [1 + w(z^{'})] \frac{\mathrm{d}z^{'}}{1+z^{'}} \right). \tag{33}$$

If we show that all terms added in the above equations have the same sign, that is they are either positive or negative for all values of z, it follows that they never cancel out and will therefore never sum to zero. Noting that

1. $E(z)$ is for flat cosmologies only ever positive,
2. $f(z) > 0$ for nCPL and JBP parametrisations,
3. and $z > 0$

it follows that $\frac{\partial \Delta\mu}{\partial w_0}$ is only ever negative, if we restrict ourselves to work with flat cosmologies. Applying the extreme value theorem, it is apparent that there are no critical points, so the extreme values of $\Delta\mu$ exist on the boundary. This argument reduces the dimensionality of the problem by one from three to two, saving a large amount of computation time in searching for the extreme values of $\Delta\mu$.

F Data Analysis

In this work CosmoMC (Lewis and Bridle, 2002; Lewis, 2013), utilising CAMB (Lewis et al., 2000; Howlett et al., 2012), PICO (Fendt and Wandelt, 2006), and CMBFAST (Seljak and Zaldarriaga, 1996; Zaldarriaga et al., 1998) was used extensively. The datasets used include observations of the cosmic microwave background from the Planck Collaboration (Ade et al., 2016; Planck

Collaboration, 2015; Adam et al., 2016) and BICEP-Planck (Ade et al., 2015), observations of baryon acoustic oscillations from SDSS-III (Anderson et al., 2014a), 6dF (Beutler et al., 2011), MGS (Blake et al., 2011; Padmanabhan et al., 2012; Anderson et al., 2014b; Ross et al., 2015) as well as supernova data from the Joint Light-Curve Analysis (Betoule et al., 2014b). For analysis of the output chains of CosmoMC this work made use of Astropy, a community-developed core Python package for Astronomy (Astropy Collaboration, 2013). For details on how the output chains of CosmoMC were analysed and plots of the results were produced see the GitHub repository at `https://github.com/per-andersen/Deltamu`.

G Additional Plots

In Fig. 3 plots analogous to panels (a) and (b) of Fig. 5.2 are shown for the JBP, $n3$CPL, and $n7$CPL models. First, in panel (a), (c), and (e) it is shown that the largest contribution to the extrema of $\Delta\mu$ comes from the uncertainty in $\Omega_{m,0}$, rather than the choice of dark energy model and uncertainty in w_0 and w_a, just like for the CPL model. In panels (b), (d), and (f) the effect of K on the JBP, $n3$CPL, and $n7$CPL models is shown to be similar to that on the $\Delta\mu$ of the CPL model; not including K removes the scatter around $z = 0$ and widens the distribution of $\Delta\mu$ somewhat, increasing the extrema of $\Delta\mu$ at high redshifts.

H Additional Fitting Details

As discussed in the main body of this work we apply a grid method to derive maximum likelihood parameters for the models introduced in this work. Grid methods are typically computationally expensive, with the computational workload quickly increasing with the number of dimensions. In our case, the maximum number of free parameters to fit in one model is four, which is the regime where MCMC methods such as EMCEE can be substantially cheaper computationally than grid methods. The MCMC approach was however found to be unsuitable, due to many local extrema effecting the marginalised likelihoods. The one dimensional marginalised likelihoods could for one parameter have a maximum at the global maximum likelihood while for others have a maximum at some value not near the global maximum likelihood region. This also meant that while the likelihood grid was utilised to find the maximum likelihood fit, it suffers from the same issues as the MCMC approach when used to estimate uncertainties. Therefore a bootstrapping approach was attempted. In this approach the the data is resampled with replacement and then refit multiple times, to derive distributions for all parameters from which uncertainties can be estimated. This proved to be computationally too expensive, as for each resampling of the data the grid method had to be rerun. Finally the Fisher matrix method was used to estimate uncertainties. First the Fisher matrix method was applied to the A+B model, which yielded uncertainties in agreement with those of the MCMC method to within 1%. The Fisher matrix method was then used to estimate uncertainties for the piecewise model and the smooth logarithm parametrisation, respectively.

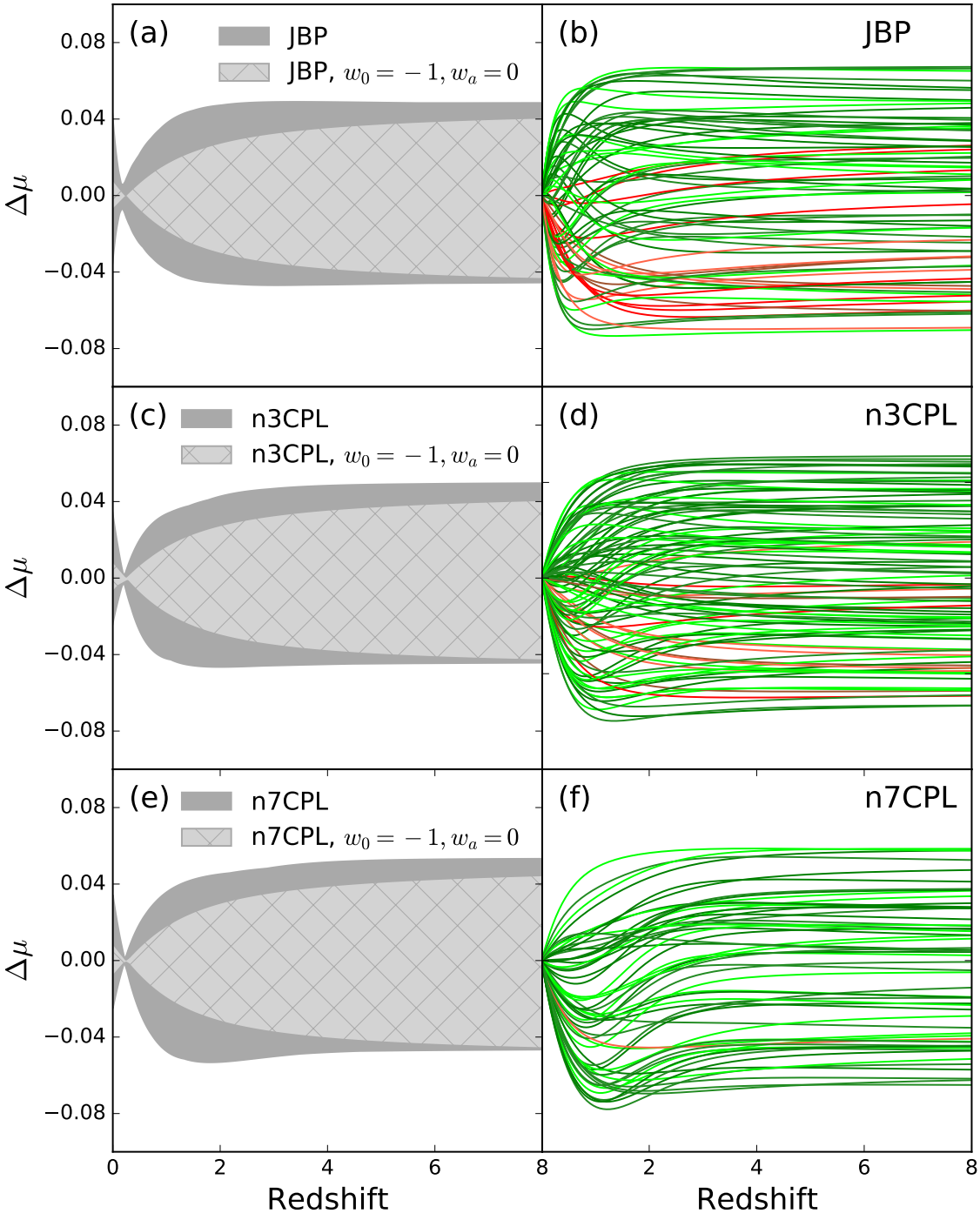

Figure 3: Plots analogous to panels (a) and (b) of Fig. 5.2, but instead of the CPL model for the JBP, $n3$CPL, and $n7$CPL models.

Bibliography

M. Aaronson, J. Huchra, J. Mould, P. L. Schechter, and R. B. Tully. The velocity field in the local supercluster. *The Astrophysical Journal*, 258:64, jul 1982. ISSN 0004-637X. doi: 10.1086/160053.

Alexandra Abate and Hume A. Feldman. Detected fluctuations in Sloan Digital Sky Survey luminous red galaxy magnitudes: bulk flow signature or systematic? *Monthly Notices of the Royal Astronomical Society*, 419(4):3482–3490, feb 2012. ISSN 00358711. doi: 10.1111/j.1365-2966.2011.19988.x.

B. P. Abbott, R. Abbott, T. D. Abbott, et al. A gravitational-wave standard siren measurement of the Hubble constant. *Nature*, 551(7678):85, oct 2017a. ISSN 0028-0836. doi: 10.1038/nature24471.

B. P. Abbott, R. Abbott, T. D. Abbott, et al. GW170817: Observation of Gravitational Waves from a Binary Neutron Star Inspiral. *Physical Review Letters*, 119(16):161101, oct 2017b. ISSN 0031-9007. doi: 10.1103/PhysRevLett.119.161101.

B. P. Abbott, R. Abbott, T. D. Abbott, et al. Multi-messenger Observations of a Binary Neutron Star Merger. *The Astrophysical Journal*, 848(2):L12, oct 2017c. ISSN 2041-8213. doi: 10.3847/2041-8213/aa91c9.

R. Adam, P. A. R. Ade, N. Aghanim, et al. Planck 2015 results. *Astronomy & Astrophysics*, 594:A8, oct 2016. ISSN 0004-6361. doi: 10.1051/0004-6361/201525820.

Caitlin Adams and Chris Blake. Improving constraints on the growth rate of structure by modelling the density–velocity cross-correlation in the 6dF Galaxy Survey. *Monthly Notices of the Royal Astronomical Society*, 471(1):839–856, oct 2017. ISSN 0035-8711. doi: 10.1093/mnras/stx1529.

P. A. R. Ade, N. Aghanim, Z. Ahmed, et al. Joint Analysis of BICEP2/Keck Array and Planck Data. *Physical Review Letters*, 114(10):1–17, feb 2015. ISSN 10797114. doi: 10.1103/PhysRevLett.114.101301.

P. A. R. Ade, N. Aghanim, M. Arnaud, et al. Planck 2015 results. *Astronomy & Astrophysics*, 594:A13, oct 2016. ISSN 0004-6361. doi: 10.1051/0004-6361/201525830.

Andreas Albrecht, Gary Bernstein, Robert Cahn, et al. Report of the Dark Energy Task Force. *arXiv:0609591*, astro-ph:9591, sep 2006.

Greg Aldering, Alex G. Kim, Marek Kowalski, Eric V. Linder, and Saul Perlmutter. Snapping supernovae at z $>$ 1.7. *Astroparticle Physics*, 27(2-3):213–225, jul 2007. ISSN 09276505. doi: 10.1016/j.astropartphys.2006.11.001.

L. Amati, D. S. Sawant, and M. Della Valle. *GRB Cosmology through the Ep,i-intensity correlation*, volume 29. Gordon and Breach Science Publishers, 2016.

Lauren Anderson, Eric Aubourg, Stephen Bailey, et al. The clustering of galaxies in the SDSS-III baryon oscillation spectroscopic survey: Baryon acoustic oscillations in the data releases 10 and 11 galaxy samples. *Monthly Notices of the Royal Astronomical Society*, 441(1):24–62, dec 2014a. ISSN 13652966. doi: 10.1093/mnras/stu523.

Lauren Anderson, Eric Aubourg, Stephen Bailey, et al. The clustering of galaxies in the sdss-iii baryon oscillation spectroscopic survey: Measuring DA and H at z = 0.57 from the baryon acoustic peak in the data release 9 spectroscopic galaxy sample. *Monthly Notices of the Royal Astronomical Society*, 439(1):83–101, mar 2014b. ISSN 00358711. doi: 10.1093/mnras/stt2206.

Astropy Collaboration. Astropy: A community Python package for astronomy. *Astronomy & Astrophysics*, 558:A33, jul 2013. ISSN 0004-6361. doi: 10.1051/0004-6361/201322068.

Edésio M Barboza and J.S. Alcaniz. Probing the time dependence of dark energy. *Journal of Cosmology and Astroparticle Physics*, 2012(02):042–042, feb 2012. ISSN 1475-7516. doi: 10.1088/1475-7516/2012/02/042.

Peter S. Behroozi, Risa H. Wechsler, and Charlie Conroy. THE AVERAGE STAR FORMATION HISTORIES OF GALAXIES IN DARK MATTER HALOS FROM z = 0-8. *The Astrophysical Journal*, 770(1):57, may 2013. ISSN 0004-637X. doi: 10.1088/0004-637X/770/1/57.

Eric Bellm and Shrinivas Kulkarni. The unblinking eye on the sky. *Nature Astronomy*, 1(3):0071, mar 2017. ISSN 2397-3366. doi: 10.1038/s41550-017-0071.

M. Betoule, R. Kessler, J. Guy, et al. Improved cosmological constraints from a joint analysis of the SDSS-II and SNLS supernova samples. *Astronomy & Astrophysics*, 568:A22, aug 2014a. ISSN 0004-6361. doi: 10.1051/0004-6361/201423413.

M. Betoule, R. Kessler, J. Guy, et al. Improved cosmological constraints from a joint analysis of the SDSS-II and SNLS supernova samples. *Astronomy & Astrophysics*, 568:A22, jan 2014b. ISSN 0004-6361. doi: 10.1051/0004-6361/201423413.

Florian Beutler, Chris Blake, Matthew Colless, et al. The 6dF Galaxy Survey: Baryon acoustic oscillations and the local Hubble constant. *Monthly Notices of the Royal Astronomical Society*, 416(4):3017–3032, 2011. ISSN 00358711. doi: 10.1111/j.1365-2966.2011.19250.x.

Chris Blake, Eyal A. Kazin, Florian Beutler, et al. The WiggleZ Dark Energy Survey: Mapping the distance-redshift relation with baryon acoustic oscillations. *Monthly Notices of the Royal Astronomical Society*, 418(3):1707–1724, aug 2011. ISSN 00358711. doi: 10.1111/j.1365-2966.2011.19592.x.

M. T. Botticella, E. Cappellaro, L. Greggio, et al. Supernova rates from the SUDARE VST-Omegacam search II. Rates in a galaxy sample. *Astronomy & Astrophysics*, 598:A50, feb 2017. ISSN 0004-6361. doi: 10.1051/0004-6361/201629432.

M. C. P. Bours, S. Toonen, and G. Nelemans. Single degenerate supernova type Ia progenitors. *Astronomy & Astrophysics*, 552:A24, apr 2013. ISSN 0004-6361. doi: 10.1051/0004-6361/201220692.

David Branch. TYPE Ia SUPERNOVAE AND THE HUBBLE CONSTANT. *Annual Review of Astronomy and Astrophysics*, 36(1):17–55, sep 1998. ISSN 0066-4146. doi: 10.1146/annurev.astro.36.1.17.

H.˜A. Buchdahl. Non-linear Lagrangians and cosmological theory. *Monthly Notices of the Royal Astronomical Society*, 150(1):1, sep 1970. ISSN 0035-8711. doi: 10.1093/mnras/150.1.1.

R. R. Caldwell, Rahul Dave, and Paul J. Steinhardt. Cosmological Imprint of an Energy Component with General Equation of State. *Physical Review Letters*, 80(8):1582–1585, feb 1997. ISSN 0031-9007. doi: 10.1103/PhysRevLett.80.1582.

Z. Cano. Gamma-Ray Burst Supernovae As Standardizable Candles. *The Astrophysical Journal*, 794(2):121, oct 2014. ISSN 1538-4357. doi: 10.1088/0004-637X/794/2/121.

E. Cappellaro, R. Evans, and M. Turatto. A new determination of supernova rates and a comparison with indicators for galactic star formation. *Astron. Astrophys.*, 351:459–466, apr 1999. ISSN 0004-6361.

Jordan Carlson, Martin White, and Nikhil Padmanabhan. Critical look at cosmological perturbation theory techniques. *Physical Review D*, 80(4):043531, aug 2009. ISSN 1550-7998. doi: 10.1103/PhysRevD.80.043531.

Jonathan Carrick, Stephen J. Turnbull, Guilhem Lavaux, and Michael J. Hudson. Cosmological parameters from the comparison of peculiar velocities with predictions from the 2M++ density field. *Monthly Notices of the Royal Astronomical Society*, 450(1):317–332, jun 2015. ISSN 0035-8711. doi: 10.1093/mnras/stv547.

M. Chevallier and D. Polarski. Accelerating Universes with Scaling Dark Matter. *International Journal of Modern Physics D, Volume 10, Issue 02, pp. 213-223 (2001).*, 10:213–223, sep 2000. ISSN 0218-2718. doi: 10.1142/S0218271801000822.

Takeshi Chiba. Slow-roll thawing quintessence. *Physical Review D - Particles, Fields, Gravitation and Cosmology*, 79(8):083517, apr 2009. ISSN 15507998. doi: 10.1103/PhysRevD.79.083517.

Peter Coles and Francesco. Lucchin. *Cosmology The origin and evolution of cosmic structure*, volume 53. John Wiley, 2013. ISBN 9788578110796. doi: 10.1017/CBO9781107415324.004.

Jacques Colin, Roya Mohayaee, Subir Sarkar, and Arman Shafieloo. Probing the anisotropic local Universe and beyond with SNe Ia data. *Monthly Notices of the Royal Astronomical Society*, 414 (1):264–271, jun 2011. ISSN 00358711. doi: 10.1111/j.1365-2966.2011.18402.x.

A. Conley, J. Guy, M. Sullivan, et al. SUPERNOVA CONSTRAINTS AND SYSTEMATIC UNCERTAINTIES FROM THE FIRST THREE YEARS OF THE SUPERNOVA LEGACY SURVEY. *The Astrophysical Journal Supplement Series*, 192(1):1, jan 2011. ISSN 0067-0049. doi: 10.1088/0067-0049/192/1/1.

Asantha R. Cooray and Dragan Huterer. Gravitational Lensing as a Probe of Quintessence. *The Astrophysical Journal*, 513(2):L95–L98, mar 1999. ISSN 0004637X. doi: 10.1086/311927.

Stéphane Courteau, Michele Cappellari, Roelof S. de Jong, et al. Galaxy masses. *Reviews of Modern Physics*, 86(1):47–119, jan 2014. ISSN 0034-6861. doi: 10.1103/RevModPhys.86.47.

Martín Crocce and Román Scoccimarro. Renormalized cosmological perturbation theory. *Physical Review D*, 73(6):063519, mar 2006. ISSN 1550-7998. doi: 10.1103/PhysRevD.73.063519.

De-Chang Dai, William H Kinney, and Dejan Stojkovic. Measuring the cosmological bulk flow using the peculiar velocities of supernovae. *Journal of Cosmology and Astroparticle Physics*, 2011(04):015–015, apr 2011. ISSN 1475-7516. doi: 10.1088/1475-7516/2011/04/015.

Tamara M Davis, Lam Hui, Joshua A Frieman, et al. THE EFFECT OF PECULIAR VELOCITIES ON SUPERNOVA COSMOLOGY. *The Astrophysical Journal*, 741(1):67, nov 2011. ISSN 0004-637X. doi: 10.1088/0004-637X/741/1/67.

Marek Demianski, Ester Piedipalumbo, Disha Sawant, and Lorenzo Amati. High redshift constraints on dark energy models from the $E_{p,i}$ – E_{iso} correlation in GRBs. *arXiv:1802.01694*, feb 2018.

Suhail Dhawan, Ariel Goobar, Edvard Mörtsell, Rahman Amanullah, and Ulrich Feindt. Narrowing down the possible explanations of cosmic acceleration with geometric probes. *Journal of Cosmology and Astroparticle Physics*, 2017(07):040–040, jul 2017. ISSN 1475-7516. doi: 10.1088/1475-7516/2017/07/040.

Benedikt Diemer, Martin Sparre, Louis E. Abramson, and Paul Torrey. Log-normal Star Formation Histories in Simulated and Observed Galaxies. *The Astrophysical Journal*, 839(1):26, apr 2017. ISSN 1538-4357. doi: 10.3847/1538-4357/aa68e5.

Albert Einstein. Kosmologische Betrachtungen zur allgemeinen Relativitätstheorie. *Die Naturwissenschaften*, 7(14):232–232, apr 1917. ISSN 0028-1042. doi: 10.1007/BF01591613.

Daniel J. Eisenstein, David H. Weinberg, Eric Agol, et al. SDSS-III: MASSIVE SPECTROSCOPIC SURVEYS OF THE DISTANT UNIVERSE, THE MILKY WAY, AND EXTRA-SOLAR PLANETARY SYSTEMS. *The Astronomical Journal*, 142(3):72, sep 2011. ISSN 0004-6256. doi: 10.1088/0004-6256/142/3/72.

U. Feindt, M. Kerschhaggl, M. Kowalski, et al. Measuring cosmic bulk flows with Type Ia supernovae from the Nearby Supernova Factory. *Astronomy & Astrophysics*, 560:A90, dec 2013. ISSN 0004-6361. doi: 10.1051/0004-6361/201321880.

Martin Feix, Adi Nusser, and Enzo Branchini. Tracing the cosmic velocity field at z 0.1 from galaxy luminosities in the SDSS DR7. *Journal of Cosmology and Astroparticle Physics*, 2014 (09):019–019, sep 2014. ISSN 1475-7516. doi: 10.1088/1475-7516/2014/09/019.

Hume A. Feldman, Richard Watkins, and Michael J. Hudson. Cosmic flows on 100 Mpc scales: standardized minimum variance bulk flow, shear and octupole moments. *Monthly Notices of the Royal Astronomical Society*, 407(4):2328–2338, jul 2010. ISSN 00358711. doi: 10.1111/j.1365-2966.2010.17052.x.

William A. Fendt and Benjamin D. Wandelt. Pico: Parameters for the Impatient Cosmologist. *The Astrophysical Journal*, 654(1):9, jun 2006. ISSN 0004-637X. doi: 10.1086/508342.

Chao-Jun Feng, Xian-Yong Shen, Ping Li, and Xin-Zhou Li. A new class of parametrization for dark energy without divergence. *Journal of Cosmology and Astroparticle Physics*, 2012(09): 023–023, sep 2012. ISSN 1475-7516. doi: 10.1088/1475-7516/2012/09/023.

Lei Feng, Tan Lu, A.G. Riess et Al., et al. A new equation of state for dark energy model. *Journal of Cosmology and Astroparticle Physics*, 2011(11):034–034, nov 2011. ISSN 1475-7516. doi: 10.1088/1475-7516/2011/11/034.

M. Fink, F. K. Röpke, W. Hillebrandt, et al. Double-detonation sub-Chandrasekhar supernovae: can minimum helium shell masses detonate the core? *Astronomy and Astrophysics*, 514:A53, may 2010. ISSN 0004-6361. doi: 10.1051/0004-6361/200913892.

Daniel Foreman-Mackey, David W. Hogg, Dustin Lang, and Jonathan Goodman. emcee : The MCMC Hammer. *Publications of the Astronomical Society of the Pacific*, 125(925):306–312, mar 2013. ISSN 00046280. doi: 10.1086/670067.

Joshua A. Frieman, Bruce Bassett, Andrew Becker, et al. The Sloan Digital Sky Survey-II Supernova Survey: Technical summary. *Astronomical Journal*, 135(1):338–347, jan 2008. ISSN 0004-6256. doi: 10.1088/0004-6256/135/1/338.

Yan Gao and Chris J. Pritchet. Correlations between SNe Ia Rates and Host Galaxy Properties. *The Astronomical Journal*, 145:83, jan 2013. doi: 10.1088/0004-6256/145/3/83.

Shy Genel, Mark Vogelsberger, Volker Springel, et al. Introducing the Illustris project: the evolution of galaxy populations across cosmic time. *Monthly Notices of the Royal Astronomical Society*, 445(1):175–200, nov 2014. ISSN 0035-8711. doi: 10.1093/mnras/stu1654.

M. Goliath, R. Amanullah, P. Astier, A. Goobar, and R. Pain. Supernovae and the nature of the dark energy. *Astronomy and Astrophysics*, 380(1):6–18, dec 2001. ISSN 0004-6361. doi: 10.1051/0004-6361:20011398.

O. Graur, S. A. Rodney, D. Maoz, et al. TYPE-Ia SUPERNOVA RATES TO REDSHIFT 2.4 FROM CLASH: THE CLUSTER LENSING AND SUPERNOVA SURVEY WITH HUBBLE. *The Astrophysical Journal*, 783(1):28, feb 2014. ISSN 0004-637X. doi: 10.1088/0004-637X/783/1/28.

Or Graur, Federica B. Bianco, and Maryam Modjaz. A unified explanation for the supernova rate-galaxy mass dependence based on supernovae detected in Sloan galaxy spectra. *Monthly Notices of the Royal Astronomical Society*, 450(1):905–925, apr 2015a. ISSN 0035-8711. doi: 10.1093/mnras/stv713.

Or Graur, Federica B. Bianco, and Maryam Modjaz. A unified explanation for the supernova rate-galaxy mass dependence based on supernovae detected in Sloan galaxy spectra. *Monthly Notices of the Royal Astronomical Society*, 450(1):905–925, apr 2015b. ISSN 0035-8711. doi: 10.1093/mnras/stv713.

Gaveshna Gupta, Raghavan Rangarajan, and Anjan A. Sen. Thawing quintessence from the inflationary epoch to today. *Physical Review D - Particles, Fields, Gravitation and Cosmology*, 92 (12):123003, dec 2015. ISSN 15502368. doi: 10.1103/PhysRevD.92.123003.

J. Guy, P. Astier, S. Nobili, N. Regnault, and R. Pain. SALT: a spectral adaptive light curve template for type Ia supernovae. *Astronomy & Astrophysics*, 443(3):781–791, dec 2005. ISSN 0004-6361. doi: 10.1051/0004-6361:20053025.

J. Guy, P. Astier, S. Baumont, et al. SALT2: using distant supernovae to improve the use of type Ia supernovae as distance indicators. *Astronomy & Astrophysics*, 466(1):11–21, apr 2007. ISSN 0004-6361. doi: 10.1051/0004-6361:20066930.

A. A. Hakobyan, A. G. Karapetyan, L. V. Barkhudaryan, et al. Supernovae and their host galaxies – III. The impact of bars and bulges on the radial distribution of supernovae in disc galaxies. *Monthly Notices of the Royal Astronomical Society*, 456(3):2848–2860, mar 2016. ISSN 0035-8711. doi: 10.1093/mnras/stv2853.

Adrian S. Hamers, Onno R. Pols, Joke S. W. Claeys, and Gijs Nelemans. Population synthesis of triple systems in the context of mergers of carbon–oxygen white dwarfs. *Monthly Notices of the Royal Astronomical Society*, 430(3):2262–2280, apr 2013. ISSN 1365-2966. doi: 10.1093/mnras/stt046.

Troels Haugbolle, Steen Hannestad, Bjarne Thomsen, et al. The Velocity Field of the Local Universe from Measurements of Type Ia Supernovae. *The Astrophysical Journal*, 661(2):650–659, jun 2007. ISSN 0004-637X. doi: 10.1086/513600.

Malcolm Hicken, W. Michael Wood-Vasey, Stephane Blondin, et al. IMPROVED DARK ENERGY CONSTRAINTS FROM ˜100 NEW CfA SUPERNOVA TYPE Ia LIGHT CURVES. *The Astrophysical Journal*, 700(2):1097–1140, aug 2009. ISSN 0004-637X. doi: 10.1088/0004-637X/700/2/1097.

W. Hillebrandt, M. Kromer, F. K. Röpke, and A. J. Ruiter. Towards an understanding of Type Ia supernovae from a synthesis of theory and observations. *Frontiers of Physics*, 8(2):116–143, apr 2013. ISSN 2095-0462. doi: 10.1007/s11467-013-0303-2.

Wolfgang Hillebrandt and Jens C. Niemeyer. Type Ia Supernova Explosion Models. *Annual Review of Astronomy and Astrophysics*, 38(1):191–230, sep 2000. ISSN 0066-4146. doi: 10.1146/annurev.astro.38.1.191.

Samuel Hinton. ChainConsumer. *The Journal of Open Source Software*, 1(4), aug 2016. doi: 10.21105/joss.00045.

Daniel E. Holz and Eric V. Linder. Safety in Numbers: Gravitational Lensing Degradation of the Luminosity Distance–Redshift Relation. *The Astrophysical Journal*, 631(2):678–688, oct 2005. ISSN 0004-637X. doi: 10.1086/432085.

Tao Hong, Christopher M. Springob, Lister Staveley-Smith, et al. 2MTF – IV. A bulk flow measurement of the local Universe. *Monthly Notices of the Royal Astronomical Society*, 445(1):402–413, nov 2014. ISSN 0035-8711. doi: 10.1093/mnras/stu1774.

S. F. Hönig, D. Watson, M. Kishimoto, et al. Cosmology with AGN dust time lags–simulating the new VEILS survey. *Monthly Notices of the Royal Astronomical Society*, 464(2):1693–1703, jan 2017. ISSN 0035-8711. doi: 10.1093/mnras/stw2484.

Cullan Howlett, Antony Lewis, Alex Hall, and Anthony Challinor. CMB power spectrum parameter degeneracies in the era of precision cosmology. *Journal of Cosmology and Astroparticle Physics*, 2012(04):027–027, apr 2012. ISSN 1475-7516. doi: 10.1088/1475-7516/2012/04/027.

E. Hubble. A relation between distance and radial velocity among extra-galactic nebulae. *Proceedings of the National Academy of Sciences*, 15(3):168–173, mar 1929. ISSN 0027-8424. doi: 10.1073/pnas.15.3.168.

Dragan Huterer, Daniel L. Shafer, and Fabian Schmidt. No evidence for bulk velocity from type Ia supernovae. *Journal of Cosmology and Astroparticle Physics*, 2015(12):033–033, dec 2015. ISSN 1475-7516. doi: 10.1088/1475-7516/2015/12/033.

Cosimo Inserra and Stephen J. Smartt. Superluminous Supernovae As Standardizable Candles and High-Redshift Distance Probes. *The Astrophysical Journal*, 796(2):87, sep 2014. ISSN 1538-4357. doi: 10.1088/0004-637X/796/2/87.

George H. Jacoby, David Branch, Robin Clardullo, et al. A critical review of selected techniques for measuring extragalactic distances. *Publications of the Astronomical Society of the Pacific*, 104:599, aug 1992. ISSN 0004-6280. doi: 10.1086/133035.

H. K. Jassal, J. S. Bagla, and T. Padmanabhan. WMAP constraints on low redshift evolution of dark energy. *Monthly Notices of the Royal Astronomical Society: Letters, Volume 356, Issue 1, pp. L11-L16.*, 356:L11–L16, apr 2004. ISSN 0035-8711. doi: 10.1111/j.1745-3933.2005.08577.x.

Elise Jennings. An improved model for the non-linear velocity power spectrum. *Monthly Notices of the Royal Astronomical Society: Letters*, 427:no–no, sep 2012. ISSN 17453925. doi: 10.1111/j.1745-3933.2012.01338.x.

Saurabh Jha, Adam G. Riess, and Robert P. Kirshner. Improved Distances to Type Ia Supernovae with Multicolor Light-Curve Shapes: MLCS2k2. *The Astrophysical Journal*, 659(1):122–148, apr 2007. ISSN 0004-637X. doi: 10.1086/512054.

Austin Joyce, Lucas Lombriser, and Fabian Schmidt. Dark Energy Versus Modified Gravity. *Annual Review of Nuclear and Particle Science*, 66(1):95–122, oct 2016. ISSN 0163-8998. doi: 10.1146/annurev-nucl-102115-044553.

A. Kashlinsky, F. Atrio-Barandela, D. Kocevski, and H. Ebeling. A Measurement of Large-Scale Peculiar Velocities of Clusters of Galaxies: Results and Cosmological Implications. *The Astrophysical Journal*, 686(2):L49–L52, oct 2008. ISSN 0004-637X. doi: 10.1086/592947.

ShiAnne Kattner, Douglas C. Leonard, Christopher R. Burns, et al. The Standardizability of Type Ia Supernovae in the Near-Infrared: Evidence for a Peak-Luminosity Versus Decline-Rate Relation in the Near-Infrared. *Publications of the Astronomical Society of the Pacific*, 124(912):114–127, feb 2012. ISSN 00046280. doi: 10.1086/664734.

Patrick L. Kelly, Malcolm Hicken, David L. Burke, Kaisey S. Mandel, and Robert P. Kirshner. HUBBLE RESIDUALS OF NEARBY TYPE Ia SUPERNOVAE ARE CORRELATED WITH HOST GALAXY MASSES. *The Astrophysical Journal*, 715(2):743–756, jun 2010. ISSN 0004-637X. doi: 10.1088/0004-637X/715/2/743.

Ju-Han Kim, Chang-Bom Park, Graziano Rossi, Sang-Min Lee, and J. Richard III Gott. THE NEW HORIZON RUN COSMOLOGICAL N-BODY SIMULATIONS. *Journal of The Korean Astronomical Society*, 44(6):217–234, dec 2011. ISSN 1225-4614. doi: 10.5303/JKAS.2011.44.6.217.

A. L. King, T. M. Davis, K. Denney, M. Vestergaard, and D. Watson. High Redshift Standard Candles: Predicted Cosmological Constraints. *Monthly Notices of the Royal Astronomical Society, Volume 441, Issue 4, p.3454-3476*, 441:3454–3476, nov 2013. ISSN 0035-8711. doi: 10.1093/mnras/stu793.

Anthea L. King, Tamara M. Davis, K. D. Denney, M. Vestergaard, and D. Watson. High-redshift standard candles: predicted cosmological constraints. *Monthly Notices of the Royal Astronomical Society*, 441(4):3454–3476, jun 2014. ISSN 0035-8711. doi: 10.1093/mnras/stu793.

E. Komatsu, J. Dunkley, M. R. Nolta, et al. FIVE-YEAR WILKINSON MICROWAVE ANISOTROPY PROBE OBSERVATIONS: COSMOLOGICAL INTERPRETATION. *The Astrophysical Journal Supplement Series*, 180(2):330–376, feb 2009. ISSN 0067-0049. doi: 10.1088/0067-0049/180/2/330.

Guilhem Lavaux, Niayesh Afshordi, and Michael J. Hudson. First measurement of the bulk flow of nearby galaxies using the cosmic microwave background. *Monthly Notices of the Royal Astronomical Society*, 430(3):1617–1635, apr 2013. ISSN 0035-8711. doi: 10.1093/mnras/sts698.

Ruth Lazkoz, Vincenzo Salzano, and Irene Sendra. Oscillations in the dark energy equation of state: New MCMC lessons. *Physics Letters B*, 694(3):198–208, nov 2010. ISSN 03702693. doi: 10.1016/j.physletb.2010.10.002.

Nathan W. C. Leigh and Aaron M. Geller. The dynamical significance of triple star systems in star clusters. *Monthly Notices of the Royal Astronomical Society*, 432(3):2474–2479, jul 2013. ISSN 1365-2966. doi: 10.1093/mnras/stt617.

Claus Leitherer, Daniel Schaerer, Jeffrey D. Goldader, et al. Starburst99: Synthesis Models for Galaxies with Active Star Formation. *The Astrophysical Journal Supplement Series*, 123(1):3–40, jul 1999. ISSN 0067-0049. doi: 10.1086/313233.

Antony Lewis. Efficient sampling of fast and slow cosmological parameters. *Physical Review D*, 87(10):103529, may 2013. ISSN 1550-7998. doi: 10.1103/PhysRevD.87.103529.

Antony Lewis and Sarah Bridle. Cosmological parameters from CMB and other data: A Monte Carlo approach. *Physical Review D*, 66(10):103511, nov 2002. ISSN 05562821. doi: 10.1103/PhysRevD.66.103511.

Antony Lewis, Anthony Challinor, and Anthony Lasenby. EFFICIENT COMPUTATION OF COSMIC MICROWAVE BACKGROUND ANISOTROPIES IN CLOSED FRIEDMANN-ROBERTSON-WALKER MODELS. *THE ASTROPHYSICAL JOURNAL*, 538(2):473–476, aug 2000. ISSN 0004-637X. doi: 10.1086/309179.

Ming Li, Jun Pan, Liang Gao, et al. BULK FLOW OF HALOS IN ΛCDM SIMULATION. *The Astrophysical Journal*, 761(2):151, dec 2012. ISSN 0004-637X. doi: 10.1088/0004-637X/761/2/151.

Xue Li, Jens Hjorth, and Radosław Wojtak. Cosmological Parameters From Supernovae Associated With Gamma-Ray Bursts. *The Astrophysical Journal*, 796(1):L4, sep 2014. ISSN 2041-8213. doi: 10.1088/2041-8205/796/1/L4.

Eric V. Linder. Exploring the Expansion History of the Universe. *Phys.Rev.Lett.*, 90(9):91301, aug 2003. ISSN 0031-9007. doi: 10.1063/1.1543500.

Eric V. Linder. Lambda Is coming: Parametrizing freezing fields. *Astroparticle Physics*, 91:11–14, may 2017. ISSN 09276505. doi: 10.1016/j.astropartphys.2017.02.008.

Dongdong Liu, Bo Wang, and Zhanwen Han. The double-degenerate model for the progenitors of Type Ia supernovae. *Monthly Notices of the Royal Astronomical Society*, 473(4):5352–5361, feb 2017. ISSN 0035-8711. doi: 10.1093/mnras/stx2756.

Mario Livio and Paolo Mazzali. On the Progenitors of Type Ia Supernovae. *arXiv:1802.03125v1*, 7(S281):303, feb 2011.

Mario Livio and Adam G. Riess. Have the Elusive Progenitors of Type Ia Supernovae Been Discovered? *The Astrophysical Journal*, 594(2):L93–L94, sep 2003. ISSN 0004-637X. doi: 10.1086/378765.

M. Lopez-Corredoira, F. Melia, E. Lusso, and G. Risaliti. Cosmological test with the QSO Hubble diagram. *International Journal of Modern Physics D*, 25(05):1650060, apr 2016. ISSN 02182718. doi: 10.1142/S0218271816500607.

Jing-Zhe Ma and Xin Zhang. Probing the dynamics of dark energy with novel parametrizations. *Physics Letters B*, 699(4):233–238, may 2011. ISSN 03702693. doi: 10.1016/j.physletb.2011.04.013.

Yin-Zhe Ma and Jun Pan. An estimation of local bulk flow with the maximum-likelihood method. *Monthly Notices of the Royal Astronomical Society*, 437(2):1996–2004, jan 2014. ISSN 1365-2966. doi: 10.1093/mnras/stt2038.

Yin-Zhe Ma and Douglas Scott. Cosmic bulk flows on 50 Mpc scales: a Bayesian hyper-parameter method and multishell likelihood analysis. *Monthly Notices of the Royal Astronomical Society*, 428(3):2017–2028, jan 2013. ISSN 1365-2966. doi: 10.1093/mnras/sts178.

B. F. Madore. The period-luminosity relation. IV - Intrinsic relations and reddenings for the Large Magellanic Cloud Cepheids. *The Astrophysical Journal*, 253(2):575, feb 1982. ISSN 0004-637X. doi: 10.1086/159659.

F. Mannucci, M. Della Valle, N. Panagia, et al. The supernova rate per unit mass. *Astronomy and Astrophysics*, 433(3):807–814, apr 2005. ISSN 0004-6361. doi: 10.1051/0004-6361:20041411.

F. Mannucci, M. Della Valle, and N. Panagia. Two populations of progenitors for Type la supernovae? *Monthly Notices of the Royal Astronomical Society*, 370(2):773–783, oct 2006. ISSN 00358711. doi: 10.1111/j.1365-2966.2006.10501.x.

Dan Maoz and Or Graur. Star Formation, Supernovae, Iron, and α : Consistent Cosmic and Galactic Histories. *The Astrophysical Journal*, 848(1):25, oct 2017. ISSN 1538-4357. doi: 10.3847/1538-4357/aa8b6e.

Dan Maoz and Filippo Mannucci. Type-Ia Supernova Rates and the Progenitor Problem: A Review. *Publications of the Astronomical Society of Australia*, 29(04):447–465, jan 2012. ISSN 1323-3580. doi: 10.1071/AS11052.

Dan Maoz, Filippo Mannucci, and Gijs Nelemans. Observational Clues to the Progenitors of Type Ia Supernovae. *Annual Review of Astronomy and Astrophysics*, 52(1):107–170, dec 2014. ISSN 0066-4146. doi: 10.1146/annurev-astro-082812-141031.

R. Minkowski. The Spectra of the Supernovae in IC 4182 and in NGC 1003. *The Astrophysical Journal*, 89:156, mar 1939. ISSN 0004-637X. doi: 10.1086/144037.

S. Miyaji, K. Nomoto, K. Yokoi, and D. Sugimoto. Supernova Triggered by Electron Captures. *Publications of the Astronomical Society of Japan*, 32:303, 1980.

James D. Neill, Michael J. Hudson, and Alex Conley. The Peculiar Velocities of Local Type Ia Supernovae and Their Impact on Cosmology. *The Astrophysical Journal*, 661(2):L123–L126, jun 2007. ISSN 0004-637X. doi: 10.1086/518808.

K. Nomoto, F.-K. Thielemann, and K. Yokoi. Accreting white dwarf models of Type I supernovae. III - Carbon deflagration supernovae. *The Astrophysical Journal*, 286:644, nov 1984. ISSN 0004-637X. doi: 10.1086/162639.

Ken'ichi Nomoto, Hideyuki Saio, Mariko Kato, and Izumi Hachisu. Thermal Stability of White Dwarfs Accreting Hydrogen-rich Matter and Progenitors of Type Ia Supernovae. *The Astrophysical Journal*, 663(2):1269–1276, jul 2007. ISSN 0004-637X. doi: 10.1086/518465.

Adi Nusser and Marc Davis. THE COSMOLOGICAL BULK FLOW: CONSISTENCY WITH ΛCDM AND z 0 CONSTRAINTS ON σ 8 AND γ. *The Astrophysical Journal*, 736(2):93, aug 2011. ISSN 0004-637X. doi: 10.1088/0004-637X/736/2/93.

S. J. Osborne, D. S. Y. Mak, S. E. Church, and E. Pierpaoli. MEASURING THE GALAXY CLUSTER BULK FLOW FROM WMAP DATA. *The Astrophysical Journal*, 737(2):98, aug 2011. ISSN 0004-637X. doi: 10.1088/0004-637X/737/2/98.

Nikhil Padmanabhan, Xiaoying Xu, Daniel J. Eisenstein, et al. Methods and application to the Sloan Digital Sky Survey. *Mon. Not. R. Astron. Soc*, 427:2132–2145, jan 2012. ISSN 0035-8711. doi: 10.1111/j.1365-2966.2012.21888.x.

G. Pantazis, S. Nesseris, and L. Perivolaropoulos. Comparison of thawing and freezing dark energy parametrizations. *Physical Review D - Particles, Fields, Gravitation and Cosmology*, 93 (10), mar 2016. ISSN 15502368. doi: 10.1103/PhysRevD.93.103503.

Changbom Park, Yun-Young Choi, Juhan Kim, et al. THE CHALLENGE OF THE LARGEST STRUCTURES IN THE UNIVERSE TO COSMOLOGY. *The Astrophysical Journal*, 759(1): L7, nov 2012. ISSN 2041-8205. doi: 10.1088/2041-8205/759/1/L7.

P. J. E. Peebles. Principles of Physical Cosmology, 1994. ISSN 00029505.

S. Perlmutter, S. Gabi, G. Goldhaber, et al. Measurements of the Cosmological Parameters Ω and Λ from the First Seven Supernovae at z $>$ 0.35. *The Astrophysical Journal*, 483(2):565–581, jul 1997. ISSN 0004-637X. doi: 10.1086/304265.

S. Perlmutter, G. Aldering, G. Goldhaber, et al. Measurements of Ω and Λ from 42 High-Redshift Supernovae. *The Astrophysical Journal*, 517(2):565–586, jun 1999. ISSN 0004-637X. doi: 10.1086/307221.

Saul Perlmutter and Brian P. Schmidt. Measuring Cosmology with Supernovae. *Lect.Notes Phys.*, 598:195–217, mar 2003. ISSN 0004-640X. doi: 10.1007/3-540-45863-8_11.

M. M. Phillips. The absolute magnitudes of Type IA supernovae. *The Astrophysical Journal*, 413: L105, aug 1993. ISSN 0004-637X. doi: 10.1086/186970.

M. M. Phillips, Paulina Lira, Nicholas B. Suntzeff, et al. The Reddening-Free Decline Rate Versus Luminosity Relationship for Type [CLC]Ia[/CLC] Supernovae. *The Astronomical Journal*, 118 (4):1766–1776, oct 1999. ISSN 00046256. doi: 10.1086/301032.

Planck Collaboration. Planck intermediate results. *Astronomy & Astrophysics*, 561:A97, jan 2014. ISSN 0004-6361. doi: 10.1051/0004-6361/201321299.

Planck Collaboration. Planck 2015 results. XV. Gravitational lensing. *Astronomy and Astrophysics*, 594:10, feb 2015. ISSN 0004-6361. doi: 10.1051/0004-6361/201525941.

Planck Collaboration. Planck 2015 results. *Astronomy & Astrophysics*, 594:A13, oct 2016. ISSN 0004-6361. doi: 10.1051/0004-6361/201525830.

Christopher J. Pritchet, D. Andrew Howell, and Mark Sullivan. The Progenitors of Type Ia Supernovae. *The Astrophysical Journal*, 683(1):L25–L28, aug 2008. ISSN 0004-637X. doi: 10.1086/591314.

Roland De Putter and Eric V. Linder. Calibrating Dark Energy. *Journal of Cosmology and Astroparticle Physics*, 2008(10):042, aug 2008. ISSN 1475-7516. doi: 10.1088/1475-7516/2008/10/042.

Bharat Ratra and P. J. E. Peebles. Cosmological consequences of a rolling homogeneous scalar field. *Physical Review D*, 37(12):3406–3427, jun 1988. ISSN 05562821. doi: 10.1103/PhysRevD.37.3406.

Adam G. Riess, William H. Press, and Robert P. Kirshner. Using Type IA supernova light curve shapes to measure the Hubble constant. *The Astrophysical Journal*, 438:L17, jan 1995. ISSN 0004-637X. doi: 10.1086/187704.

Adam G. Riess, William H. Press, and Robert P. Kirshner. Is the Dust Obscuring Supernovae in Distant Galaxies the Same as Dust in the Milky Way? *The Astrophysical Journal*, 473(2): 588–594, dec 1996. ISSN 0004-637X. doi: 10.1086/178174.

Adam G. Riess, Alexei V. Filippenko, Peter Challis, et al. Observational Evidence from Supernovae for an Accelerating Universe and a Cosmological Constant. *The Astronomical Journal*, 116(3):1009–1038, sep 1998. ISSN 00046256. doi: 10.1086/300499.

Adam G. Riess, Lucas M. Macri, Samantha L. Hoffmann, et al. A 2.4% DETERMINATION OF THE LOCAL VALUE OF THE HUBBLE CONSTANT. *The Astrophysical Journal*, 826(1): 56, jul 2016a. ISSN 1538-4357. doi: 10.3847/0004-637X/826/1/56.

Adam G. Riess, Lucas M. Macri, Samantha L. Hoffmann, et al. A 2.4% DETERMINATION OF THE LOCAL VALUE OF THE HUBBLE CONSTANT. *The Astrophysical Journal*, 826(1): 56, jul 2016b. ISSN 1538-4357. doi: 10.3847/0004-637X/826/1/56.

G. Risaliti and E. Lusso. a Hubble Diagram for Quasars. *The Astrophysical Journal*, 815(1):33, dec 2015. ISSN 1538-4357. doi: 10.1088/0004-637X/815/1/33.

Steven A. Rodney, Adam G. Riess, Louis-Gregory Strolger, et al. Type Ia Supernova Rate Measurements to Redshift 2.5 from CANDELS : Searching for Prompt Explosions in the Early Universe. *The Astronomical Journal*, 148(1):13, jun 2014. ISSN 0004-6256. doi: 10.1088/0004-6256/148/1/13.

Vicente Rodriguez-Gomez, Annalisa Pillepich, Laura V. Sales, et al. The stellar mass assembly of galaxies in the Illustris simulation: growth by mergers and the spatial distribution of accreted stars. *Monthly Notices of the Royal Astronomical Society*, 458(3):2371–2390, may 2016. ISSN 0035-8711. doi: 10.1093/mnras/stw456.

F. K. Röpke, M. Kromer, I. R. Seitenzahl, et al. CONSTRAINING TYPE Ia SUPERNOVA MODELS: SN 2011fe AS A TEST CASE. *The Astrophysical Journal*, 750(1):L19, may 2012. ISSN 2041-8205. doi: 10.1088/2041-8205/750/1/L19.

Ashley J. Ross, Lado Samushia, Cullan Howlett, et al. The clustering of the SDSS DR7 main Galaxy sample - I: A 4 per cent distance measure at z = 0.15. *Monthly Notices of the Royal Astronomical Society*, 449(1):835–847, sep 2015. ISSN 13652966. doi: 10.1093/mnras/stv154.

A. J. Ruiter, K. Belczynski, S. A. Sim, et al. Delay times and rates for Type Ia supernovae and thermonuclear explosions from double-detonation sub-Chandrasekhar mass models. *Monthly Notices of the Royal Astronomical Society*, 417(1):408–419, oct 2011. ISSN 00358711. doi: 10.1111/j.1365-2966.2011.19276.x.

Martin Sahlén, Andrew R. Liddle, and David Parkinson. Quintessence reconstructed: New constraints and tracker viability. *Physical Review D - Particles, Fields, Gravitation and Cosmology*, 75(2):023502, jan 2007. ISSN 15507998. doi: 10.1103/PhysRevD.75.023502.

H. Saio and K. Nomoto. Evolution of a merging pair of C + O white dwarfs to form a single neutron star. *Astronomy and Astrophysics*, 150(1):L21–L23, 1985.

Evan Scannapieco and Lars Bildsten. The Type Ia Supernova Rate. *The Astrophysical Journal*, 629(2):L85–L88, aug 2005. ISSN 0004-637X. doi: 10.1086/452632.

Robert J. Scherrer. Dark energy models in the w - w' plane. *Phys. Rev.*, D73(3):43502, feb 2006. ISSN 1550-7998. doi: 10.1103/PhysRevD.73.043502.

Robert J. Scherrer and A. A. Sen. Thawing quintessence with a nearly flat potential. *Physical Review D - Particles, Fields, Gravitation and Cosmology*, 77(8):083515, apr 2008. ISSN 15507998. doi: 10.1103/PhysRevD.77.083515.

C. Schimd, I. Tereno, J. P. Uzan, et al. Tracking quintessence by cosmic shear. Constraints from VIRMOS-Descart and CFHTLS and future prospects. *Astronomy and Astrophysics*, 463(2): 405, feb 2007. ISSN 00046361. doi: 10.1051/0004-6361:20065154.

D. Scolnic, A. Rest, A. Riess, et al. SYSTEMATIC UNCERTAINTIES ASSOCIATED WITH THE COSMOLOGICAL ANALYSIS OF THE FIRST PAN-STARRS1 TYPE Ia SUPERNOVA SAMPLE. *The Astrophysical Journal*, 795(1):45, oct 2014. ISSN 1538-4357. doi: 10.1088/0004-637X/795/1/45.

D. Scolnic, S. Casertano, A. Riess, et al. SUPERCAL: CROSS-CALIBRATION OF MULTIPLE PHOTOMETRIC SYSTEMS TO IMPROVE COSMOLOGICAL MEASUREMENTS WITH TYPE Ia SUPERNOVAE. *The Astrophysical Journal*, 815(2):117, dec 2015. ISSN 1538-4357. doi: 10.1088/0004-637X/815/2/117.

Dario Scovacricchi, Robert C. Nichol, David Bacon, Mark Sullivan, and Szymon Prajs. Cosmology with superluminous supernovae. *Monthly Notices of the Royal Astronomical Society*, 456 (2):1700–1707, feb 2016. ISSN 0035-8711. doi: 10.1093/mnras/stv2752.

Morag I. Scrimgeour, Tamara M. Davis, Chris Blake, et al. The 6dF Galaxy Survey: bulk flows on 50-70 h -1 Mpc scales. *Monthly Notices of the Royal Astronomical Society*, 455(1):386–401, jan 2016. ISSN 0035-8711. doi: 10.1093/mnras/stv2146.

Ivo R. Seitenzahl, Franco Ciaraldi-Schoolmann, Friedrich K. Röpke, et al. Three-dimensional delayed-detonation models with nucleosynthesis for Type Ia supernovae. *Monthly Notices of the Royal Astronomical Society*, 429(2):1156–1172, feb 2013. ISSN 0035-8711. doi: 10.1093/mnras/sts402.

Uros Seljak and Matias Zaldarriaga. A Line-of-Sight Integration Approach to Cosmic Microwave Background Anisotropies. *The Astrophysical Journal*, 469:437, mar 1996. ISSN 0004-637X. doi: 10.1086/177793.

Ken J. Shen and Lars Bildsten. Thermally Stable Nuclear Burning on Accreting White Dwarfs. *The Astrophysical Journal*, 660(2):1444–1450, may 2007. ISSN 0004-637X. doi: 10.1086/513457.

Ken J. Shen, Daniel Kasen, Nevin N. Weinberg, Lars Bildsten, and Evan Scannapieco. THERMONUCLEAR .Ia SUPERNOVAE FROM HELIUM SHELL DETONATIONS: EXPLOSION MODELS AND OBSERVABLES. *The Astrophysical Journal*, 715(2):767–774, jun 2010. ISSN 0004-637X. doi: 10.1088/0004-637X/715/2/767.

S. A. Sim, F. K. Röpke, W. Hillebrandt, et al. DETONATIONS IN SUB-CHANDRASEKHAR-MASS C+O WHITE DWARFS. *The Astrophysical Journal*, 714(1):L52–L57, may 2010. ISSN 2041-8205. doi: 10.1088/2041-8205/714/1/L52.

Mathew Smith, Robert C Nichol, Benjamin Dilday, et al. THE SDSS-II SUPERNOVA SURVEY: PARAMETERIZING THE TYPE Ia SUPERNOVA RATE AS A FUNCTION OF HOST GALAXY PROPERTIES. *The Astrophysical Journal*, 755(1):61, aug 2012. ISSN 0004-637X. doi: 10.1088/0004-637X/755/1/61.

J.-E. Solheim. AM CVn Stars: Status and Challenges. *Publications of the Astronomical Society of the Pacific*, 122(896):1133–1163, oct 2010. ISSN 0004-6280. doi: 10.1086/656680.

Jan-Erik Solheim and Lev R. Yungelson. The White Dwarfs in AM CVn systems - candidates for SN Ia? *Astronomical Society of the Pacific Conference Series*, 334:357, nov 2004. ISSN 1050-3390.

Thomas P. Sotiriou and Valerio Faraoni. F (R) theories of gravity. *Reviews of Modern Physics*, 82 (1):451–497, may 2010. ISSN 00346861. doi: 10.1103/RevModPhys.82.451.

Martin Sparre, Christopher C. Hayward, Volker Springel, et al. The star formation main sequence and stellar mass assembly of galaxies in the Illustris simulation. *Monthly Notices of the Royal Astronomical Society*, 447(4):3548–3563, jan 2015. ISSN 0035-8711. doi: 10.1093/mnras/stu2713.

Sumner Starrfield. The accretion of solar material onto white dwarfs: No mixing with core material implies that the mass of the white dwarf is increasing. *AIP Advances*, 4(4):041007, apr 2014. ISSN 2158-3226. doi: 10.1063/1.4866984.

M. Sullivan, D. Le Borgne, C. J. Pritchet, et al. Rates and Properties of Type Ia Supernovae as a Function of Mass and Star Formation in Their Host Galaxies. *The Astrophysical Journal*, 648 (2):868–883, may 2006. ISSN 0004-637X. doi: 10.1086/506137.

M. Sullivan, R. S. Ellis, D. A. Howell, et al. THE MEAN TYPE IA SUPERNOVA SPECTRUM OVER THE PAST NINE GIGAYEARS. *The Astrophysical Journal*, 693(2):L76–L80, mar 2009. ISSN 0004-637X. doi: 10.1088/0004-637X/693/2/L76.

M. Sullivan, A. Conley, D. A. Howell, et al. The dependence of Type Ia Supernovae luminosities on their host galaxies. *Monthly Notices of the Royal Astronomical Society*, 406(2):no–no, may 2010. ISSN 00358711. doi: 10.1111/j.1365-2966.2010.16731.x.

R. Terlevich, E. Terlevich, J. Melnick, et al. On the road to precision cosmology with high-redshift H II galaxies. *Monthly Notices of the Royal Astronomical Society*, 451(3):3001–3010, jun 2015. ISSN 0035-8711. doi: 10.1093/mnras/stv1128.

Tomonori Totani, Tomoki Morokuma, Takeshi Oda, Mamoru Doi, and Naoki Yasuda. Delay Time Distribution Measurement of Type Ia Supernovae by the Subaru/XMM-Newton Deep Survey and Implications for the Progenitor. *Publications of the Astronomical Society of Japan*, 60(6): 1327–1346, dec 2008. ISSN 0004-6264. doi: 10.1093/pasj/60.6.1327.

Shinji Tsujikawa. Quintessence: a review. *Classical and Quantum Gravity*, 30(21):214003, nov 2013. ISSN 0264-9381. doi: 10.1088/0264-9381/30/21/214003.

T. Tsujimoto, K. Nomoto, Y. Yoshii, et al. Relative frequencies of Type Ia and Type II supernovae in the chemical evolution of the Galaxy, LMC and SMC. *Monthly Notices of the Royal Astronomical Society*, 277(3):945–958, dec 1995. ISSN 0035-8711. doi: 10.1093/mnras/277.3.945.

Stephen J. Turnbull, Michael J. Hudson, Hume A. Feldman, et al. Cosmic flows in the nearby universe from Type Ia supernovae. *Monthly Notices of the Royal Astronomical Society*, 420(1): 447–454, feb 2012. ISSN 00358711. doi: 10.1111/j.1365-2966.2011.20050.x.

A. Tutukov and L. Yungelson. Double-degenerate semidetached binaries with helium secondaries: cataclysmic variables, supersoft X-ray sources, supernovae and accretion-induced collapses. *Monthly Notices of the Royal Astronomical Society*, 280(4):1035–1045, jun 1996. ISSN 0035-8711. doi: 10.1093/mnras/280.4.1035.

Mark Vogelsberger, Shy Genel, Volker Springel, et al. Properties of galaxies reproduced by a hydrodynamic simulation. *Nature*, 509(7499):177–182, may 2014a. ISSN 0028-0836. doi: 10.1038/nature13316.

Mark Vogelsberger, Shy Genel, Volker Springel, et al. Introducing the Illustris Project: simulating the coevolution of dark and visible matter in the Universe. *Monthly Notices of the Royal Astronomical Society*, 444(2):1518–1547, aug 2014b. ISSN 0035-8711. doi: 10.1093/mnras/stu1536.

Lifan Wang, Peter Höflich, and J. Craig Wheeler. Supernovae and Their Host Galaxies. *The Astrophysical Journal*, 483(1):L29–L32, jul 1997. ISSN 0004637X. doi: 10.1086/310737.

Lifan Wang, Gerson Goldhaber, Greg Aldering, and Saul Perlmutter. Multicolor Light Curves of Type Ia Supernovae on the Color-Magnitude Diagram: A Novel Step toward More Precise Distance and Extinction Estimates. *The Astrophysical Journal*, 590(2):944–970, jun 2003. ISSN 0004-637X. doi: 10.1086/375020.

Xiaofeng Wang, Lifan Wang, Xu Zhou, Yuqing Lou, and Zongwei Li. A Novel Color Parameter as a Luminosity Calibrator for Type Ia Supernovae. *The Astrophysical Journal*, 620(2):L87–L90, feb 2005. ISSN 0004-637X. doi: 10.1086/428774.

Richard Watkins and Hume A. Feldman. Large-scale bulk flows from the Cosmicflows-2 catalogue. *Monthly Notices of the Royal Astronomical Society*, 447(1):132–139, feb 2015. ISSN 1365-2966. doi: 10.1093/mnras/stu2414.

Richard Watkins, Hume A. Feldman, and Michael J. Hudson. Consistently large cosmic flows on scales of 100 Mpc : a challenge for the standard ΛCDM cosmology. *Monthly Notices of the Royal Astronomical Society*, 392(2):743–756, jan 2009. ISSN 00358711. doi: 10.1111/j.1365-2966.2008.14089.x.

Anja Weyant, Michael Wood-Vasey, Larry Wasserman, and Peter Freeman. AN UNBIASED METHOD OF MODELING THE LOCAL PECULIAR VELOCITY FIELD WITH TYPE Ia SUPERNOVAE. *The Astrophysical Journal*, 732(2):65, may 2011. ISSN 0004-637X. doi: 10.1088/0004-637X/732/2/65.

Radosław Wojtak and Francisco Prada. Redshift remapping and cosmic acceleration in dark-matter-dominated cosmological models. *Monthly Notices of the Royal Astronomical Society*, 470(4):4493–4511, oct 2017. ISSN 0035-8711. doi: 10.1093/mnras/stx1550.

Radosław Wojtak, Tamara M. Davis, and Jophiel Wiis. Local gravitational redshifts can bias cosmological measurements. *Journal of Cosmology and Astroparticle Physics*, 2015(07):025–025, jul 2015. ISSN 1475-7516. doi: 10.1088/1475-7516/2015/07/025.

William M. Wolf, Lars Bildsten, Jared Brooks, and Bill Paxton. HYDROGEN BURNING ON ACCRETING WHITE DWARFS: STABILITY, RECURRENT NOVAE, AND THE POST-NOVA SUPERSOFT PHASE. *The Astrophysical Journal*, 777(2):136, oct 2013. ISSN 0004-637X. doi: 10.1088/0004-637X/777/2/136.

Lev R. Yungelson and Mario Livio. Supernova Rates: A Cosmic History. *The Astrophysical Journal*, 528(1):108–117, jan 2000. ISSN 0004-637X. doi: 10.1086/308174.

Matias Zaldarriaga, Uros Seljak, and Edmund Bertschinger. Integral Solution for the Microwave Background Anisotropies in Nonflat Universes. *The Astrophysical Journal*, 494:491, apr 1998. ISSN 0004-637X. doi: 10.1086/305223.

Bonnie R. Zhang, Michael J. Childress, Tamara M. Davis, et al. A blinded determination of H0 from low-redshift Type Ia supernovae, calibrated by Cepheid variables. *Monthly Notices of the Royal Astronomical Society*, 471(2):2254–2285, oct 2017. ISSN 0035-8711. doi: 10.1093/mnras/stx1600.